Additive Manufacturing and Characterization of Micro-architected Lithium-ion Battery Electrodes

Thesis by

Yingjin Wang

In Partial Fulfillment of the Requirements for

the Degree of

Doctor of Philosophy

CALIFORNIA INSTITUTE OF TECHNOLOGY

Pasadena, California

2026

Defended April 21, 2026

Yingjin Wang
ORCID: 0009-0002-1239-3422

ACKNOWLEDGEMENTS

I would like to express my sincere gratitude to my advisor, Prof. Julia R. Greer, for her support, guidance, and patience throughout my PhD journey. Her constant encouragement has profoundly shaped not only this research work but also who I have become during these years. I am grateful for the trust and opportunities she has given me along the way. I am also sincerely thankful to Prof. Katherine T. Faber, Prof. Guruswami Ravichandran, and Prof. Kimberly A. See for their insightful advice as members of my thesis committee.

I would like to extend my appreciation to my mentor, Dr. Yuchun Sun, for her patient guidance at the beginning of my project and her continuous support throughout my research. I would also like to thank the other battery subgroup members, Dr. Max A. Saccone, Dr. Fernando J. Villafuerte, Dr. Wenyuan Chen, Ethan Klein, Cyrus Fiori, Joel Chacko, and Dawn Ford, for their helpful discussions and suggestions. I am equally grateful to our mechanics subgroup members, Dr. Seola Lee, Dr. Wenxin Zhang, Dr. Thomas T. Tran, and Dr. Kevin Nakahara, for their collaboration and willingness to help at every stage of my research. I would also like to thank my office mates, Dr. Weiting Deng, Kaiyu Zhao, and Anna Wu, for their companionship. Most importantly, I would like to thank all members of the Greer group for the many moments we shared during this trip.

I would like to express my sincere appreciation to my collaborators, Dr. Se H. Park and Dr. Sun G. Yoon, for their invaluable contributions and thoughtful guidance throughout the course of this research. I would like to thank Dr. Chi Ma for his assistance, as well as the Caltech GPS Analytical Facility.

Finally, I would like to express my deepest appreciation to my mother. She has supported me through every challenge, and I would not be here without her.

但愿桥都坚固，隧道都光明

ABSTRACT

Electrode structure is closely coupled with mechanical behavior, ion transport, and reaction uniformity during battery operation. In addition to conventional slurry-cast electrodes, emerging fabrication approaches provide new opportunities to study and design electrode architectures. This thesis investigates lithium-ion battery electrodes through two complementary perspectives related to the electrode structure: micro-scale mechanical characterization to elucidate degradation mechanisms and additive manufacturing of three-dimensional (3D) micro-architected electrodes to investigate structure-transport relationships.

In Chapters 2 and 3, the mechanical behavior of lithium-ion battery electrodes was investigated using nanoindentation and micro-pillar compression experiments. State-of-charge-dependent mechanical properties of electroplated $LiCoO_2$ (LCO) cathodes were quantified, revealing a decreasing tendency in elastic modulus and hardness during delithiation, which is attributed to the expansion of LCO layered structure. Fracture toughness distribution across the electrode thickness was analyzed to understand how structural heterogeneity contributes to the mechanical property landscape. In addition, we studied the deformation of lithium-based composite anodes, confirming that the Li/Na composite anode exhibits higher deformability at the electrode-electrolyte interface, which enhances interfacial contact.

The interconnected pore structure and large surface-to-volume ratio of 3D architected battery electrodes render them promising for enhancing electrochemical performance via more efficient ionic transport. In Chapters 4 and 5, we develop a hydrogel infusion additive manufacturing (HIAM)-based approach to fabricate micro-architected $LiFePO_4$ (LFP)/C composite electrodes with feature sizes down to 18 μm. The concomitant formation of carbon within the lattice enhances the mechanical strength, which preserves shape integrity of the 3D structure during cell assembly and function. We designed electrodes with different geometries, including tilted cubes, honeycombs, and triply periodic minimal surfaces (TPMS), to probe the influence of geometric factors on electrochemical performance under

various charge-discharge rates. We propose an experimentally informed electrochemical model that demonstrates the roles of Li^+ transport in the electrolyte and Li^+ diffusion in the electrode in determining the utilization of active materials. This work introduces a versatile manufacturing platform for printing 3D battery components and provides insights into structure optimization for high-performance rechargeable batteries.

PUBLISHED CONTENT AND CONTRIBUTIONS

Chapter 2 has partly been adapted from:

1. Park, S. H.; Juarez-Yescas, C.; Naik, K. G.; Wang, Y.; Luo, Y.; Puthusseri, D.; Kwon, P.; Vishnugopi, B. S.; Shyam, B.; Yang, H.; Cook, J.; Okasinski, J.; Chuang, A. C.; Xiao, X.; Greer, J. R.; Mukherjee, P. P.; Zahiri, B.; Braun, P. V.; Hatzell, K. B. Morphological Heterogeneity Impact of Film Solid-State Cathode on Utilization and Fracture Dynamics. *ACS Nano* **2025**, *19* (23), 21878–21890. https://doi.org/10.1021/acsnano.5c06799.

   Contributions: Y.W. performed mechanics investigations and participated in writing sections of the manuscript.

Chapter 3 has partly been adapted from:

2. Yoon, S. G.; Vishnugopi, B.; Nelson, D.; Xiao Bin Yong, A.; Wang, Y.; Sandoval, S.; Thomas, T.; Cavallaro, K.; Shevchenko, P.; Alsaç, E. P.; Wang, C.; Singla, A.; Greer, J.; Ertekin, E.; Mukherjee, P.; McDowell, M. Interface Morphogenesis with a Deformable Secondary Phase in Solid-State Lithium Batteries. *Science* **2025**, *388* (6751), 1062–1068. https://doi.org/10.1126/science.adt5229.

   Contributions: Y.W. performed mechanics investigations and participated in writing sections of the manuscript.

Chapter 4 and Chapter 5 have been adapted from:

3. Wang, Y.; Sun, Y.; Greer, J. R. Structure–Transport Relationships in Microarchitected LiFePO4–Carbon Li Ion Battery Electrodes. *ACS Energy Lett.* **2026**.

   https://doi.org/10.1021/acsenergylett.6c00372.

   Contributions: Y.W. conceived the study, developed the fabrication process, fabricated all samples, designed and performed the experiments, analyzed the data, and wrote the manuscript.

Not directly adapted in this thesis:

4. Koch, T.; Zhang, W.; Tran, T. T.; Wang, Y.; Mikitisin, A.; Puchhammer, J.; Greer, J. R.; Ovsianikov, A.; Chalupa‐Gantner, F.; Lunzer, M. Approaching Standardization: Mechanical Material Testing of Macroscopic Two‐Photon Polymerized Specimens. *Adv. Mater.* **2024**, 36 (34), 2308497.

   https://doi.org/10.1002/adma.202308497.

   Contributions: Y.W. conducted micro-tensile experiments.

TABLE OF CONTENTS

LIST OF ILLUSTRATIONS

LIST OF TABLES

Chapter 1

INTRODUCTION

1.1 Development of lithium-ion battery

Lithium-ion batteries are playing an increasingly important role in modern society and have changed people's daily lives, as these efficient, portable, and rechargeable energy storage devices are used in a wide range of applications. Over the past few decades, lithium-ion batteries with high energy density and long cycle life have been developed to support the widespread use of portable electronic devices, such as smartphones and laptops. Recently, with the rapid development of electric vehicles and their growing market demand, new lithium-ion battery systems are being studied to provide longer driving range, fast charging capability, and reliable operation. In addition, to achieve net-zero emissions by 2050, the use of renewable energy has been growing rapidly. As a result, energy storage systems are being further improved to meet the reliability requirements of the power grid with the intermittent electricity generation from renewable sources. Demand for lithium-ion batteries has grown from 19 GWh in 2010 to 285 GWh in 2019.[1] As electricity accounts for a larger share of the energy used, stored, and transmitted in modern society, the demand for lithium-ion batteries is expected to continue increasing and may experience exponential growth in the next few decades.[2]

The concept of Li-ion batteries was established in the 1970s. Lithium ions, with their low mass and small ionic size, were expected to maximize the energy-to-weight ratio and enhance current delivery capability.[3] The breakthrough happened in 1980, when Goodenough et al. discovered $LiCoO_2$ (LCO) as a layered oxide cathode that allows lithium ion intercalation/deintercalation at a high voltage of around 4V.[4] This discovery enabled the commercialization of lithium-ion batteries in 1991 by Sony[5], and since then, the development of lithium-ion battery materials has continued rapidly.

As one of the most expensive components, the cathode material largely determines the capacity and cost of lithium-ion batteries. Apart from LCO, other layered oxide materials, such as lithium nickel-manganese-cobalt oxide (NMC) and lithium nickel-cobalt-aluminum oxide (NCA), have been extensively studied and are widely used in consumer electronics. However, their dependence on cobalt, which is used to stabilize the material during cell cycling[6], raises concerns regarding high cost, limited resource availability, and ethical supply-chain issues. These challenges have motivated efforts to develop cobalt-free cathode materials for sustainable lithium-ion batteries. Beyond Co-containing layered oxide materials, phosphates of transition metals are considered among the most promising cathode materials for cathodes. Their strong P-O frameworks preserve a stable olivine structure during charge-discharge cycles, thereby ensuring excellent cycling stability and safety. Among these, $LiFePO_4$ (LFP) electrodes have been intensively explored due to their inherent high thermal and chemical stability, long cycle life, low cost, and non-toxicity.[7,8]

As for the anode side, graphite has been the dominant anode material since the 1990s. However, the theoretical capacity of 372 mAh/g limits its feasibility for high-energy applications[9], motivating the exploration of alternative high-capacity anode materials. Li metal has the highest theoretical capacity (3860 mAh/g), low density (0.5 g/cm^3), and the most negative electrochemical potential (-3.04 V vs. the standard hydrogen electrode) among lithium-ion battery anode materials.[10] Therefore, it is one of the most popular anode materials for next-generation lithium-ion batteries. In fact, Li metal was used as an anode in the early stages of lithium-ion battery research. However, safety concerns arise when lithium dendrites grow, penetrate the separator, and result in short circuits. To mitigate dendrite propagation and side reactions of Li metal, solid-state electrolytes, including inorganic ceramic electrolytes, polymer electrolytes, and their composites, have attracted increasing attention due to their potential for higher energy density and improved safety.[10]

1.2 Electro-chemo-mechanical challenges in lithium-ion batteries

Mechanical degradation of cathode active material is one of the main reasons for capacity fading and impedance growth in lithium-ion batteries over repeated charging and discharging. Cracks are observed at both grain boundaries and inside the grains of the cathode active material after cycling.[11,12] Cracks formed in the cathode particles can electrically isolate parts of the active material, thereby reducing the battery capacity. Meanwhile, the lithium-ion transport distance in the active material is increased, resulting in increased impedance.[13] As shown in Figure 1.1a, in 2020, Jiang et al. observed crack formation in LCO at twin boundaries and its propagation into the crystal along the (0003) planes using scanning transmission electron microscopy.[12] The mechanical degradation in the cathode is generally attributed to the repeated crystal lattice expansion and anisotropic volume change during lithiation and delithiation, which can result in stress accumulation inside cathode particles. Figure 1.1b shows the crystal lattice expansion along the c-axis and the increase of cell volume in LCO measured by in-situ X-ray diffraction as the material is charged and the Li concentration decreases.[14] Therefore, gaining insight into the mechanical properties of cathode active materials and how they evolve during battery cycling may contribute to improve battery durability and the development of predictive electro-chemo-mechanical models.

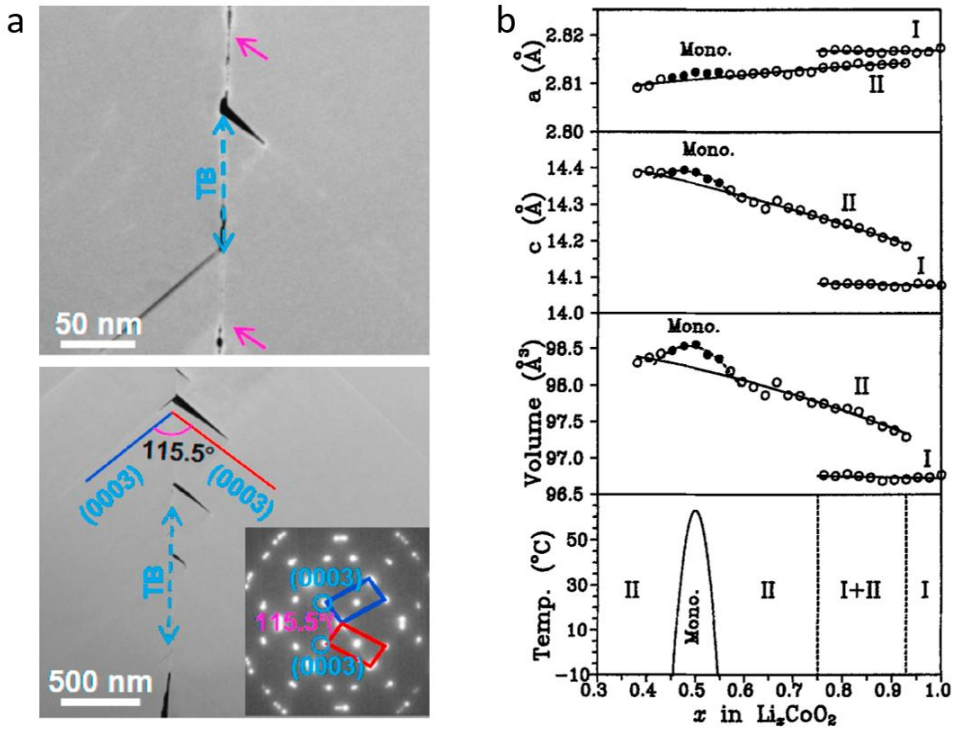

Figure 1.1 Cracks formation in LCO crystal. a) STEM-HAADF images of LCO particles with electrochemical cycling induced twin boundary deformation and cracking. Adapted with permission from reference [12]. Copyright 2020 Elsevier Ltd. b) Unit cell constants a, c, and cell volume as a function of lithium concentration x in Li_xCoO_2. Adapted with permission from reference [14]. Copyright The Electrochemical Society, Inc.

As discussed in the previous section, solid electrolytes are expected to mechanically suppress Li dendrite growth. In 2005, Monroe et al. suggested that a solid polymer electrolyte with a shear modulus roughly twice that of Li metal could suppress dendrite growth, based on linear stability analysis.[15] However, Li dendrites are still found to penetrate solid electrolytes and cause short circuits, even though the shear modulus of the solid electrolytes should be sufficiently high to suppress their growth. In Figure 1.2a, the Li dendrites are initiated at the solid electrolyte-Li metal interface and propagate into the $Li_{6.28}La_3Al_{0.3}Zr_2O_{12}$ (LLZO) electrolyte[16], whose shear modulus is measured to be 61 GPa[17], over ten times higher than

Li metal. This phenomenon can be explained by propagation of pre-existing interfacial defects. When Li metal fills in the interfacial flaws, the high current at the flaw tip and the accompanying volume increase generate stress that can open the crack.[18] In addition, size effect is also observed in lithium metal, indicating a much higher strength of lithium dendrites at the nano- or microscale.[19] On the other hand, during Li stripping, voids are generated when the current removes metal from the interface faster than it can be replenished by metal diffusion (Figure 1.2b).[20] The accumulation of voids at the interface can cause loss of contact area and higher local current density, which eventually leads to cell failure. As shown in Figure 1.2c, a widely adopted strategy is to apply external pressure perpendicular to the cell stack and maintain interfacial contact via stress-driven plastic deformation of the anode metal. Under the stack pressure, the mechanics and deformation of the anode metal play an important role in governing the nucleation and propagation of metal filaments during plating[21], as well as in maintaining low interfacial resistance at the metal/electrolyte interface during stripping[20].

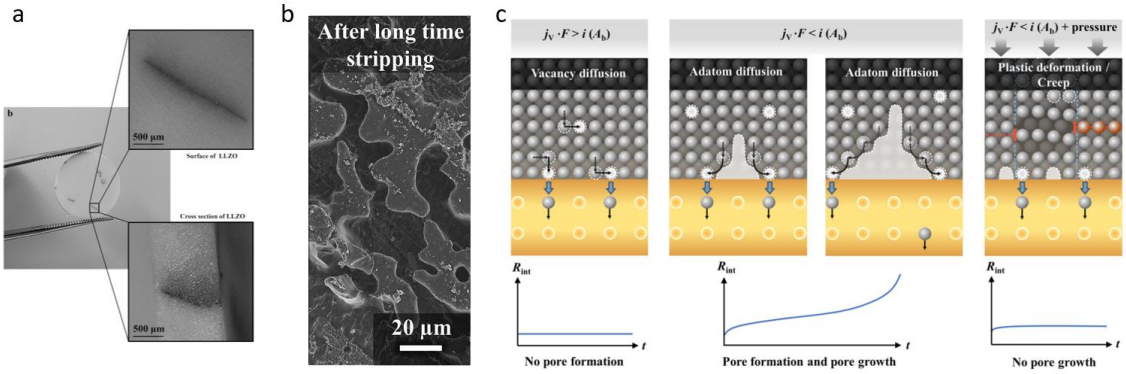

Figure 1.2 Degradation of interface between lithium metal anode and solid-state electrolyte. a) Lithium dendrites grow into LLZO pellet. Adapted with permission from reference [16]. Copyright 2015 Elsevier B.V. b) Morphology of the lithium metal anode facing solid electrolyte after long-time stripping without pressure applied. c) Strategy to maintain interfacial contact via stress-driven plastic deformation of the anode metal. Adapted with permission from reference [21]. Copyright 2019 American Chemical Society.

1.3 Electrodes with designed 3D structures

In commercial lithium-ion batteries, the electrode active materials are coated onto the current collectors in a slurry with conductive additives and binders. A 2D planar structure is used, where the anode, separator, and cathode are stacked layer by layer. When the battery is working, charge carriers must be transported through the separator and both electrodes. The rate performance is limited by several processes, as illustrated in Figure 1.3, including ion transport in both bulk electrolyte and electrolyte-filled pores, electrochemical reactions at the electrode/electrolyte interface, solid-state diffusion of ions in the active materials, and electronic transport within the electrodes.[22]

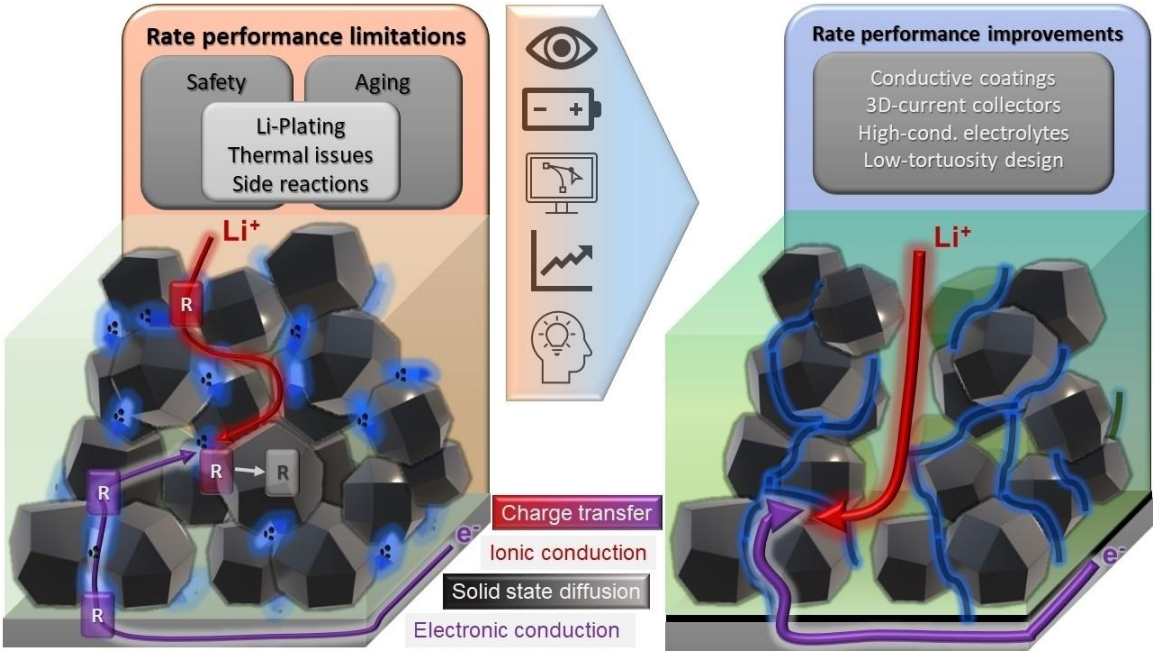

Figure 1.3 Rate performance limitations of Lithium-ion batteries and possible improvements. Adapted from reference [22]. Licensed under CC BY 4.0

These limitations become increasingly pronounced when efforts are made to improve battery capacity by increasing active material loading and using thick electrodes. The speed and efficiency of battery charging and discharging can be largely influenced by Li^+ transport in

the thick electrodes, which represents a key rate-limiting step in battery efficiency due to the material-dependent Li^+ diffusion kinetics, thereby limiting electrode thickness and active material loading[23,24]. As shown in Figure 1.4, to address this problem and to facilitate faster Li^+ transport, efforts have been made to incorporate anisotropic pores into thick electrodes[25–27], as well as to produce electrodes with desired 3D architectures.

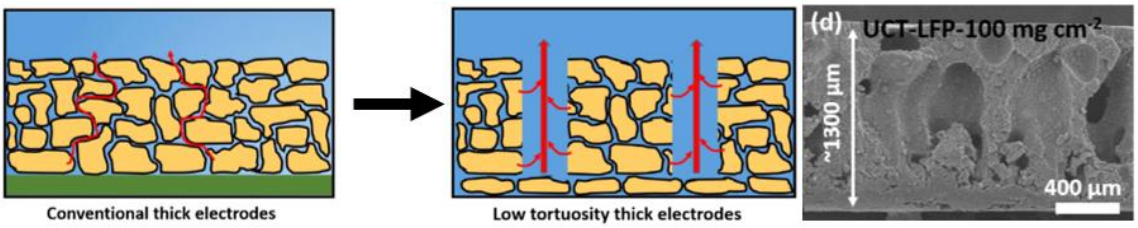

Figure 1.4 Low tortuosity thick electrodes. In order to provide the ion transfer pathways, vertically aligned pores are incorporated into thick electrodes. Adapted with permission from reference [25]. Copyright 2019 American Chemical Society.

Methods such as self-assembly[28–30], electrospinning[31,32], electrodeposition[33], and sacrificial templating[34,35] have been reported to produce 3D architected electrodes, with key findings highlighting the critical roles of pore morphology and architectural design in improving ion transport kinetics and electrochemical performance. The inherently high surface-to-volume ratio of most 3D-architected electrodes also enables higher active material mass loading while preserving short solid-state ion diffusion distances, thereby offering the potential to break the trade-off between energy density and power density of batteries[36].

1.4 Additive manufacturing techniques for battery electrodes

The development of advanced additive manufacturing techniques enables precise control over electrode dimensionality, shape, and pore structure.[37,38] The traditional extrusion-based 3D printing techniques, such as direct ink writing[39–41] and fused deposition modeling[42–44], have been used to prepare cathodes with designed 3D architectures since 2013 (Figure 1.5).

These traditional 3D printing techniques usually require introducing active material particles into the printing ink, especially for the cathode side, which may largely influence the printing resolution. The feature sizes of extrusion-based 3D printed cathodes are generally above 100 μm[41,43–45], higher than the Li^+ diffusion distance in a reasonable charge-discharge time on the order of tens of microns[24]. The associated layer-by-layer stacking strategy inherent to extrusion-based printing also severely limits electrode thickness and geometric complexity.

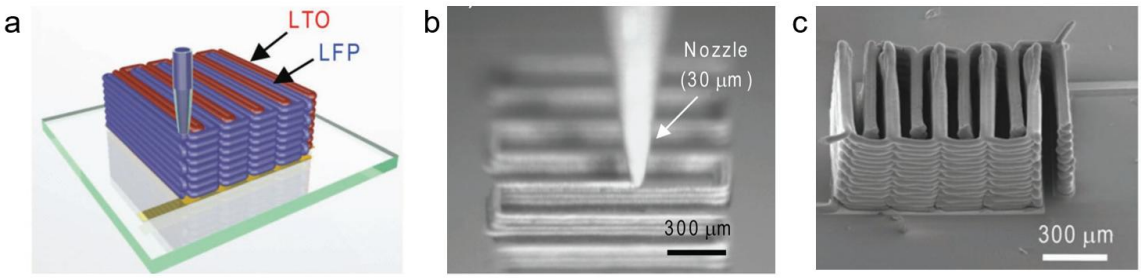

Figure 1.5 Extrusion-based 3D printing for lithium-ion batteries. a) Schematic illustration. b) LFP ink deposition through a nozzle. c) Printed and annealed 16-layer LTO-LFP electrode architecture. Adapted with permission from reference [39]. Copyright 2013 WILEY-VCH Verlag GmbH & Co. KGaA, Weinheim

A relatively new 3D printing technique based on vat photopolymerization has been adapted to prepare 3D architected electrodes with complex shapes, which does not require pre-mixing active material particles into the resin. As shown in Figure 1.6a, within a digital light processing (DLP) 3D printer, the ultraviolet (UV) light is projected through a digital micromirror array and guided through a transparent window at the bottom of the photoresin tank. A layer of photoresin is polymerized by the UV light into a designed 2D pattern. As the build head moves upward, the 3D structure is cured layer by layer and attached to the previously printed body. This 3D printing technique offers a resolution finer than 10 μm and is capable of printing complex 3D structures, such as overhanging features.

In 2021, Saccone et al.[46] dispersed aqueous solution of lithium sulfate hydrate in a UV-curable photopolymer resin to form an emulsion resin and fabricated architected lithium sulfide/carbon (Li_2S–C) cathodes with a 50 μm feature size and an octet-truss architecture. Yee, et al.[47] synthesized an aqueous photoresin using lithium nitrate and cobalt nitrate solutions to print cubic lattice LCO cathodes with a feature size of ~100 μm (Figure 1.6a). Improving on this process, hydrogel infusion additive manufacturing (HIAM), illustrated in Figure 1.6b, was developed by infusing precursor ions into a pre-printed gel scaffold.[48] The resolution is further improved due to the absence of scattering and absorbing light by emulsion or precursor ions. Sun, et al.[49] reduced the beam diameter in LCO cathodes to 45 μm (Figure 1.6c) and achieved a significantly improved capacity of 127 mAh/g at C/5, compared with 94 mAh/g in the similarly produced LCO lattices with a 100 μm beam diameter. Despite these advantages, when vat photopolymerization is used to produce thick electrodes, the resulting structures often lack conductive additives, and beam cracking can electrically isolate active material. These effects hinder further reduction in feature size and limit high-rate capacity. In addition, to gain fundamental insights into the performance of 3D-architected electrodes, it is important to uncover the mechanisms by which the 3D architecture influences the electrochemical performance of the produced electrodes and to quantify the dominant geometric factors that contribute to it.

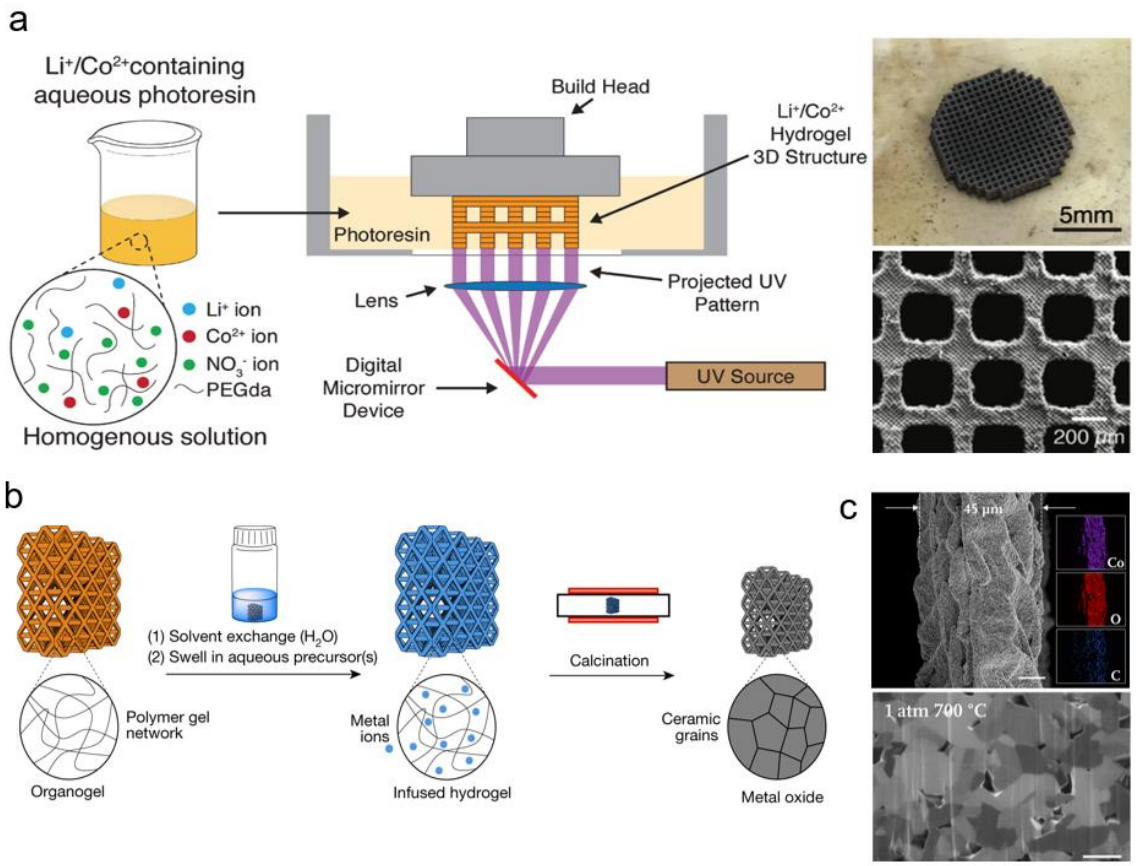

Figure 1.6 3D printing techniques based on vat photopolymerization for architected electrodes. a) LCO lattice with ~100 μm beam diameter printed by DLP 3D printing with Li+/Co2+ containing photoresin. Adapted with permission from reference [47]. Copyright 2020 Wiley-VCH GmbH. b) Schematic illustration for HIAM process. Adapted with permission from reference [48]. Copyright 2026 Springer Nature Limited. c) LCO lattice fabricated via HIAM with beam diameter of 45 μm. Adapted from reference [49]. Licensed under CC BY 4.0

1.5 Summary: Challenges faced by lithium-ion batteries

Lithium-ion batteries have become an integral part of people's daily lives, powering applications from portable electronics to electric vehicles. Their continued improvement is

closely related to the development of electrode materials. While commonly used cathode materials such as layered oxides offer high energy density, ongoing efforts aim to reduce dependence on costly elements such as cobalt and enhance sustainability. Transition meta phosphates, such as LFP, provide a more stable alternative. However, they are also facing challenges, including relatively low electronic conductivity and limited Li^+ diffusion kinetics. On the anode side, graphite remains reliable and commercially dominant, while emerging lithium metal anodes present opportunities for significantly higher energy density, accompanied by the need for solid-state electrolyte and improved control of interfacial stability to ensure safe operation.

In addition to materials innovation, battery performance is also influenced by coupled electrochemical, mechanical, and transport processes. Structure degradation during cycling of solid-state batteries under stack pressure can lead to capacity fading, motivating research to understand the mechanical behavior of electrode materials and stabilize the interface between electrode and electrolyte. Meanwhile, in thick electrodes designed for higher energy density, conventional electrode architectures face limitations in ionic transport and rate performance. To address this, advanced concepts such as 3D architected electrodes are being actively explored, offering new pathways to improve battery performance. Continued progress in materials design, interface engineering, and manufacturing techniques is supporting the development of next-generation lithium-ion batteries with improved energy density, rate capability, and safety.

Chapter 2

MECHANICAL CHARACTERIZATION OF ELECTRODEPOSITED LCO ELECTRODES

2.1 Overview

LCO is one of the most widely used cathode materials in commercial lithium-ion batteries and has been extensively applied in portable electronic devices. However, its mechanical degradation during electrochemical cycling can lead to electrode structure damage and is considered as one of the major factors responsible for capacity fading. Understanding the mechanical properties of LCO and their evolution during electrochemical cycling is therefore critical for improving battery durability and developing predictive electro-chemo-mechanical models.

Several modeling studies have indicated that the mechanical properties of LCO are strongly coupled with lithium concentration and thus dependent on its state of charge (SOC).[50,51] However, quantitative experimental measurements of how intrinsic mechanical properties evolve with SOC remain limited, particularly at the single-crystal or grain scale.[52,53]

This chapter investigates the mechanical properties of electrodeposited LCO cathodes using in-situ nanoindentation combined with microstructure characterization. The elastic modulus and hardness of LCO are measured at different SOC to reveal the dependence of mechanical properties on lithium concentration during lithiation and delithiation. In addition, nanoindentation on focused ion beam (FIB)-milled cross section is used to evaluate the distribution of fracture toughness across the electrode thickness. Electron backscatter diffraction (EBSD) analysis is performed to identify the crystallographic orientation of the electrodeposited LCO grains. Such information is essential for understanding stress

generation during battery operation and for improving electro-chemo-mechanical models that describe degradation in lithium-ion battery electrodes.

2.2 Nanoindentation on charged LCO cathode

The electroplated faceted LCO electrodes at different SOC were supplied by Xerion Advanced Battery Corp. (Kettering, Ohio) and Braun research group at the University of Illinois Urbana-Champaign. The electrodes were fabricated according to the process detailed in a previous study.[54] In this work, 100% charged LCO represents that 50% of the lithium is removed from the LCO crystal. The surface and cross-section SEM images of the pristine LCO samples electrodeposited on a metal foil are shown in Figure 2.1. The electrode thickness is around 19 μm.

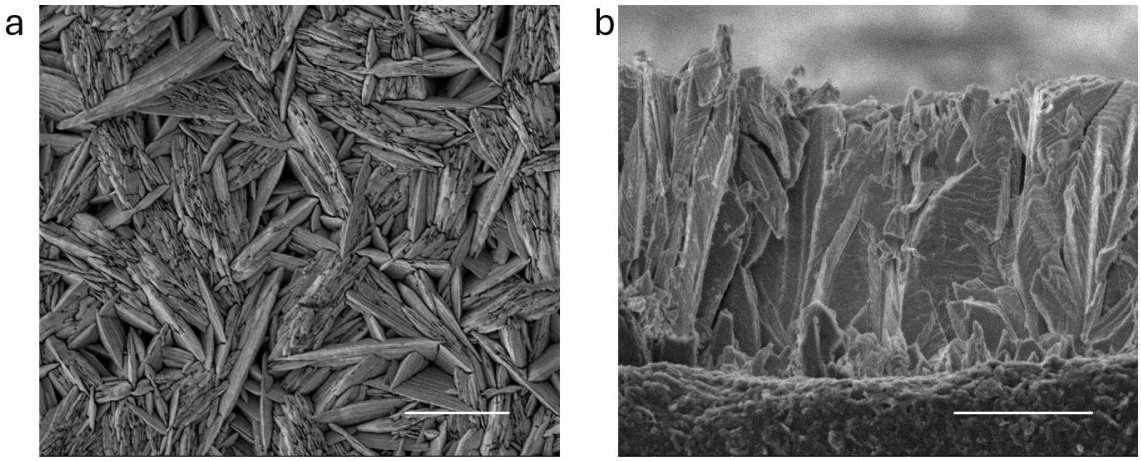

Figure 2.1 SEM images of electrodeposited LCO electrode a) surface and b) cross section. Scale bar = 10 μm.

To prepare a smooth surface for nanoindentation experiments, the LCO cathode was mounted onto a SEM stub and polished inside an Ar glovebox. The samples were polished by 0.3 μm alpha alumina powder (Buehler Micropolish) on n-Heptane (anhydrous, 99+%, Alfa Aesar)-wetted polishing cloth. The alumina powder and polishing cloth were dried in

vacuum oven overnight before being transferred into the glovebox. After around 10 min of polishing, the LCO samples were ultrasonically cleaned with n-Heptane and wiped by a nonwoven wipe. To avoid exposure to air, the samples were transferred from glovebox into the SEM chamber by Vacushut sample transfer device (Vacushut; Agar Scientific) in a secondary container (Figure 2.2a, b). Under the vacuum environment inside the SEM chamber, the liquid IPA in the Vacushut bag vaporizes, causing the bag to expand and the lid to open. As shown in Figure 2.2c, the Vacushut was mounted onto the SEM sample stage with a custom-machined cube, with the sample surface 90° tilted relative to the beam direction and the lid opened automatically under vacuum environment. Then the sample stage is tilted by 4° to align the sample surface with the indenter.

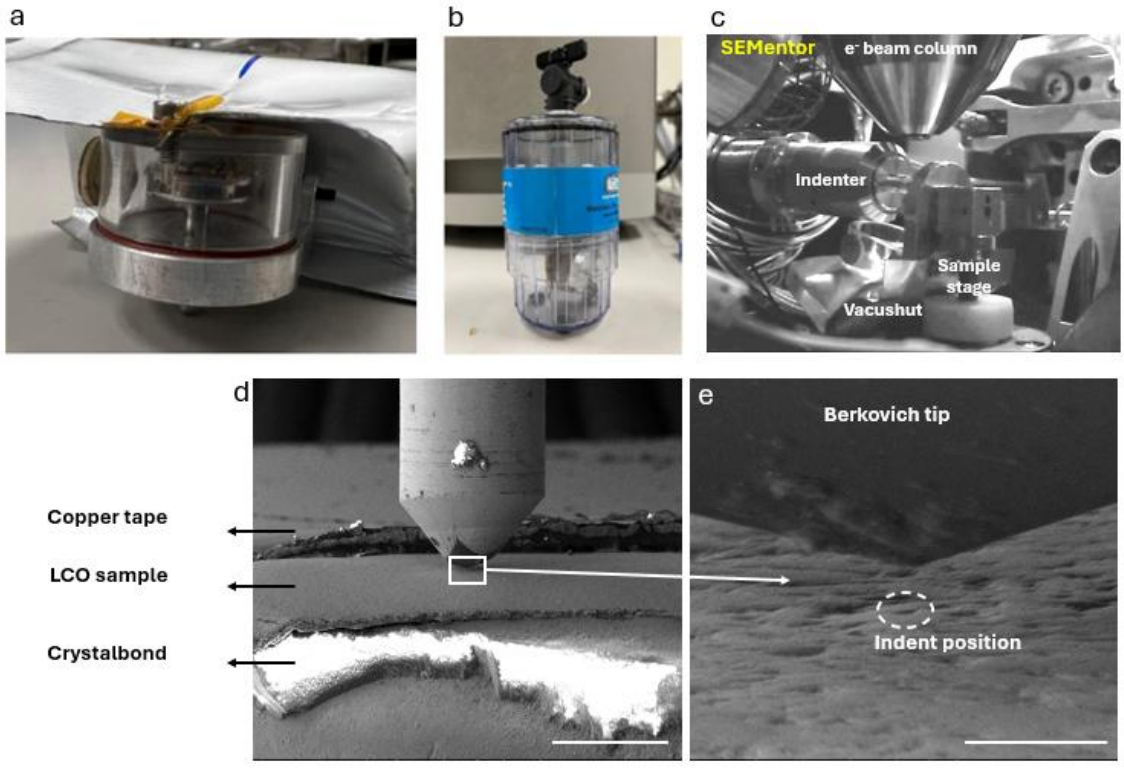

Figure 2.2 Charged LCO sample transfer and nanoindentation experiment set up. a) Vacushut sample transfer device with sample loaded inside. b) Hermetically sealed secondary container to transfer Vacushut between rooms. c) In-situ nanoindentation experiment set up

in a SEM chamber. d) LCO sample mounted on SEM stub by Crystalbond adhesive, with copper tape on top to electrically connect the sample with SEM stub. Scale bar = 400 μm. e) A Berkovich tip is used for nanoindentation tests. The indent position is selected inside the LCO grains. Scale bar = 10 μm.

In-situ nanoindentation experiment was conducted through a nanomechanical instrument (InSEM; Nanomechanics, Inc.) combined with the SEM system (Quanta 200 SEM; FEI). As shown in Figure 2.2d, e, copper tape was applied on the polished sample to electrically connect the LCO with SEM stub, and the sample stage was tilted by 4˚ to align sample surface with the indenter. Standard Berkovich tip was used with a target strain rate of 0.05 s^{-1}. The depth limit was set as 500 nm. Continuous stiffness measurement (CSM) with target frequency of 100 Hz and dynamic displacement of 2 nm was applied to measure contact stiffness changing with indent depth. Indent position was selected inside grains, to avoid influence from grain boundary area.

In the most widely used Oliver-Pharr data analysis procedure, the contact stiffness is only calculated using the data from the initial portion of unloading curve: $S = \frac{dP}{dh}|_{h=hmax}$, where P is the load and h is the indent depth. The contact depth h_c is calculated based on sink-in correction: $h_c = h - \varepsilon\frac{P}{S}$, where ε is a constant dependent on the indenter geometry. For Berkovich tip, $\varepsilon = 0.75$. Under CSM mode, a small oscillation is superimposed on the primary loading signal (Figutre 2.3a), and the small unloading phase in each oscillation period allows a continuous measurement of contact stiffness. As shown in Figure 2.3b, the nano indenter system is simplified with an equivalent stiffness $K = \left(S^{-1} + K_f^{-1}\right) + K_s$ and an equivalent dashpot $D = D_i + D_s$, where S is the measured material contact stiffness. K_f and K_s are the load-frame stiffness and support springs stiffness. D_i and D_s represent damping in the indentation head and in the sample. The contact stiffness is calculated by:

$$S = \left[\frac{1}{\frac{F_0}{z_0}cos\phi - (K_s - m\omega^2)} - \frac{1}{K_f}\right]^{-1} \quad (1)$$

Here, F_0 is the excitation amplitude, z_0 is the displacement amplitude, and ϕ is the phase angle between force and displacement. The indent column mass m and Ks are equipment constants calibrated by the manufacturer. K_f is calibrated together with the area function of our Berkovich tip by indentations into a standard fused silica sample and fitting the modulus result with $E_{fused\ silica}$ = 72 GPa (N = 10, Figure 2.4a).

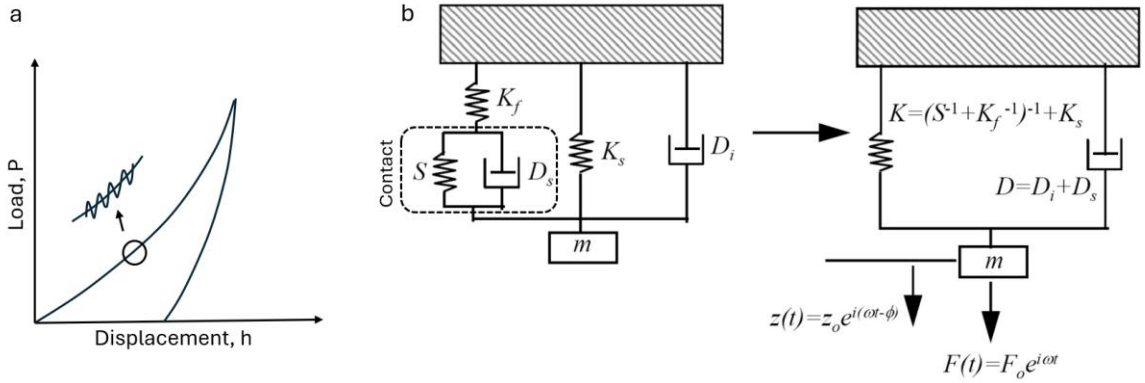

Figure 2.3 Continuous stiffness measurement. a) A small oscillation is superimposed on the primary loading signal for continuous measurement of contact stiffness. b) The indenter system and contact with samples are simplified with equivalent stiffness and equivalent damping.

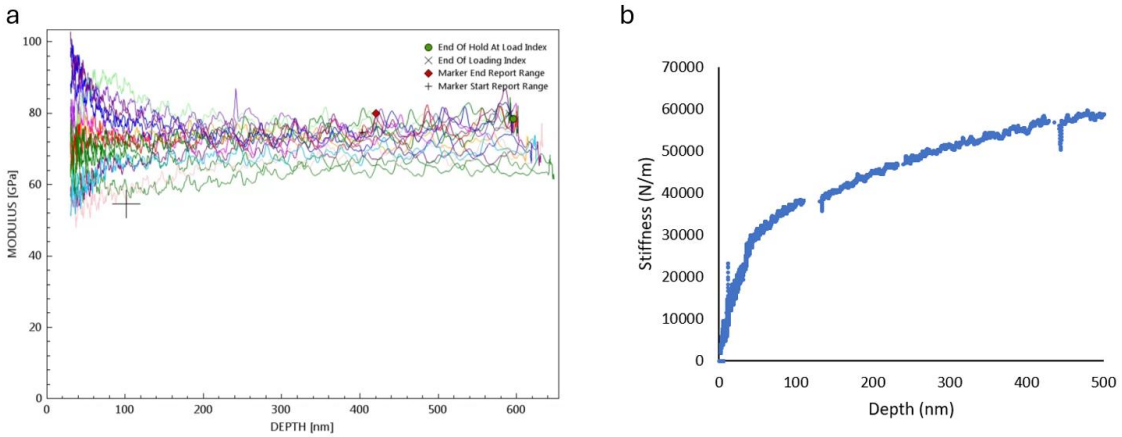

Figure 2.4 Frame stiffness and area function calibration for CSM a) Modulus results from indentations into standard fused silica sample that are applied to calibrate frame stiffness and area function. b) Typical contact stiffness changing with depth of the 100% charged LCO sample.

Elastic modulus can be calculated according to Equation (2) and (3).

$$E_r = \frac{S}{2\beta}\sqrt{\frac{\pi}{A(h_c)}} \tag{2}$$

$$\frac{1}{E_r} = \frac{1-\nu^2}{E} + \frac{1-\nu_i^2}{E_i} \tag{3}$$

Here E_r is the reduced modulus that represents elastic deformation in both sample and tip. β is a geometric constant: β=1.034 for Berkovich tip. E_i and ν_i are Young's modulus and Poisson's ratio of the tip, respectively. For the diamond tip we used, E_i = 1070 GPa and ν_i = 0.07. ν is the Poisson's ratio of measured sample: $\nu_{fused\ silica}$ = 0.17. The calibrated frame stiffness is K_f = 1.4 ×10^5 N/m, with the area function:

$$A(h_c) = 24.5h_c^2 + 7604h_c - 178445h_c^{0.5} + 707154h_c^{0.25} - 564256h_c^{0.125} \tag{4}$$

The typical contact stiffness as a function of depth of the 100% charged LCO sample is shown in Figure 2.6b. The maximum stiffness measured during this test is around 5.8×10^4 N/m, which is close to the frame stiffness and indicates that calibration of frame stiffness needs to be conducted using the experimental setup.

Poisson's ratio of LCO was assumed to be ν = 0.3. The projected area of contact A was computed from the area function and the calculated contact depth h_c. Hardness (H) was defined as Equation 5.

$$H = \frac{P}{A(h_c)} \tag{5}$$

The indent impression of the 100% charged LCO from the same test of Figure 2.6b, the corresponding load-depth data set, and the measured elastic modulus and hardness changing with indent depth are included in Figure 2.5. Several displacement bursts, or pop-ins, were observed in the load-depth curve, corresponding to cracks occurring during the nanoindentation test[52,55,56]. The cracks were also observed in the SEM image of the indent impression. Significant drops in elastic modulus and hardness occurred at the depth where large pop-ins were detected, at 109 nm, 231 nm, and 427 nm for the test shown in Figure 2.5. The drops in stiffness were also observed at the position of 109 nm and 427 nm in Figure 2.6b. Small pop-ins happened even before the depth reached 100 nm. These cracks can lead to lower modulus and hardness results with increasing indentation depth.[56,57] To avoid influence from cracks that occurred during nanoindentation and compare the mechanical properties between samples with different SOC, elastic modulus and hardness were collected at 50 nm indentation depth.

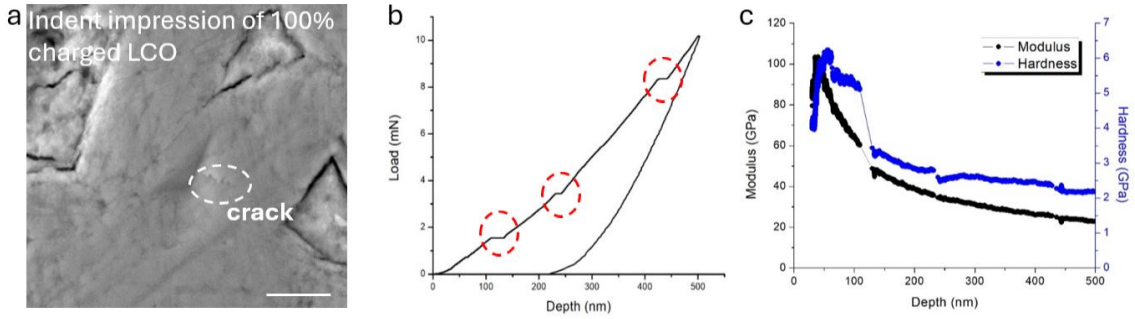

Figure 2.5 Representative nanoindentation results from a 100% charged LCO sample. a) SEM image of an indent impression from the 100% charged LCO sample. Scale bar = 2 μm. b) The corresponding load-depth data set. c) Measured elastic modulus and hardness changing with indent depth.

2.3 Effect of lithiation and delithiation on mechanical properties

In addition to the 100% charged LCO cathodes, in-situ nanoindentation experiments were conducted on 50% charged, 75% charged, 50% discharged, 100% discharged, and the

pristine LCO cathode to investigate the effect of lithiation and delithiation on their mechanical behavior. The typical load vs. depth curves, together with the indent impressions from the same tests, are shown in Figure 2.6, where cracks were observed during indentation tests in every group of samples.

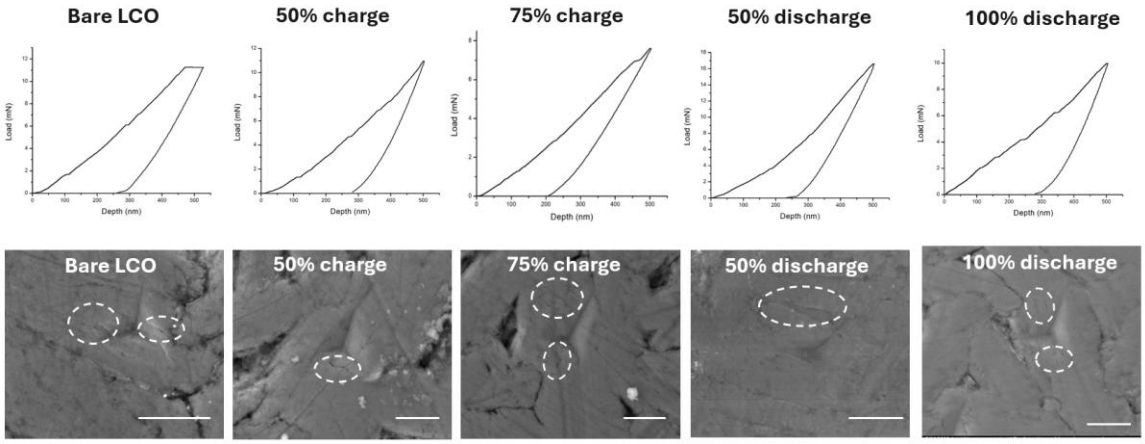

Figure 2.6 Nanoindentation load-depth data sets and the corresponding indent impressions from the pristine LCO sample, as well as samples that are 50% charged, 75% charged, 50% discharged, and 100% discharged. Scale bar = 2 μm.

The average values of elastic modulus and hardness with different SOC are summarized in Figure 2.7 (n=10), revealing that the modulus and hardness decrease when LCO is charged and recover to a value close to the pristine LCO when it is fully discharged. The elastic modulus of the pristine LCO is measured to be 119.0 ± 24.7 GPa, which then decreases linearly with increasing SOC. The fully charged LCO cathode displays a modulus of 87.5 ± 7.4 GPa, showing a 26% reduction compared to the pristine sample. We also notice that when the sample is fully discharged and the first cycle is finished, the elastic modulus recovers to 115.6 ± 8.9 GPa, a value similar to the pristine LCO. The same tendency is observed in the hardness of the electrodeposited LCO cathodes. The hardness experiences a 33% decrease from 8.9 ± 4.0 GPa to 6.0 ± 1.1 GPa when the LCO is fully charged and then recover to 9.6 ± 2.1 GPa after 100% discharging. While there is no obvious change in modulus or hardness

after the first cycle, nanoindentation tests are also conducted on LCO sample after 60 cycles, 100% discharged. After 60 cycles, the electrodeposited LCO exhibits around 20% decrease in modulus and 30% decrease in hardness compared with bare LCO and fully discharged LCO after 1st cycle, showing a modulus of 96.7 ± 8.0 GPa and a hardness of 6.8 ± 1.6 GPa.

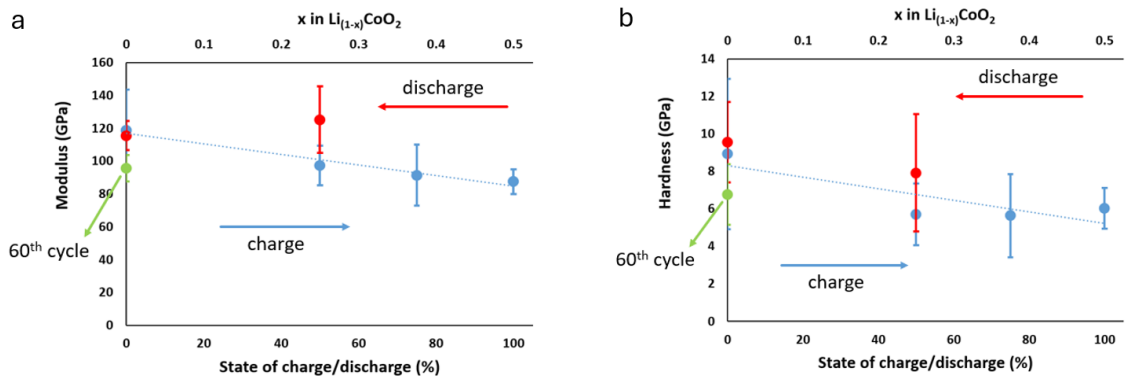

Figure 2.7 Elastic modulus and hardness of LCO with different SOC.

In 2012, Qu et al. reported modulus in the range of 151-236 GPa and hardness of 11.7 ± 3.8 GPa by nanoindentation on individual grains of dense LCO ceramic pellets after sintering, with indent load of 2 mN at around 100 nm depth.[55] No detectable crack formed during their indentation under 2 mN load. In comparison, our pristine LCO sample shows a modulus 21% below the lower limit and a 23% lower hardness, despite that our nanoindentation tests were done along the near-[110] orientations, which is expected to show higher modulus than the crystal orientations closer to c-axis according to the theoretical calculation based on a strain energy approach.[50] More detailed characterization and discussion about the crystallographic orientation of the electrodeposited LCO sample is provided in section 2.5. The low mechanical properties of this electrodeposited LCO cathode can be attributed to the vacancies formed between the LCO grains during electrodeposition. Gaps are observed along the grain boundaries in Figure 2.5 and 2.6. Porosity under 10% can lead to significant drop in modulus and hardness of ceramic materials.[58,59] Although we have carefully selected the indent position inside the grains, the small width of less than 5 μm of the LCO crystal

platelets does not allow enough space to completely avoid the influence from the week grain boundary area.

To better understand the morphology influence on LCO mechanical properties, nanoindentation mapping was conducted using FemtoTools (FemtoTools AG; FT-NMT04) on a 50 μm × 50 μm area of a pristine LCO sample with a larger grain size (Figure 2.8a, b). The indent position was set in an array with point spacing of 2 μm. The load rate was set as 0.1 μm/s and the depth limit was 200 nm, which is ten times smaller than the point spacing. As shown in the hardness and modulus maps overlapped with SEM images in Figure 2.8c and d, the regions near grain boundary are mainly in blue and purple colors which represent lower hardness and modulus compared with the grain interior.

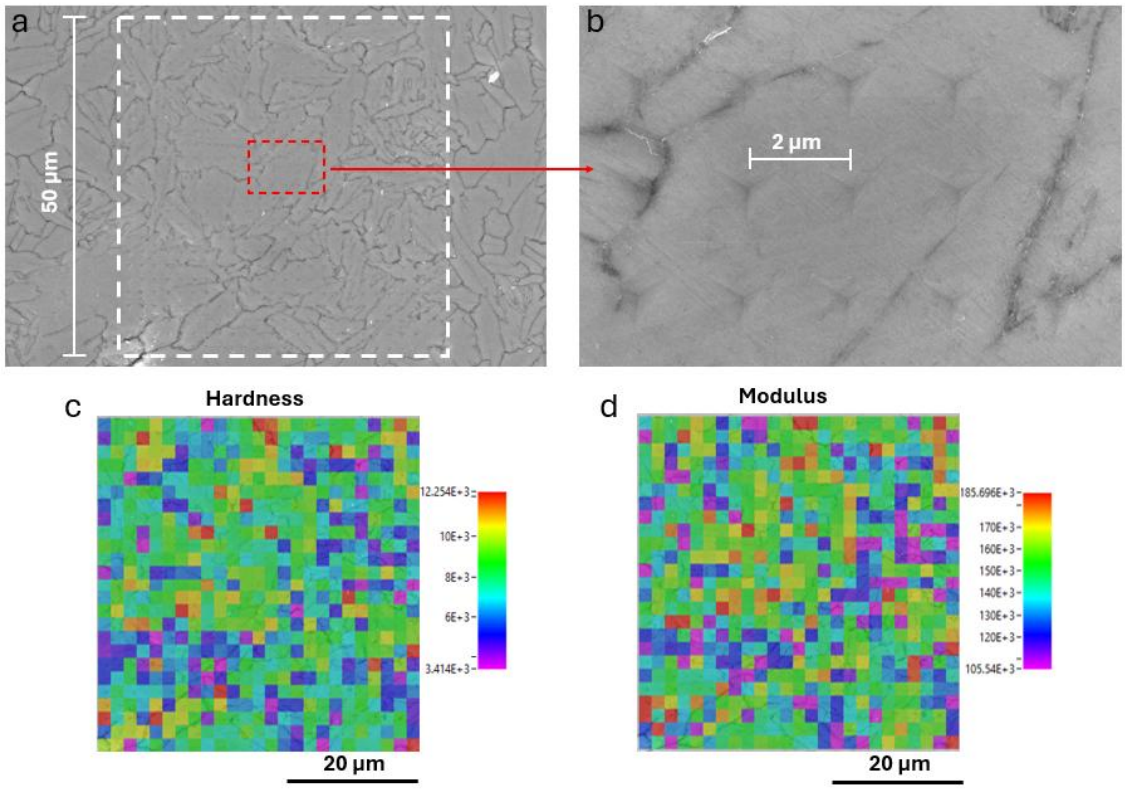

Figure 2.8 Nanoindentation mapping on pristine LCO sample with a larger grain size. a) A SEM image of the 50 μm × 50 μm polished LCO surface for nanoindentation mapping. b) A

zoomed-in SEM image of the indent impression. Indent position is set in an array with point spacing of 2 μm. c) Hardness and d) modulus maps calculated based on the nanoindentation result and overlapped with the SEM image.

The decrease of mechanical properties in charged LCO can be attributed to deintercalation of Li from the LCO crystal and the expansion of the layered structure along c-axis. In 2015, Wu et al. revealed a linear relationship between the Young's modulus and ultimate strength of Li_xCoO_2 with the Li concentration in LCO crystal using first principles calculations.[50] The calculation results indicate that the deintercalation of Li from the layered crystal structure causes a weaker Co-O bond, thus leading to decreased mechanical properties. Experimentally, Swallow et al. showed a 40% decrease of modulus and a 50% decrease of hardness in charged LCO, through nanoindentation on dense and sintered LCO pellets.[52] However, their modulus and hardness did not decrease with further charging, and all of the charged samples with charging times varying from 50 to 500 hours at C/1000 charge rate exhibited similar mechanical properties. It was found that the surface of the dense, thick LCO pellets was overcharged, and the degradation of mechanical properties was caused by microstructural damage of the polycrystalline samples, together with chemical expansion and phase changes occurring upon lithium deintercalation.

In this work, a linear decreasing tendency in both modulus and hardness with SOC is detected. Recovery of modulus and hardness in the discharged samples indicate that the effect from the possible cracks that occur during charge/discharge process is negligible, at least for the first cycle. Therefore, the linear decrease in elastic modulus and hardness with increasing SOC is likely due to Li deintercalation and expansion of the layered structure along c-axis, reflecting changes in the intrinsic properties of the material. Additionally, the ~ 20% decrease in modulus and ~30% decrease in hardness after the 60^{th} cycle can be attributed to the microstructural damage that happened during long-term cycling.

2.4 Distribution of fracture toughness through electrode cross-section

Fracture toughness serves as a key material parameter for predicting crack stability and its propagation under stress. To understand how structural heterogeneity and electroplating contributes to the mechanical property landscape, we performed nanoindentations on a cross-sectional LCO sample using a Berkovich indenter tip in a nanoindenter (FemtoTools AG; FT-NMT04). To prepare a smooth plane on the cross-section of LCO sample for nanoindentation test, FIB milling (FEITM; Versa 3DTM DualBeamTM) was used to polish an area of around 200 µm × 15 µm. The ion beam direction was perpendicular to the LCO surface with an accelerating voltage of 30keV. 50nA, 10nA, and 5nA ion beam currents were applied sequentially to reduce the roughness. The SEM images of the FIB-milled cross section are shown in Figure 2.9a and b.

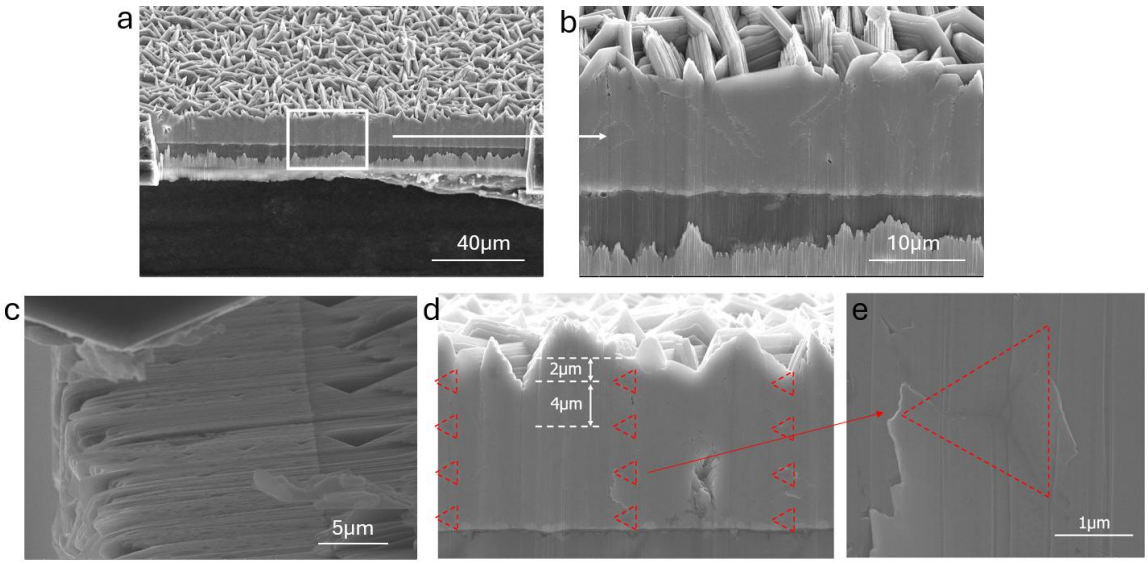

Figure 2.9 Experimental set up for nanoindentation on LCO cathode cross-section. a, b) SEM images of FIB-milled cross-section for nanoindentation tests. c) A Berkovich diamond tip is used to conduct tests and the metal layer under the LCO is used as reference to find contact. d) SEM image of the LCO electrode cross-section after nanoindentation. The residual indents are marked as red triangles. e) An individual indent mark.

In-situ nanoindentation test on the FIB milled cross section was conducted with a Berkovich diamond tip inside the SEM system and the metal layer under the LCO was used as reference to find contact (Figure 2.9c). The indentation positions were set in lines perpendicular to the sample's surface, with 4 points in each line at different layers (Figure 2.9d). The point spacing in a line was 4 μm, and the lines were separated by more than 10 μm. Load was applied with a rate of 100 μN/s till the depth limit (400 nm) was achieved. Figure 2.9e depicts the remaining indentation marks with radial and lateral cracks emanating from the sharp corners, which serve as sufficiently high stress concentrations for crack initiation. A typical load vs. displacement curve is shown in Figure 2.10. Several displacement bursts, or pop-ins, are observed in the curve, corresponding to cracks that formed during the nanoindentation test.

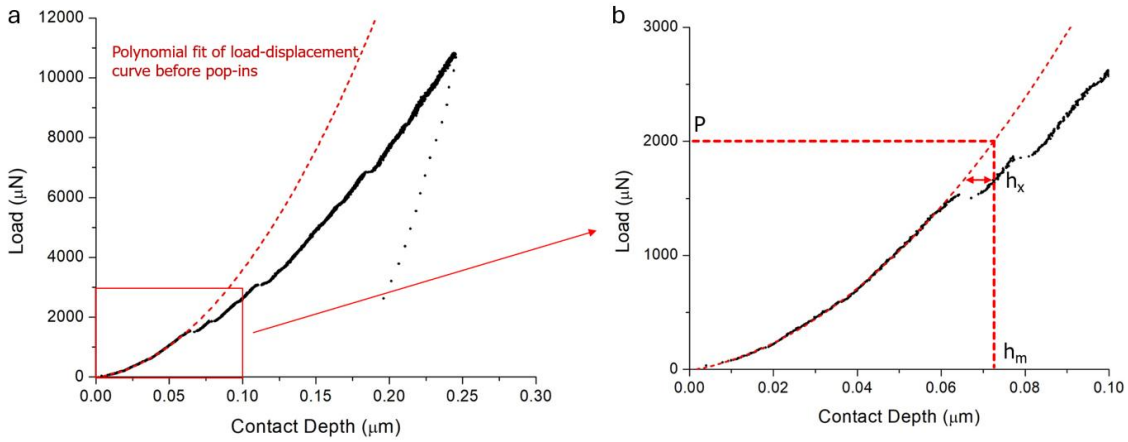

Figure 2.10 Typical load-displacement data of nanoindentation test on LCO cross-section. a) Load-displacement curve with pop-ins corresponding to cracks. The red dotted line shows a polynomial fitting of the load-displacement curve prior to the first pop-in. b) Definition of the real displacement with pop-ins h_m and the extra displacement caused by the crack h_x.

The fracture toughness (K_{Ic}) can be determined via the indentation-induced pop-ins[60,61], and this pop-in method has been used to measure K_{Ic} of LCO electrodes[52,55]. Crack length c was calculated based on the displacement burst as

$$c = \sqrt{2}h_m + (Q\frac{E}{H} - \sqrt{2})h_x \quad (6)$$

Here h_m was the real displacement with pop-ins and h_x was the extra displacement caused by the entry of the tip into the crack. Definition of h_m and h_x is illustrated in Figure 2.10b. The red dotted line represents the polynomial fit of load-displacement curve before the first pop-in. The indentation load P used to determine h_m and h_x was in the range of 600-6000 μN before the second pop-in was observed. Q is a unitless constant of 4.55 according to Field's work.[61] Fracture toughness of different layers was then calculated as

$$K_{Ic} = k(\frac{E}{H})^{\frac{1}{2}}\frac{P}{c^{3/2}} \quad (7)$$

Research has shown that the constant k mainly depends on the geometry of the indenter [60,62]. Following Jang's work[62], we estimate k = 0.028 from Equation (8), where Ψ is the half opening angle of the indenter (Berkovich tip Ψ = 65.3°).

$$k = \frac{0.0352}{(1-\nu)}(cos\Psi)^{\frac{2}{3}} \quad (8)$$

We find that in its pristine state, the electrode displays a similar fracture toughness along its height, with the average toughness ranging from 0.73 to 0.75 MPa·m$^{0.5}$, with the layer adjacent to the current collector having a higher fracture toughness of 1.00 ± 0.16 MPa·m$^{0.5}$ (Figure 2.11a). The lower porosity near the current collector can explain the greater fracture toughness in that location compared to the rest of the electrode (Figure 2.12a).

After delithiation to 3.6 V vs. LiIn (4.2 V vs. Li), fracture toughness around the current collector decreases to 0.8 MPa·m$^{0.5}$, a 20% decrease compared to pristine LCO (Figure 2.11b). The fracture toughness measured along the electrode cross-section, at distances of 5, 9, and 13 μm from the current collector, are distributed in the range of 0.66 to 0.77 MPa·m$^{0.5}$. Studies of lithium transition metal oxides have observed a similar reduction in fracture toughness after charging and attributed it to charging-induced Li depletion, residual stress, and micro-crack generation.[52,57] Our results indicate that the material in the vicinity of the

current collector experiences the largest change in fracture toughness of 20% and lowest active material utilization (minimal delithiation), which suggests that Li depletion is unlikely to be the root cause for the fracture toughness variation. Most likely, it is the creation of pores, nano-cracks, and voids that drive fracture toughness reduction. This is consistent with our observation that the fracture toughness becomes more uniform throughout the remaining thickness of the LCO electrode, following the porosity gradient (Figure 2.12a, b).

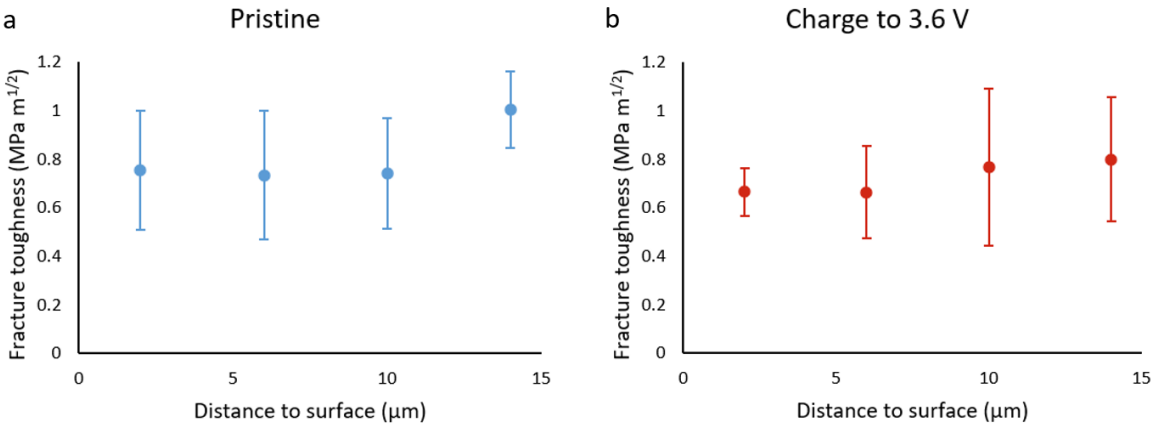

Figure 2.11 Fracture toughness, calculated from displacement bursts (pop-ins) in load-displacement data corresponding with crack formation, as function of distance away from sample surface for (a) pristine (n = 7) and (b) charged LCO (n = 4-6).

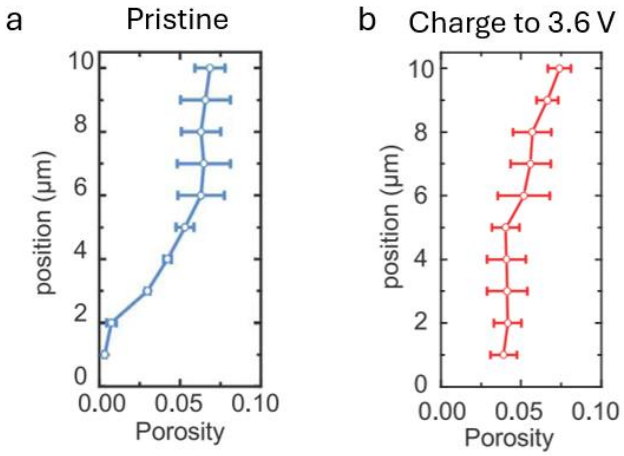

Figure 2.12 Porosity variation along the thickness in LCO electrode a) pristine and b) charged, with position 0 at the current collector surface.

2.5 Crystallographic orientation of electrodeposited LCO

LCO crystal's mechanical properties are largely dependent on crystallographic orientation, and the electrodeposited samples usually have preferred grain growth direction. Therefore, it is important to identify the crystallographic texture of the electrodeposited LCO cathodes. EBSD measurements were conducted on both LCO surface and cross-section, which were progressively polished by 0.3 µm and 0.05 µm alpha alumina powder (Buehler Micropolish). EBSD maps were acquired at an accelerating voltage of 20 kV using the EBSD detector (HKL Nordlys II, Oxford Instruments) in a SEM system (LEO 1550 VP, Zeiss). The specimen was tilted to 70° with respect to the beam normal and the step size was set as 0.08 µm. Lattice parameters used for crystallographic evaluation are listed in Table 2.1.

Table 2.1 Lattice parameters for LCO used in EBSD analysis[63]

Lattice parameters	
Space group/number	R-3mH/166
a, b (nm)	2.8147
c (nm)	14.0466
α, β (°)	90
γ (°)	120

Figure 2.13a contains the SEM image of the polished sample surface with the EBSD test region outlined by a rectangular dashed line. The grain orientation map of the sample surface is shown in Figure 2.13b, with color based on the specimen z-axis inverse pole figure. The average mean angular deviation (MAD) value over the whole set of electron backscatter diffraction patterns on sample surface was 0.69°, with an indexing rate of 38.61%. Inverse pole figure and pole figure were generated based on the EBSD orientation measurements (Figure 2.3d, e). Inverse pole figure in Z0 direction (surface normal) revealed a dominant (110) texture out of the surface plane, with significant intensities at near-[110] orientations. As shown in the {001} pole figure, the [001] crystal direction mainly arranges in the X0-Y0 plane, which is the surface plane of the sample.

The EBSD result of the mechanically polished cross-section is shown in Figure 2.14, with a MAD value of 0.70° and an indexing rate of 39.03%. The grain orientation map is colored based on Z0 inverse pole figure, with Z0 direction normal to the cross-section plane (Figure 2.3b, c). Inverse pole figure in Y0 direction shows significantly high intensity at the [110] orientation (Figure 2.14d), and the [001] crystal direction lays in the X0-Z0 plane according to the {001} pole figure (Figure 2.14e). This result is consistent with the sample surface, indicating a preferred orientation of [110] out of the electrodeposited LCO sample surface and the crystal c-axis randomly arranged in the surface plane.

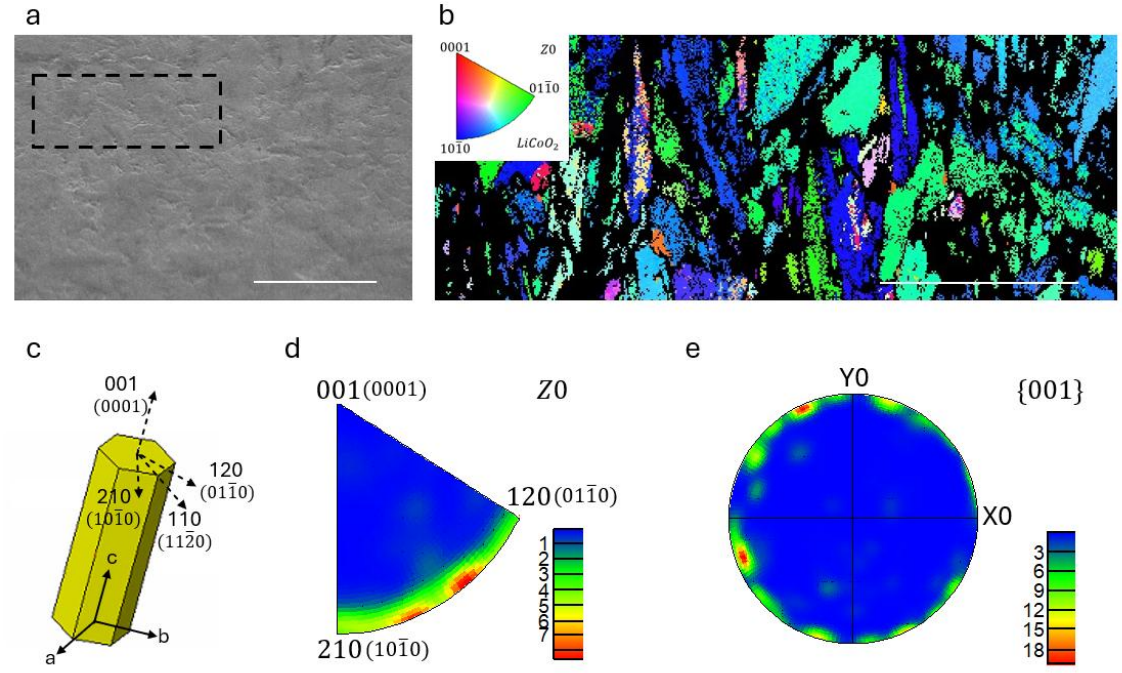

Figure 2.13 EBSD analysis on LCO sample surface. a) SEM image of the polished sample surface for EBSD measurement. b) Grain orientation map colored based on the specimen z-axis inverse pole figure. c) LCO crystal orientation index. d) Inverse pole figure in Z0 direction (surface normal). e) {001} pole figure.

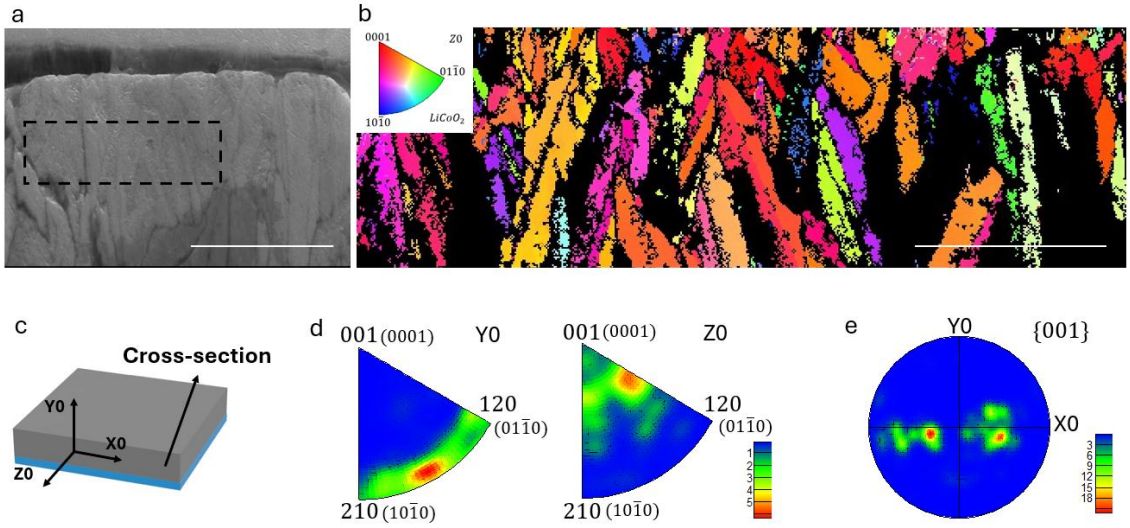

Figure 2.14 EBSD analysis on LCO cathode cross-section. a) SEM image of the polished cross-section. The EBSD test region is outlined by a rectangular dashed line. b) Grain orientation map colored based on the specimen z-axis inverse pole figure. c) Specimen coordinate system for the test on cross-section. d) Inverse pole figure in Y0 direction (surface normal) and Z0 direction (normal to the cross-section). e) {001} pole figure.

2.6 Summary

To determine the mechanical properties of charged LCO crystals and avoid the effects of grain boundaries and air-exposure, in-situ nanoindentation experiments were conducted in a custom mechanical testing system within a SEM. Our results show a decrease in elastic modulus and hardness with increasing SOC, which can be attributed to the deintercalation of Li from the crystal lattice and the expansion of the layered structure of LCO. The recovery of mechanical properties during discharge indicates that the changes in measured mechanical properties mainly originate from changes in Li concentration rather than intergranular fracture during cycling. The fracture toughness at various depths in the LCO electrode is determined via nanoindentation on FIB-milled cross section and calculated based on the displacement caused by crack formation. After delithiation, the fracture toughness in the layer closest to the current collector decreases by 20%, driven by the formation of pores, nano-cracks, and voids during charging. Considering the anisotropy of the LCO, EBSD analysis is utilized to clarify the preferred crystallographic orientation of the electrodeposited LCO cathode, enabling the correlation between crystallographic orientation and measured mechanical properties. By establishing the relationship between mechanical properties and the degree of delithiation, this work provides experimental insights for understanding mechanical degradation and for informing electro-chemo-mechanical modeling of lithium-ion battery electrodes.

. C h a p t e r 3

DEFORMATION OF LITHIUM-BASED COMPOSITE ANODES

3.1 Overview

In lithium metal batteries with solid electrolyte, the deformation behavior of lithium anodes under externally applied stack pressure plays an important role in influencing dendrite growth and interfacial stability. Alkali metals, such as lithium and sodium, crystallize in a body-centered cubic (BCC) structure. Metallic lithium and sodium are both known to exhibit size effects, leading to size-dependent mechanical performance at reduced length scales. In practical solid-state batteries, both lithium dendrites and interfacial voids typically develop at submicron to micron scales, where such size effects may significantly influence deformation behavior. However, experimental characterization of the micromechanical properties of Li and Na remains limited due to their high chemical reactivity and the stringent environmental control requirements.

This chapter investigates the deformation behavior of two types of lithium-based composite anodes designed to mitigate interfacial degradation in solid-state batteries (Figure 3.1). The first system is a Li/ reduced graphene oxide (rGO) composite anode, where the carbon-based framework beneficially functions as a bridging material to deliver Li and retain contact with the electrolyte during Li stripping, thus enhancing the stripping capacity at low stack pressure.[64] The second system is a Li/Na composite anode, in which sodium is expected to serve as a soft metallic filler that enhances the deformability of the composite electrode and maintains the interface contact without requiring high stack pressures.[65]

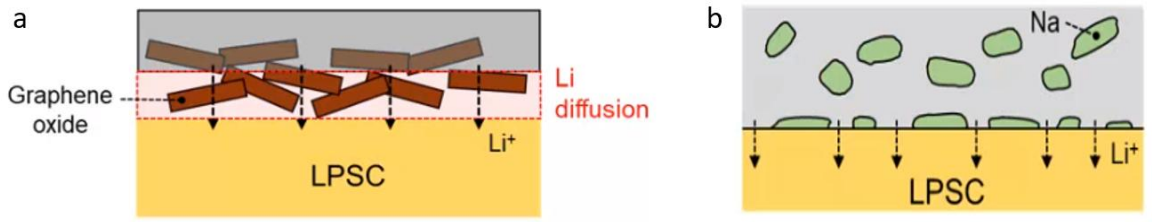

Figure 3.1 Schematic illustration for the a) Li/Na composite anodes and b) Li/rGO composite anodes.

The deformation behavior of lithium-based composite anodes is investigated using in-situ micro-scale mechanical characterization. Micro-pillar compression experiments are conducted on Li/rGO composite anodes with different carbon contents. The results reveal that increasing rGO content introduces hollow regions that significantly reduce the modulus and strength of the composite pillars. In addition, nanoindentation experiments are performed on Li/Na composite anodes to evaluate the mechanical response of the composite system. The results show that introducing Na into the Li matrix reduces the elastic modulus of the composite while the hardness remains in a similar range of 9.5-11.8 MPa whichis higher than the bulk material due to size effect. Site-specific indentation of individual phases further reveals that the Na phase exhibits ~54% lower hardness than Li phase under 500 nm indent depth, suggesting that the soft Na filler can more easily deform during lithium stripping, thereby reducing void formation and improving interfacial contact with the solid electrolyte.

3.2 Micro-pillar compression of lithium-graphene oxide anodes

The deformation behavior of Li/rGO anodes with 3.9 wt%, 7.6 wt%, 9.9 wt%, 13.2 wt%, and 18 wt% carbon fractions, along with pure Li metal, was studied via uniaxial compression experiments on FIB-milled micro-pillars. The composite films were mounted onto SEM stubs inside an argon glovebox, and the sample surface was cleaned by a razor blade. To avoid exposure to air, the samples were transferred from glovebox into the SEM chamber by Vacushut sample transfer device. As shown in Figure 3.2a, the sample stage was tilted by

52˚ from the e-beam direction with the sample surface facing the ion-beam column. The micro-pillar was prepared at the edge of the surface by Ga-ion FIB milling in VERSA 3D DualBeam SEM (Figure 3.2b, c). The aspect ratio of the micro-pillar was controlled to be around 2:1, with diameters in the range of 5-6 μm.

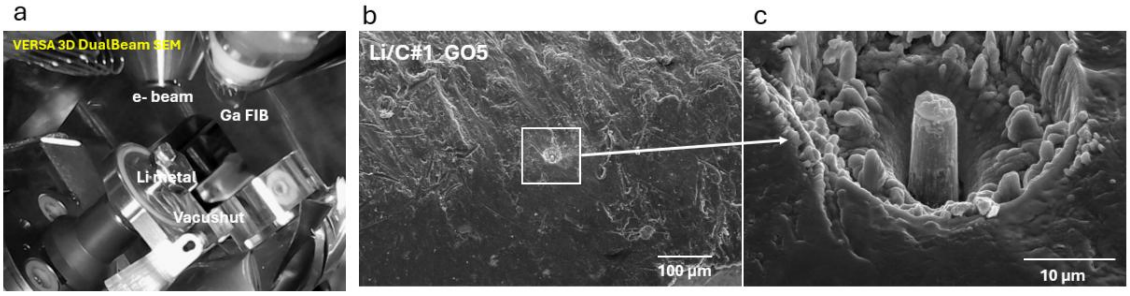

Figure 3.2 Preparation of Li/rGO micro-pillars. a) Experimental setup in a SEM chamber. Li/rGO is loaded in Vacushut with the lid automatically opening under vacuum environment. Sample stage is tilted by 52° to align the sample surface with the ion-beam column. b) SEM image of a micro-pillar prepared on the edge of 3.9 wt% C sample surface. c) Zoomed-in SEM image of the micro-pillar prepared via FIB milling.

Using the pillar prepared on the 3.9 wt% C sample as an example, the C, O, and Ga element maps from energy-dispersive X-ray spectroscopy (EDS) analysis (Bruker XFlash, Bruker ESPRIT) are included in Figure 3.3. The element maps show remaining oxygen contamination and gallium deposition on the top layer of the micro-pillar, while the side face of the pillar is clean and the pillar under the surface layer was not contaminated by Ga-ion. Vacushut was then loaded on a cube to tilt the sample by 90° and ion beam with high current (30nA) was used to polish away the top layer of micro-pillar (Figure 3.4).

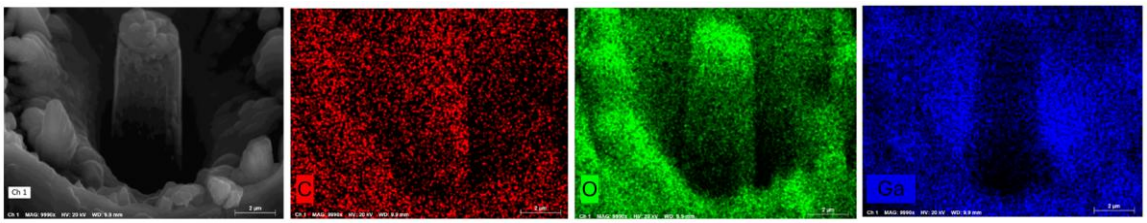

Figure 3.3 Carbon, oxygen, and gallium element maps from EDS analysis of a micro-pillar after Ga-ion FIB milling.

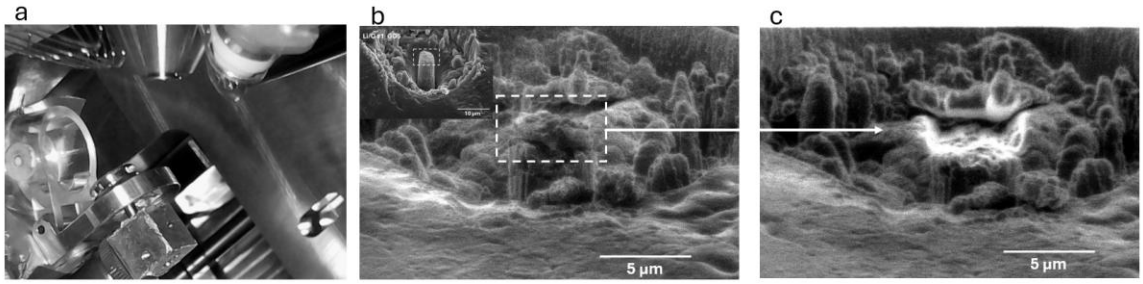

Figure 3.4 Removal of the contamination layer by high-current FIB milling. a) Vacushut is loaded on a cube to tilt the sample by 90° from the ion-beam direction. Ion-beam images b) before and c) after high-current FIB milling to remove the contamination layer. Inset in b) 52° tilted SEM image of the pillar before high-current FIB milling. The contamination layer on top of the pillar is outlined by a rectangular dashed line.

The Li/rGO micro-pillar was transformed to SEMentor by Vacushut and compressed using a diamond flat punch tip with 5 µm diameter. The strain rate was set as 1×10^{-3} s^{-1}. Sneddon's correction was applied to eliminate the deformations of indenter and substrate according to the equation:

$$\Delta x_{pillar} = \Delta x_{total} - \frac{(1-\nu_{sub}^2)\cdot f}{2E_{sub}\cdot r_{base}} - \frac{(1-\nu_{ind}^2)\cdot f}{2E_{ind}\cdot r_{top}} \quad (9)$$

Here, Δx_{total} was the measured displacement and f was the load. For the diamond tip, the Young's modulus and Poisson's ratio of the indenter were E_{ind} = 1141 GPa and ν_{ind} = 0.07.

Poisson's ratio of substrate was assumed to be v_{sub} = 0.36 for Li metal. Young's modulus of substrate, E_{sub}, was estimated from the slope of elastic segment of engineering stress-strain curve. The radius of the loaded area at the base r_{base}, and at the top r_{top} were measured from the SEM image of the pillar. The engineering stress-strain curves for the micro-pillars fabricated on the Li/rGO films with carbon fractions varying from 3.9 wt% to 18 wt%, as well as the pure Li micro-pillar, are shown in Figure 3.5. After full contact was established, all of the samples exhibited an elastic loading segment followed by plastic flow, ultimately ending in catastrophic failure.

The mechanical properties are summarized in Figure 3.6. The Young's modulus (E) was obtained from the slope of elastic segment of loading curve. The yield strength ($\sigma_{0.2\%ys}$) is defined as the stress that will result in a plastic strain of 0.2%. And the flow stress (σ_{flow}) is defined as the stress at which the first significant strain burst occurs. The pure Li metal exhibits an average Young's modulus of 2.6 GPa, yield strength of 31 MPa, and flow stress of 43 MPa. The mechanical properties of Li/rGO anodes with high carbon fraction (13.2wt% and 18wt%) show significant decrease compared with the pure Li metal. For example, the sample with 13.2 wt% carbon shows E = 0.72±0.18 GPa, $\sigma_{0.2\%ys}$ = 16±3 MPa, and σ_{flow} = 22±7 MPa, which are 72%, 48%, and 49% smaller than pure Li metal, respectively.

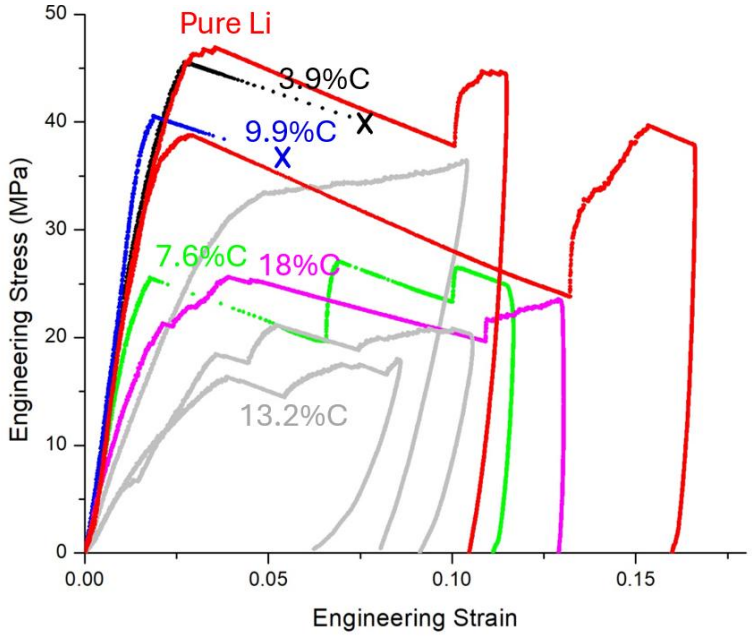

Figure 3.5 Engineering stress-strain curves for the micro-pillars fabricated on the Li/rGO films with carbon fractions of 0 wt%, 3.9 wt% 7.6 wt%, 9.9 wt%, and 18 wt%.

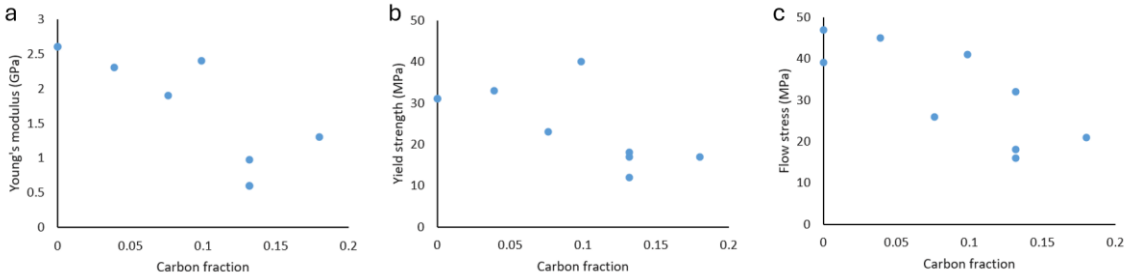

Figure 3.6 Mechanical properties as a function of carbon fraction. a) Young's modulus, b) yield strength, and c) flow stress measured from the micro-pillars changing with carbon fraction.

Due to the diversity of experimental methods and test environments, the elastic modulus for polycrystal bulk Li has been reported in a wide range of 1.9-7.9 GPa.[66–68] In 2023, Darngrough et al. reported that the Li elastic modulus measured by nanoindentation testing

of individual grains varies from 3 GPa to 28 GPa, depending on the crystal orientation.[69] Although we were not able to measure the crystal orientation of the Li pillars we tested on, our result shows a relatively low Young's modulus of 2.6 GPa for pure Li metal, which is close to the reported value of E = 3.0±0.5 GPa from a {0.1 0 1} grain[69] and the lower limit of 3.1 GPa along [100] crystal direction among different orientation, calculated via the equation for bcc metal:

$$\frac{1}{E_{hkl}} = S_{11} - 2(S_{11} - S_{12} - \frac{1}{2}S_{44}) \cdot \frac{h^2k^2+h^2l^2+k^2l^2}{(h^2+k^2+l^2)^2} \quad (10)$$

Here *h*, *k*, and *l* are the miller indices and the elements of compliance matrix S_{11}, S_{12}, S_{44} are calculated based on the room temperature elastic constant C_{11}, C_{12}, C_{44}[70]. The Young's modulus consistent with pristine Li also suggests that the possible atmospheric contamination did not significantly affect the measured mechanical response. Different from the elastic modulus, the plastic properties of Li metal show obvious size effect. While the yield strength of bulk Li is reported in the range of 0.41-1.26 MPa[66,71,72], the value can increase by two orders of magnitude when measured in micro- or nano-scale. Xu et al. demonstrated that the yield strengths increase from 15 to 105 MPa at room temperature with pillar diameter decreasing from 9.45 to 1.39 μm by uniaxial compression experiments.[19] The size effect in Li metal is also detected by nanoindentation[72,73], and we will discuss in more detail in section 3.2. This work shows a flow stress of 43 MPa for pure Li metal, which is consistent with Xu's result of ~50 MPa from an un-oxidized 4.17 μm Li pillar.

The low modulus and strength in high C loading samples are attributed to the hollow structure in the graphene influenced region. The rGO sheet position was determined via carbon element mapping from EDS analysis on a FIB-milled cross-section by the Li/rGO film edge (Figure 3.7b). In Figure 3.7a, the corresponding SEM image shows that the graphene influenced region is highly porous compared with pure Li area. The hollow structure remained in the pillar that was prepared in the same region and was marked with the red circle in Figure 3.7c. We also notice that the size of rGO sheet and the spacing

between the sheets are in the range of several micrometers for the Li/rGO film with 13.2wt% C, which are comparable with the pillar diameter. Therefore, the mechanical behavior measured from the micro-pillars on Li/rGO films may largely be influenced by the individual pillar's position. Whether or not a hollow graphene region is included in the pillar and the hollow region fraction can significantly affect the test result. For low carbon loading samples, likely no graphene region is included in the micro-pillars, so that their deformation behavior is identical with Li metal. The SEM images before and after compression test of a pure Li pillar and a Li/rGO composite pillar with 7.6 wt% C are included in Figure 3.8. The video of representative compression test and corresponding load-displacement curve are provided in Supplementary Material. In pure Li micro-pillars, the initial displacement burst happened with a shear avalanche via single slip. In comparison, for the Li/rGO composite pillars, multiple cracks occur in the hollow region, resulting in lower modulus and yield strength in high carbon loading sample.

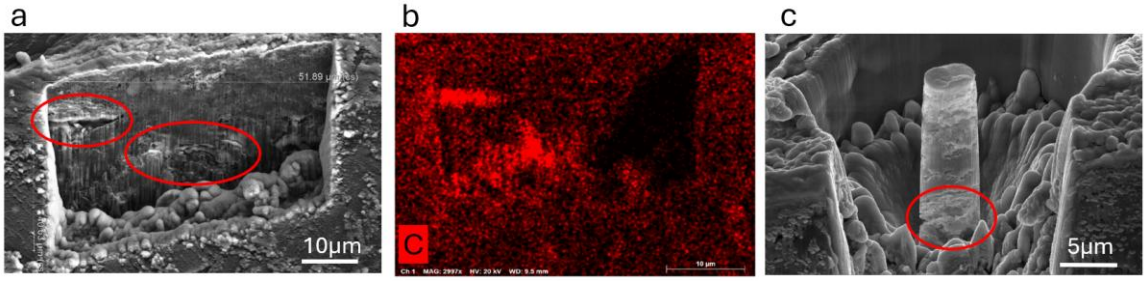

Figure 3.7 Hollow structure in the graphene influenced region. a) A 52° tilted SEM image of a FIB-milled cross-section including the graphene influenced region. b) Carbon element map from EDS analysis showing rGO sheet position. c) A SEM image of the micro-pillar prepared on the same region. The graphene influenced hollow regions are marked with red circles.

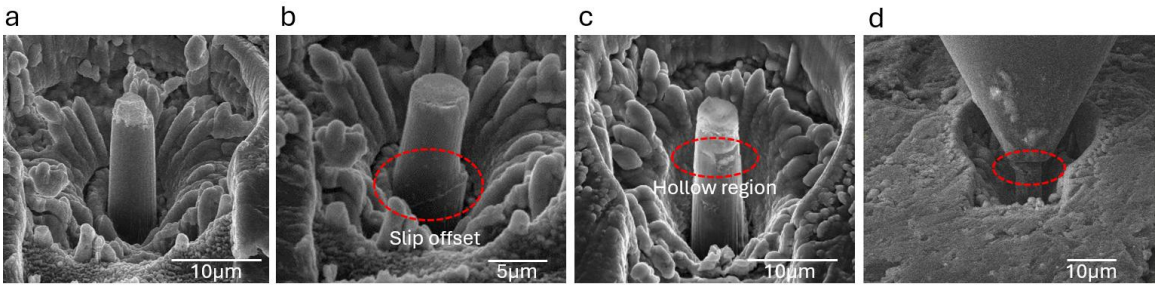

Figure 3.8 SEM images before and after micro-pillar compression tests. SEM images of a pure Li pillar a) before and b) after shear avalanche via single slip. SEM images of a Li/rGO composite pillar c) before and d) after cracks in the hollow region.

3.3 Nanoindentation on lithium-sodium anodes

In-situ nanoindentation experiment was conducted through the nanomechanical instrument (InSEM; Nanomechanics, Inc.) combined with SEM system (Quanta 200 SEM; FEI) on Li/Na composite films with 2.5 at.% and 20 at.% Na, as well as on pure Li and Na metal. The sample surface was cleaned by a razor blade inside an argon glovebox, and the sample thickness is larger than 100 μm. A Berkovich tip was used with target strait rate of 0.05 s^{-1} for the nanoindentation tests. The depth limit was set as 2 μm and the tip was held at maximum load for 1 s. Figure 3.9a shows the 2.5 at.% Na sample cross-section, where clearly identifiable phases can be observed: the bright region corresponds to Na, and the dark matrix is Li.

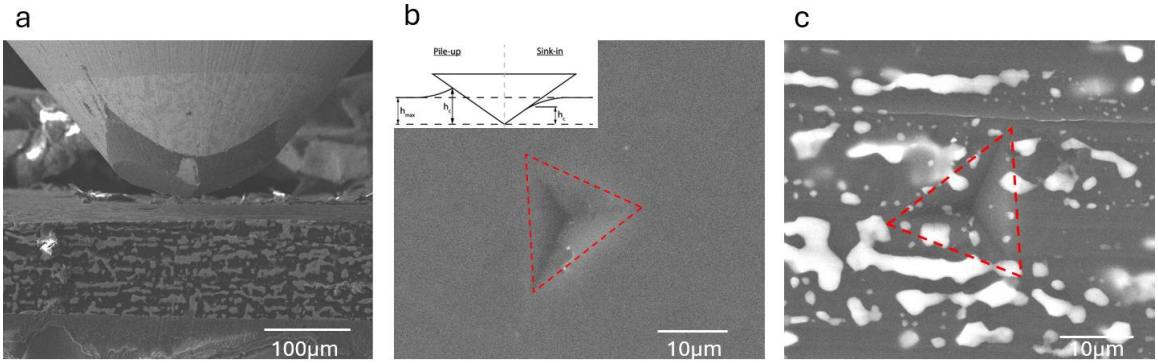

Figure 3.9 Nanoindentation tests on Li/Na composite films. a) A Berkovich tip is used for nanoindentation tests on Li/Na composite film. SEM images of the indent impression from b) pure Li and c) 2.5 at.% Na composite film. Inset in b) Illustration of pile-up and sink-in effects.

The data analysis process is the same as presented in section 2.2. The only difference comes from the correction of so-called pile-up effect, or the additional extruded material around the nanoindentation boundary that the residual nanoindentation impressions indicate in Figure 3.9b and c. Due to the large E/H ratio of Li and Na, pile-up effect has been observed in both metals.[72,74] Such pile-ups have been associated with a deeper contact depth (h_c) compared to the measured indenter penetration depth (h). For example, Fincher et al. showed that the measured nanoindentation depth in Li metal that exhibits pile-up can be underestimated by 11%.[72] The underestimation of contact depth will result in an overestimated modulus and hardness. The contact depth of 2 μm indentations on pure Li and Li/Na composite were calculated from the impression images on pure Li and 2.5 at.% Na samples, respectively. The h_c/h ratios of 1.11 ± 0.07 (N = 10) for Li and 1.09 ± 0.05 (N = 7) for Li/Na composite were then used to correct the depth when calculating the modulus and hardness. In order to image the impression area, samples need to be taken out of SEM chamber and tilted by 90°. It is difficult to get impression images of Na metal and samples with high Na concentration, because Na is so reactive that it reacts with air during this short process (Figure 3.10). Therefore, we assumed h_c/h = 1.06 for Na according to Fincher's work.[74]

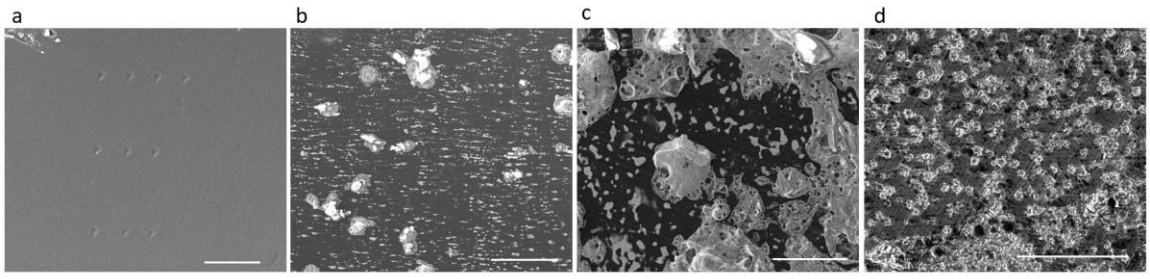

Figure 3.10 SEM images of a) pure Li, b) 2.5 at.% Na, c) 20 at.% Na, and d) pure Na samples after being taken out of SEM chamber for a short period. Scale bar = 100 μm.

As shown in Figure 3.11a and b, moduli and hardnesses of the samples with different Na concentrations saturated at contact depth of around 1 μm. The relatively larger moduli and hardnesses in low depth region can be attributed to the size effect of nanoindentation.[19,69,72,74] To compare the mechanical properties between different samples, the average values were collected at 1.8-1.9 μm depth, with 9-10 tests on each sample. In Figure 3.11c, the result shows a reduction in modulus when Na filler is introduced into Li matrix. The dot line represents the estimated modulus if we assume having Na fibers in Li matrix perpendicular to the load direction and calculate based on the equation:

$$\frac{1}{E} = \frac{v_{Na}}{E_{Na}} + \frac{v_{Li}}{E_{Li}} \tag{11}$$

Here v_{Na} and v_{Li} are the volume fraction of Na and Li phases. E_{Na} = 2.1 ± 0.3 GPa and E_{Li} = 5.0 ± 0.5 GPa are the elastic modulus measured from the pure Li and Na samples. And our experimental results of the composite films: $E_{Li/Na2.5}$ = 4.2 ± 0.2 GPa, $E_{Li/Na20}$ = 2.9 ± 0.2 GPa agree with the estimated value. The hardness shows no obvious change, with all of the samples exhibiting hardnesses in the range of 9.5-11.8 MPa. We also noticed a relatively high hardness of Na at low depth, which can be attributed to the size effect and possible influences from a different h_c/h at low depth.

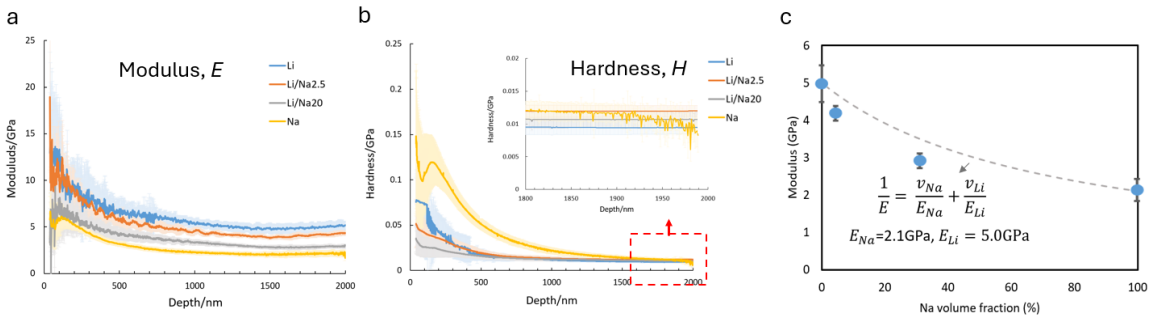

Figure 3.11 Modulus and hardness of Li/Na films. a) Modulus and b) hardness changing with indent depth for pure Li, 2.5 at.% Na, 20 at.% Na, and pure Na films. c) Moduli as function of Na volume fraction.

To determine the hardness of the individual Li and Na phases in the composite anode, we performed in situ nanoindentation into site-specific individual Na and Li regions within the 20 at.% Na composite material. This experiment also helps us determine the h_c/h value for Na phase in the composite at low depth. Nanoindentation was performed with a Berkovich indenter tip to a depth of 500 nm. Two representative load vs. displacement data sets and a corresponding SEM image, which shows a 85˚-tilted view of the indenter tip hovering 6 μm above the sample surface acquired during the nanoindentation experiment are shown in Figure 3.12a and b. Figure 3.12c and d contains top-down SEM images that show the residual indentation impressions outlined by dashed circles on the Na and Li phases, respectively. Hardness (H) is then calculated as

$$H = \frac{P}{A_c} \tag{12}$$

where P is the final indentation load measured by the instrument and A_c is the contact area measured directly from the SEM image to avoid influence of the pile-up effect. Table 2 contains the contact area (A_c), maximum indentation load (P), and hardness (H), as well as the h_c/h measured from the impression images with 500 nm indent depth. The result reveals that Na shows stronger pile-up effect at low depth, leading to 40% higher h_c/h at 500 nm depth compared with 2 μm, while the Li shows similar h_c/h under both 500 nm and 2 μm depth. This phenomenon can cause an overestimated hardness of Na at low depth if using the same h_c/h ratio as measured at 2 μm and help us to explain the high measured hardness of Na below 1 μm depth in Figure 3.11. We also need to note that the Na phase is embedded in a Li matrix, and this different boundary condition from pure Na film may slightly influence the h_c/h ratio. The shallow (500 nm) indentation experiments into individual Li and Na phases demonstrate that Na phase shows a hardness of around 8.9 MPa, which is 54% lower than the Li phase in the composite anode with a hardness of around 16.5 MPa.

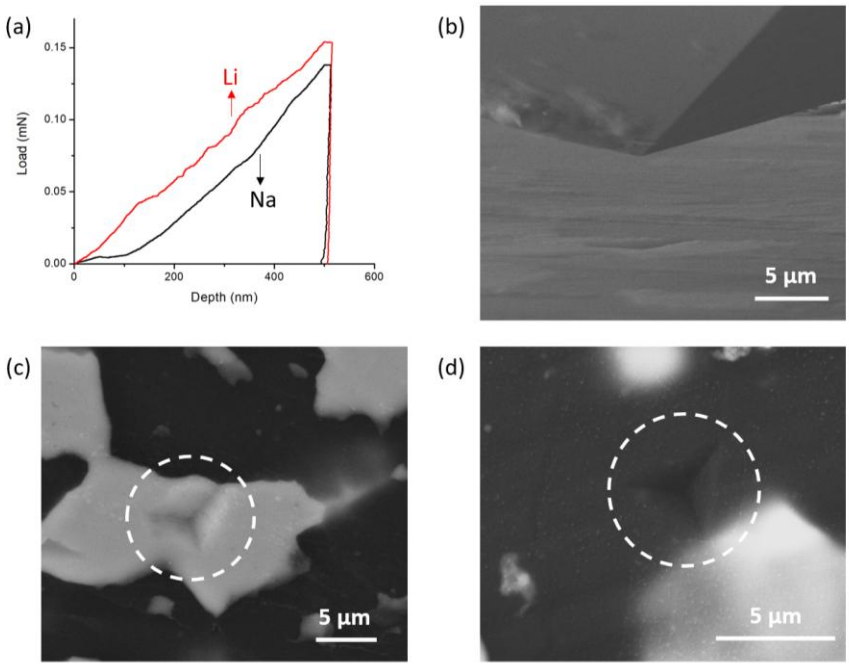

Figure 3.12. Nanoindentation tests on individual Li and Na phases. a) Load-depth data from nanoindentation tests on Li and Na regions from a 20% Na foil. b) SEM image during the nanoindentation experiment on the Na phase. 85˚-tilted view of the Berkovich tip hovering 6 µm above the sample surface with residual nanoindentation impression on Na region. Top-view SEM images of residual nanoindentation impressions on c) a Na region and d) a Li region.

Table 3.1. Experimental parameters (A_c and P) and measured hardness (H) of Li and Na phases shown in Figure 3.12.

	Contact area (A_c) [µm^2]	Indentation load (P) [mN]	Hardness (H) [MPa]	h_c/h
Li	9.89	0.158	16	1.08
	9.08	0.154	17	1.04
Na	16.77	0.138	8.2	1.45
	19.32	0.134	9.6	1.57

The yield strength of bulk Na metal was reported in the range of 0.16-0.28 MPa[74,75], and Na is generally considered mechanically softer than Li. However, the mechanical behavior of

Na at micro- and nanoscales remains insufficiently understood. In 2020, Fincher et al. showed a decreasing hardness of Na from ~30 MPa to 4 MPa as the indentation depth increased from 0.3 to 10 μm, with a further decrease to 1.1 MPa under 135 μm indentation depth.[74] However, change in h_c/h ratio with indent depth is not considered in their nanoindentation analysis. Compared with Li metal tested under equivalent conditions, Na metal displays softer mechanical properties, although the difference between two metals decreases with smaller length scale. Later, Liu et al. used an ETEM-AFM platform for in-situ mechanical property measurements of electroplated Na dendrites, showing yield strengths of 92-203 MPa from nanorods or nanoparticles with diameters of 196-1110 nm.[76] Similar method has been applied to Li whisker and the yield strengths from 12.2 MPa to 244 MPa were measured with diameter from 76 to 607 nm.[77] But both works indicate a nanolayer of Na_2CO_3 or Li_2CO_3 with less than 20 nm thickness on the sample surface, which may slightly influence the test results. In addition, Citrin et al. reported an average yield stress of 16.0 ± 6.82 MPa from electrodeposited Li pillar in SEM with 360-759 nm diameters.[78] These results suggest that while lithium generally exhibits higher intrinsic strength, the mechanical contrast between Na and Li becomes increasingly condition-dependent at the submicron scale as shown in figure 3.13. Our nanoindentation measurements at a depth of 500 nm on individual Li and Na phases further show that the Na phase exhibits a 54% lower hardness compared with the Li phase in the Li/Na composite anode. This observation supports our hypothesis that the Na phase can more easily deform without high stack pressures, thereby mitigating void formation and improving interface contact between the metal anode and solid-state electrode.

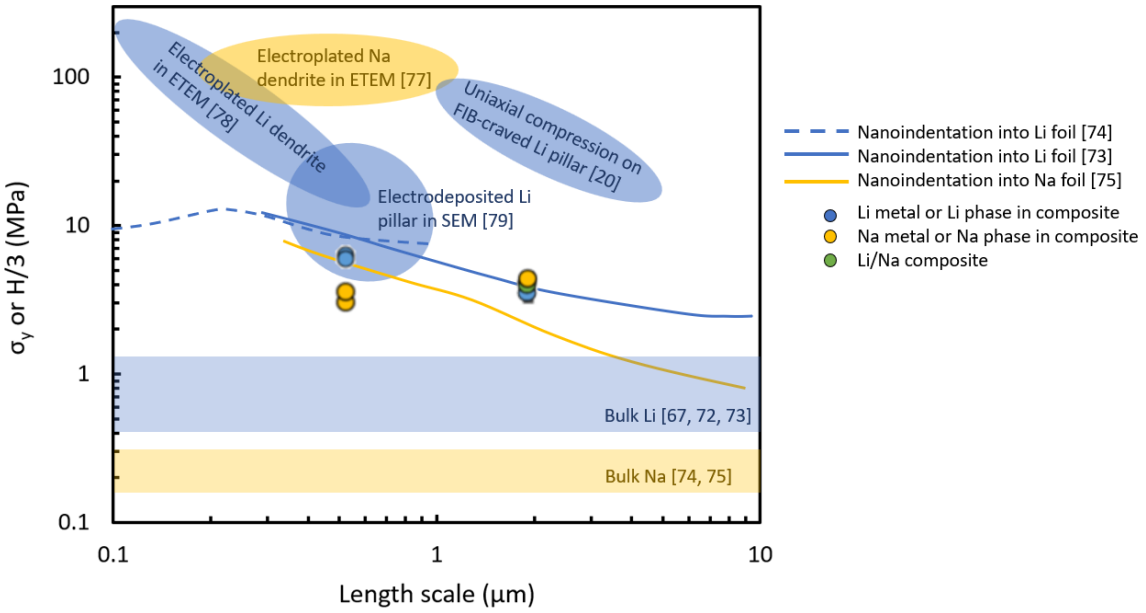

Figure 3.13 Summary of reported yield strength and hardness of Li and Na metals from literature, together with the nanoindentation results from this work.

3.4 Summary

The mechanical behavior of Li/rGO and Li/Na composite anodes was studied by uniaxial compression experiments on FIB-milled micro-pillars and nanoindentation experiments, respectively. The in-situ micro-pillar compression test allows us to observe the deformation process and identify the deformation mechanism. In pure Li micro-pillars, the initial displacement burst corresponds to a shear via crystallographic slip, showing a flow stress of 43 MPa. Through SEM images and EDS analysis, we found that the rGO is concomitant with adjacent pore structures. During compression, multiple cracks occur in the hollow regions, resulting in lower modulus and yield strength in high C loading samples. Nanoindentation was conducted on Li/Na composite anodes. A pile-up effect was observed and corrected according to the indentation impression area. The indentation with a depth of 2 μm into the composite revealed a modulus reduction caused by the introduction of Na filler into Li matrix. Size effect was observed in pure Li and Na metals, as well as in the composite

anodes, and all samples exhibited similar hardness in the range of 9.5-11.8 MPa. Shallow (500 nm) indentation into individual Li and Na phases of the composite anode was then carried out, indicating that the Na phase shows more severe pile-up effect with low indentation depth and has 54% lower hardness compared with the Li phase. This result supports our hypothesis that during the Li stripping process, Na can easily deform without high stack pressures. Therefore, the Na phase can lead to reduced void formation and improved interface contact between the metal anode and solid-state electrolyte.

Chapter 4

HYDROGEL INFUSION ADDITIVE MANUFACTURING FOR MICRO-ARCHITECTED LFP/C ELECTRODES

4.1 Overview

Additive manufacturing techniques have been increasingly explored as a promising approach to fabricate 3D electrodes with controlled geometries. However, challenges remain in achieving high printing resolution and precise control over complex micro-architectures, especially for cathodes, which usually require the introduction of active material particles or precursors into the print ink or resin. Our group previously developed the HIAM technique for printing metallic and metal oxide materials, and this method has been successfully applied to fabricate 3D LCO electrodes. Its potential to synthesize other classes of materials, such as transition metal phosphates and composite materials, remains to be explored.

This chapter develops a HIAM-based method to fabricate micro-architected LFP/C composite electrodes via ion infusion into a pre-printed polymer scaffold, followed by thermal treatment. During calcination, the polymer scaffold served as a carbon source, enabling the concomitant formation of a conductive carbon network while simultaneously reducing the Fe^{3+} to Fe^{2+}. Powder XRD analysis confirmed the formation of olivine-structured LFP, while SEM and EDS characterization revealed uniformly distributed LFP particles within the lattice beams. The carbon content of the electrodes was tuned through precursor concentration, which significantly enhanced the mechanical strength. Electrochemical measurements of the micro-architected LFP/C electrode assembled in coin cells exhibited clear LFP redox peaks near 3.4 V and delivered a specific capacity of 160 mAh/g at C/10, close to the theoretical capacity of LFP. These results demonstrate that this HIAM-based approach enables the fabrication of mechanically robust micro-architected LFP/C electrodes with high resolution and well-controlled 3D architectures.

4.2 Fabrication of 3D-architected LFP/C electrode

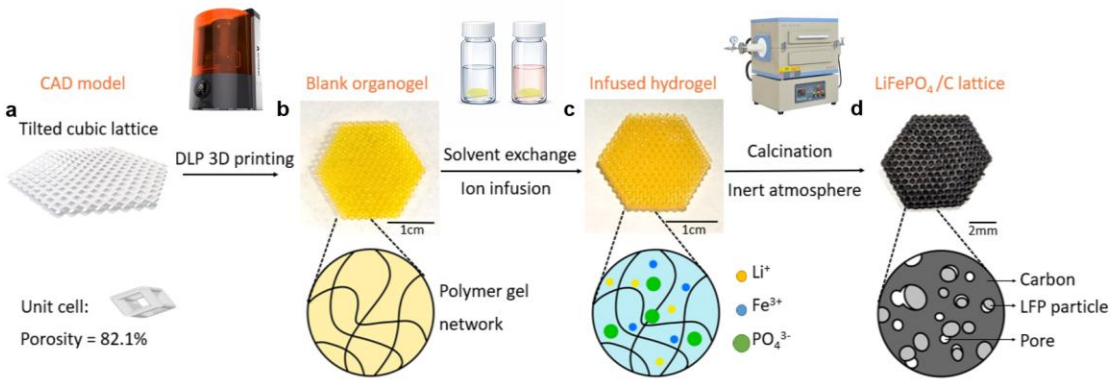

Figure 4.1. Schematics of the hydrogel infusion additive manufacturing process for LFP/C composite electrodes and representative images of the resulting lattices. a) CAD model of a tilted cubic lattice and its unit cell. b) A 3D printed blank organogel lattice. c) Metal-ion-infused hydrogel lattice formed via solvent exchange and ion infusion. d) LFP/C composite electrode obtained after pyrolysis and calcination under inert atmosphere.

Figure 4.1 contains the specific steps of the gel infusion additive manufacturing process, which begins with a computer-aided design (CAD) architecture model; in this case, a two-layer tilted cube. The blank organogel scaffold is then printed using a DLP 3D printer (Ember, Autodesk) and serves as a template defining the 3D architecture of the final electrode. The photoresin is prepared by mixing 0.1 mol poly(ethylene glycol) diacrylate (PEGda; Mn = 575, Sigma-Aldrich) with N,N-dimethylformamide (DMF; 99.8%, Sigma-Aldrich) solvent under 1:1 volume ratio. 1.33 mmol 2-dimethylamino-2-(4-methyl-benzyl)-1-(4-morpholin-4-yl-phenyl)-butan-1-one (Omnirad 379; iGM Resins), 1.25 mmol 4,4'-bis(dimethylamino)benzophenone (Michler's ketone; 98%, Sigma-Aldrich), and 0.06 mmol 1-Phenylazo-2-naphthol (Sudan I; ⩾95%, Sigma-Aldrich) are added into the resin to serve as photoinitiator, photosensitizer, and UV blocker, sequentially. The exposure time is 7-10 s and varies slightly depending on the age of the photoresin.

The printed organogel scaffold was then swollen in deionized (DI) water for 2 hours at 80 ˚C for solvent exchange and in aqueous solution of $LiNO_3$, $Fe(NO_3)_3$, and $NH_4H_2PO_4$ for 2 days at 80 ˚C for ion infusion. An optical image of the infused gel is shown in Figure 4.2a. Solvent exchange replaces the organic solvent with DI water and forms a hydrogel scaffold. The ion infusion step enables the diffusion of Li^+, Fe^{3+}, and PO_4^{3-} ions into the scaffold and their embedding within the polymer network. Subsequently, calcination in Ar atmosphere (gas flow rate = 50 ml/min) is carried in a tube furnace (OLT-1500X-UL, MTI). The temperature was firstly increased to 400˚C for 4 hours pyrolysis, followed by heating to 800˚C for 6 hours calcination. The temperature profile is shown in Figure 4.3. The SEM image of the as-synthesized LFP/C lattice is shown in Figure 4.2b. During calcination, the polymer scaffold acts as carbon source, driving the reduction of Fe^{3+} to Fe^{2+} and forming an additional conductive carbon network within the lattice. The expected reaction is: $Fe(NO_3)_3 + LiNO_3 + NH_4H_2PO_4 + \eta C_{26}H_{46}O_{13} \rightarrow LiFePO_4 + 26\eta C + 4NO_2 \uparrow + (13\eta + 4)H_2O \uparrow + (10\eta - 2.5)H_2 \uparrow + NH_3 \uparrow$. η is the molar ratio of PEGda to $Fe(NO_3)_3$ salt.

This process results in an approximately 60% linear shrinkage after calcination. For the tilted cubic lattice, the measured linear shrinkage is 61% in the surface plane (x-y plane), and 63% in the thickness direction (z direction). Specifically, the hexagon diagonal in the x-y plane shrinks from $15\sqrt{2}$ mm in the CAD model to 8.33 mm after calcination, while the lattice thickness decreases from $\sqrt{3}$ mm in CAD model to 0.646 mm after calcination.

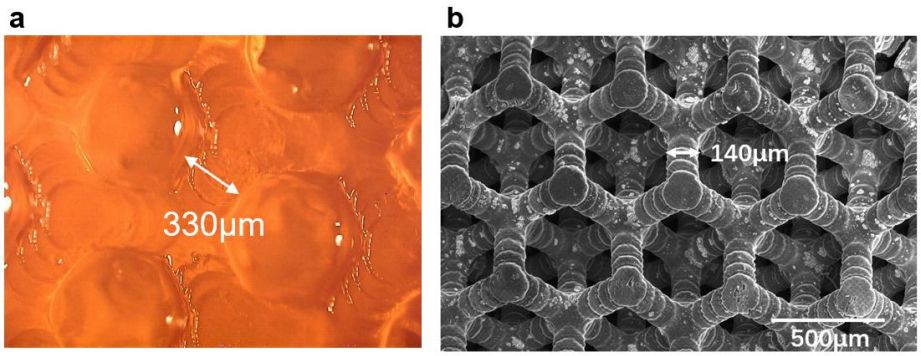

Figure 4.2 Images of a two-layer tilted cube lattice. a) Optical image of the infused hydrogel. b) SEM image of the LFP/C composite lattice.

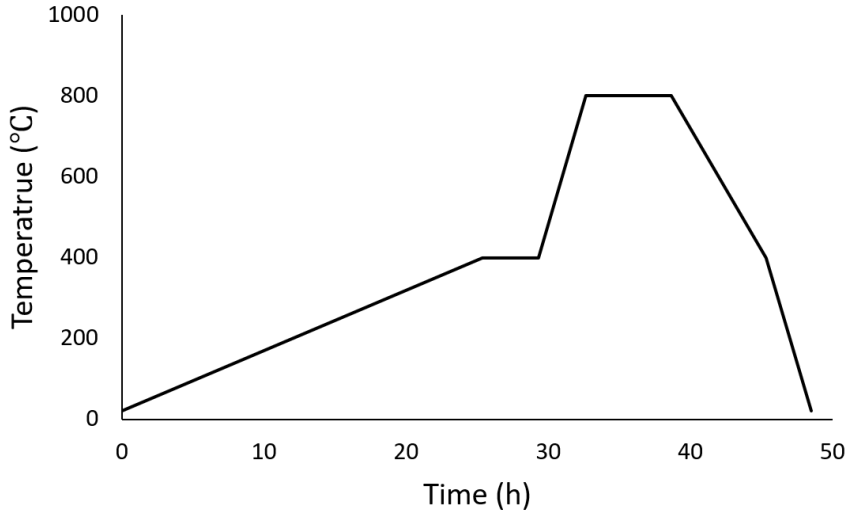

Figure 4.3 Temperature profile of pyrolysis and calcination process.

4.3 Thermal analysis for calcination process

Figure 4.4a presents the thermogravimetric analysis (TGA; TGA 550, TA Instruments) of the infused hydrogel under a N_2 atmosphere, conducted at a heating ramp of 1 °C/min from room temperature to 800 °C. The plot shows that 10.6% of the original mass remains at the final calcination temperature of 800 °C. The blue curve shows the derivative of sample weight with respect to temperature (dW/dT) and demonstrates that the vaporization of water

within the polymer network occurs below 100 °C, accompanied by a mass loss of around 25%. The first mass loss peak is observed at 130 °C, corresponding to the loss of bound water from $Fe(NO_3)_3 \cdot xH_2O$ and $LiNO_3 \cdot xH_2O$. Similar dehydration peaks have been reported in Cu^{2+} and Ni^{+} infused hydrogels[48]. Three major mass loss events occur between 290 °C and 420 °C (shaded blue region), which correspond to three concurrent reactions occurring in this temperature range: (1) decomposition of the reactants, (2) pyrolysis of the polymer network, and (3) reduction of iron from Fe (III) to Fe (II). For comparison, an analogously produced TGA curve of a blank hydrogel, with no metal ions, is shown in Figure 4.4b, exhibiting a single pyrolysis dW/dT peak at 350 °C.

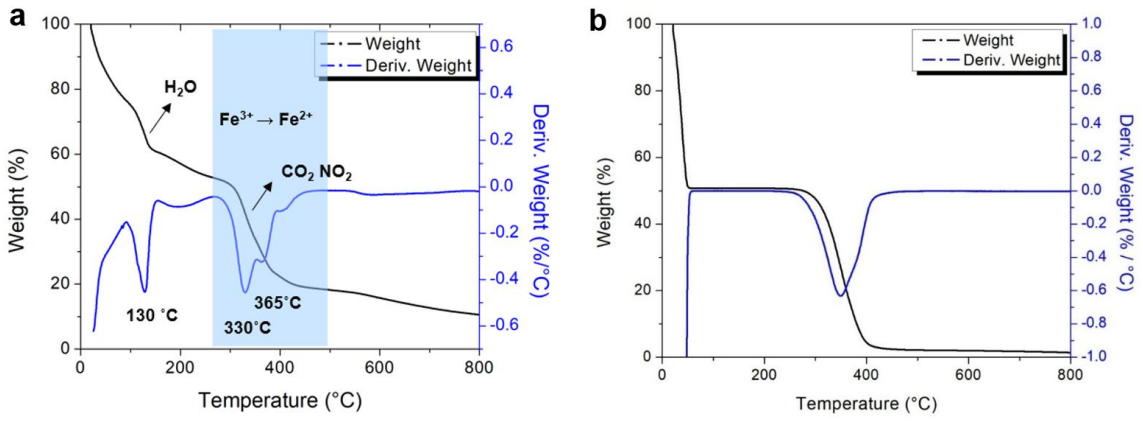

Figure 4.4 TGA profile of the a) ion-infused hydrogel and b) blank gel under N_2 atmosphere, with a heating ramp from room temperature to 800 °C at 1 °C/min.

4.4 Chemical composition and structure characterization

The lattices were ground for powder X-ray diffraction analysis (XRD; SmartLab, Rigaku) with Cu Kα radiation at 40 kV and 50 mA. Figure 4.5 contains the powder XRD analysis that shows the formation of well-crystallized LFP with olivine structure. The XRD results reveal LFP as the main phase, along with two impurity phases: Fe and Li_3PO_4, in the solid sample prepared from the liquid precursor solution with the molar ratio of 1 (Li^{+}) : 1 (Fe^{3+}) : 1 (PO_4^{3-}). The formation of Li_3PO_4 and metallic Fe is attributed to the excessive Li^{+}

concentration in the infused hydrogel, which causes Li^+ ions to bind with the PO^{4-} ions and reduce the Fe^{3+} ions to metallic state in the high-temperature reducing atmosphere during calcination. The mass fractions of the crystalline phases are calculated through XRD refinement (Figure 4.6, Table 4.1) and show that the stoichiometric precursor solution produces solids with the atomic ratio of 1.2 (Li) : 1.0 (Fe) : 1.0 (P) (Table 4.2). To suppress the formation of impurity phases, we reduced the initial Li^+ concentration in the precursor solution from 1 mol/L to 0.9 mol/L (Sample II), 0.7 mol/L (Sample III), and 0.5 mol/L (Sample IV), while the $Fe(NO_3)_3$ and $NH_4H_2PO_4$ salt concentrations were kept as 1 mol/L. The XRD data reveals a corresponding steady decrease in the Li_3PO_4 and Fe peak intensities in the solid samples, with Sample III containing only the pure LFP phase (Figure 4.5). We found that in the 0.5 mol/L Li^+ sample, the shortage of Li to bind with PO_4^{3-} leads to the formation of another undesirable phase, Fe_2P. We chose the solid sample that consists of 93.4 wt.% $LiFePO_4$, 5.5 wt.% Li_3PO_4, and 1.1 wt.% Fe (Sample II) for the following electrochemical experiments in this work.

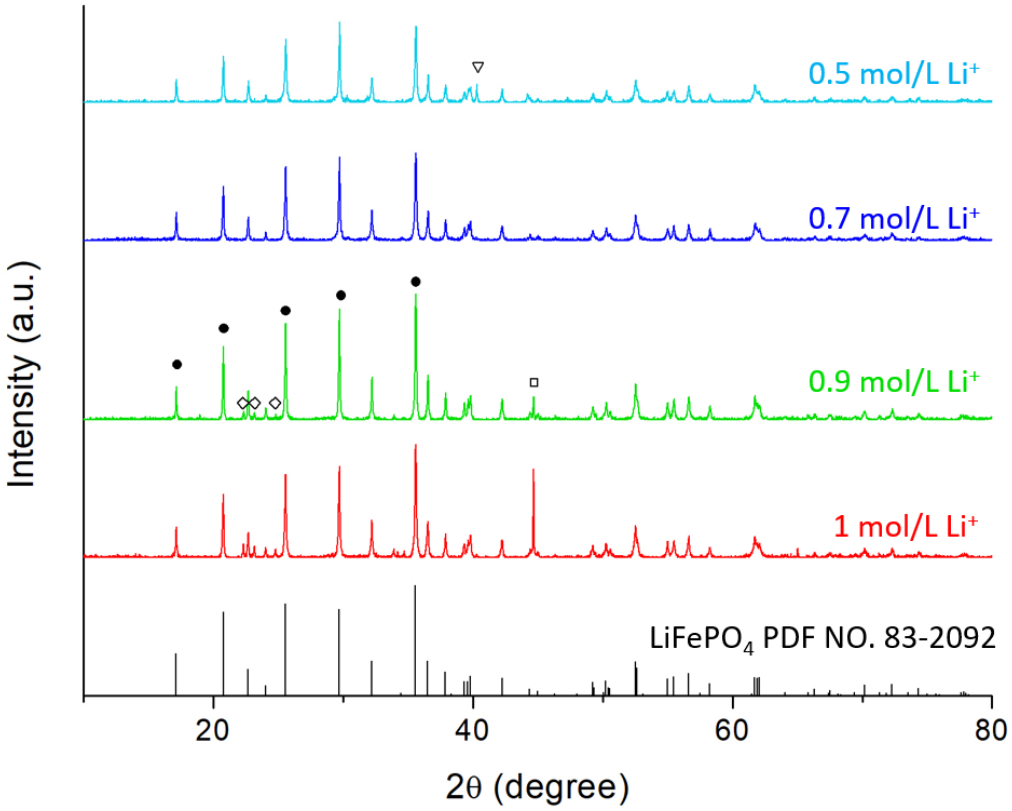

Figure 4.5 XRD pattern of samples prepared using a stoichiometric precursor solution, 1 mol/L Li^+ (Sample I), and solutions with 0.9, 0.7, and 0.5 mol/L Li^+ concentrations (Sample II, III, IV), while the Fe^{3+} and PO_4^{3-} concentrations are kept at 1 mol/L. The characteristic peaks are labeled as: ● LiFePO4, ▽ Fe2P, ◇Li3PO4, and □ Fe.

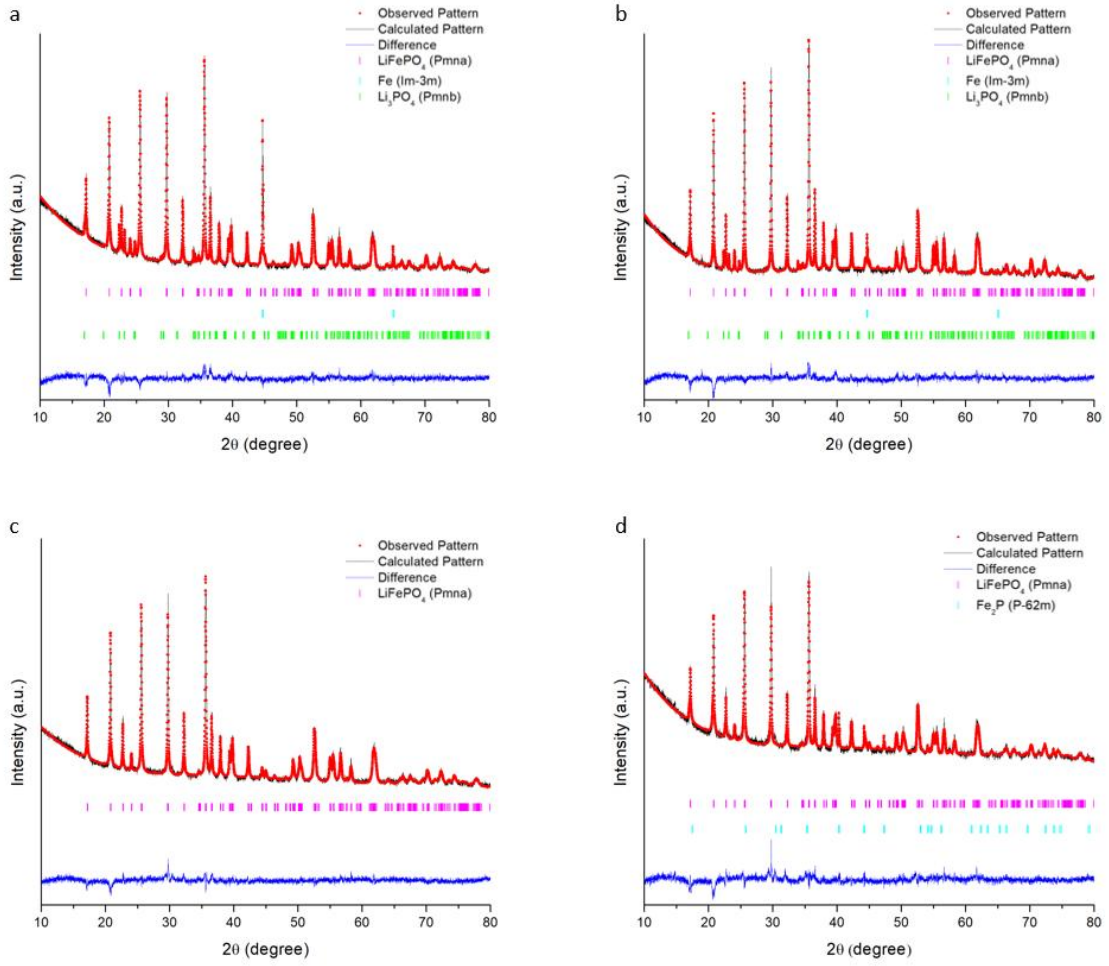

Figure 4.6 Refinement profile of the XRD data for samples prepared using a a) stoichiometric precursor solution, 1 mol/L Li^+, and solutions with b) 0.9 mol/L, c) 0.7 mol/L, and d) 0.5 mol/L Li^+ concentrations, while the Fe^{3+} and PO_4^{3-} concentrations are kept at 1 mol/L.

Table 4.1 Weight fractions of crystalline phases and reliability factors (χ^2) of the XRD refinement results for sample prepared by precursor solutions with various Li^+ concentrations. The concentration of Fe^{3+} and PO_4^{3-} were kept as 1mol/L.

	$c(Li^+)$ (mol/L)	$LiFePO_4$ (wt.%)	Fe_2P (wt.%)	Li_3PO_4 (wt.%)	Fe (wt.%)	χ^2
Sample I	1	87.2	-	8.8	4	1.97
Sample II	0.9	93.4	-	5.5	1.1	2.25
Sample III	0.7	100	-	-	-	1.57
Sample IV	0.5	97.1	2.9	-	-	2.29

Table 4.2 Atomic ratio between Li, Fe, and P calculated based on XRD refinement results.

	$c(Li^+)$ (mol/L)	Li	Fe	P
Sample I	1	1.23	1.01	1
Sample II	0.9	1.07	1.04	1
Sample III	0.7	1	1	1
Sample IV	0.5	0.97	1.03	1

The beam cross section was prepared via FIB with an accelerating voltage of 30 kV. Ion beam currents of 50 nA, 10 nA, and 5 nA were applied sequentially. An SEM image of the FIB-milled beam cross-section is shown in Figure 4.7f. The beam width is measured to be 139 μm, corresponding to a shrinkage of approximately 65% from the original CAD model (400 μm). The thickness of the beam measured from the cross-section SEM image is 51 μm, representing the minimum feature size of this structure. Figure 4.7g-j contains EDS maps of the same beam cross-section, which demonstrate a uniform distribution of each present element: C, P, O, and Fe. For comparison, a cross-section image of sample I prepared by the precursor solution with the molar ratio of 1 (Li^+) : 1 (Fe^{3+}) : 1 (PO_4^{3-}), together with its EDS maps, is also included in Figure 4.7a-e. The non-uniform distribution of P and Fe elements

indicates the formation of Li_3PO_4 and Fe phases as individual particles inside the beam. These results, together with the zoomed-in SEM images in Figure 4.8a and b, indicate that the 201 ± 67 nm-sized LFP particles are homogeneously distributed throughout the carbon network within the beams (N = 114). The LFP particle size distribution is shown in Figure 4.8c. Submicron pores are also observed in the beam cross-section, accounting for around 13% of the area.

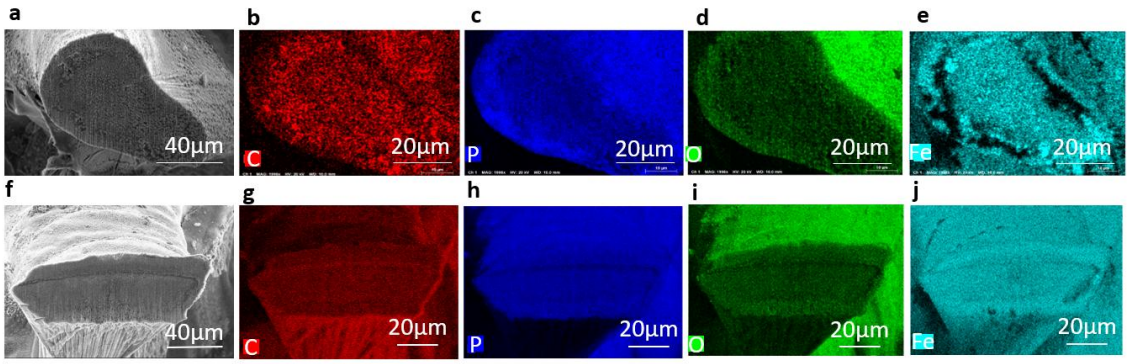

Figure 4.7 SEM images of FIB-milled cross-section of lattice beams and the corresponding EDS maps. a) SEM image of beam cross-section of Sample I prepared with 1 mol/L Li^+ precursor solution and b-e) the corresponding EDS element maps. f) SEM image of beam cross-section of Sample II prepared with 0.9 mol/L Li^+ precursor solution and g-h) the corresponding EDS element maps, showing the homogeneous distribution of C (red), P (blue), O (green), and Fe (turquoise).

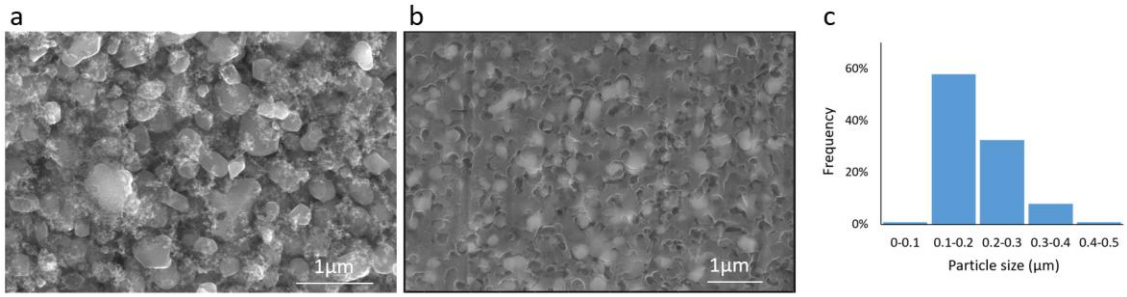

Figure 4.8 Zoomed-in SEM images showing the presence and dimensions of LFP particles, carbon network, and pore structure a) on beam surface and b) inside the lattice beam. c) Frequency distribution of LFP particle size. 114 particles were measured.

4.5 Mechanical strength enhancement via carbon network

Our results indicate that tuning the ion concentrations in the precursor solutions offers control over the carbon content in the solid electrodes. While the ratio of Li^{+} : $Fe3^{+}$: PO_4^{3-} was kept as 0.9:1:1, the concentration of Fe^{3+} and PO_4^{3-} were decreased to 0.9, 0.7, 0.5, and 0.25 mol/L (Figure 4.9a) to investigate the effect of precursor concentration on the carbon content of the finial electrodes. Figure 4.9b shows that the volume of samples after swelling in solution decreased with increasing concentration. The volume of the 0.25 mol/L samples was close to the control group of samples swollen in DI water (left column with a darker color). The total masses of four samples from each group and the changes during the fabrication process are recorded in Table 4.3. After swelling in DI water, the sample mass decreased by 5.6%, mainly resulting from solvent exchange. The mass of the 0.25 mol/L sample increased by 9.4%, which can be explained by the infusion of ions. Above 0.25 mol/L, the gels with a higher precursor concentration tended to lose more mass after infusion, despite their expected higher ion loading, indicating that the acidic environment and the presence of nitric acid can cause corrosion of the gel. Compared to the infused gel, the sample prepared with a higher precursor concentration retained a higher percentage of mass after calcination, corresponding to a higher LFP loading.

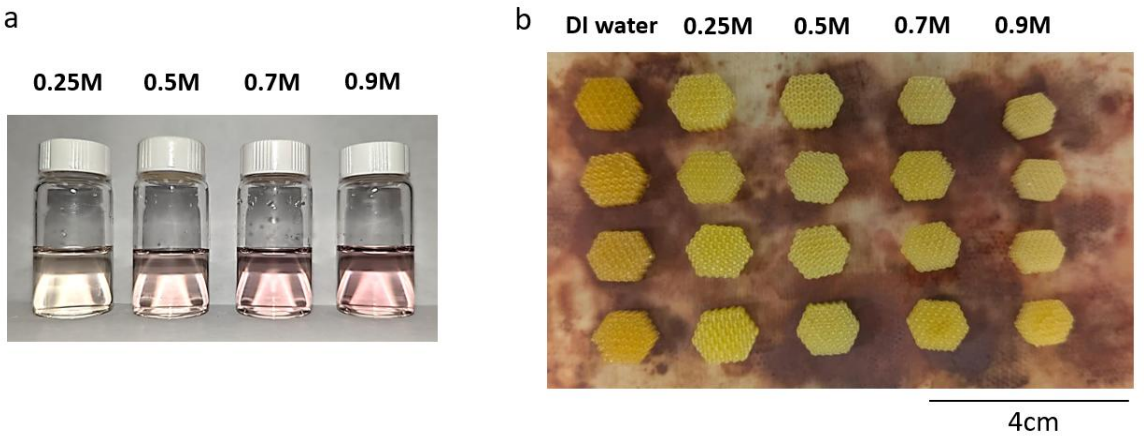

Figure 4.9 Ion concentration variation in precursor solutions. a) Image of precursor solutions with concentration of Fe^{3+} and PO_4^{3-} decreased to 0.9, 0.7, 0.5, and 0.25 mol/L b) Infused hydrogels prepared by precursor solutions with varied concentrations.

Table 4.3 Masses of samples prepared by precursor solutions with varied concentrations and changes in mass during the fabrication process.

Precursor concentration (mol/L)	Mass before infusion (mg)	Mass after infusion (mg)	Mass after calcination (mg)	Mass change during infusion	Mass remaining after calcination
0.9	862.1	555.4	31.3	-35.6%	5.6%
0.7	906.1	752.1	39.9	-17.0%	5.3%
0.5	886.3	867.7	39.1	-2.1%	4.5%
0.25	932.6	1020.5	33.1	9.4%	3.2%
0	858.2	810.5	13.6	-5.6%	1.7%

We measured the carbon content in samples prepared with different precursor concentrations via TGA analysis by heating them in air to 900˚C at a 1˚C/min rate (Figure 4.10a). A 5.1%

mass increase was attributed to the oxidation of LFP into $Li_3Fe_2(PO_4)_3$ and Fe_2O_3, and all additional mass loss was assigned to the gasification of carbon[79]. The plot in Figure 4.10b shows that the final carbon content decreased from 32.5% to 7.4% as precursor concentration increased from 0.25 mol/L to 0.9 mol/L, which can be attributed to the corrosion of gel and the increased LFP load.

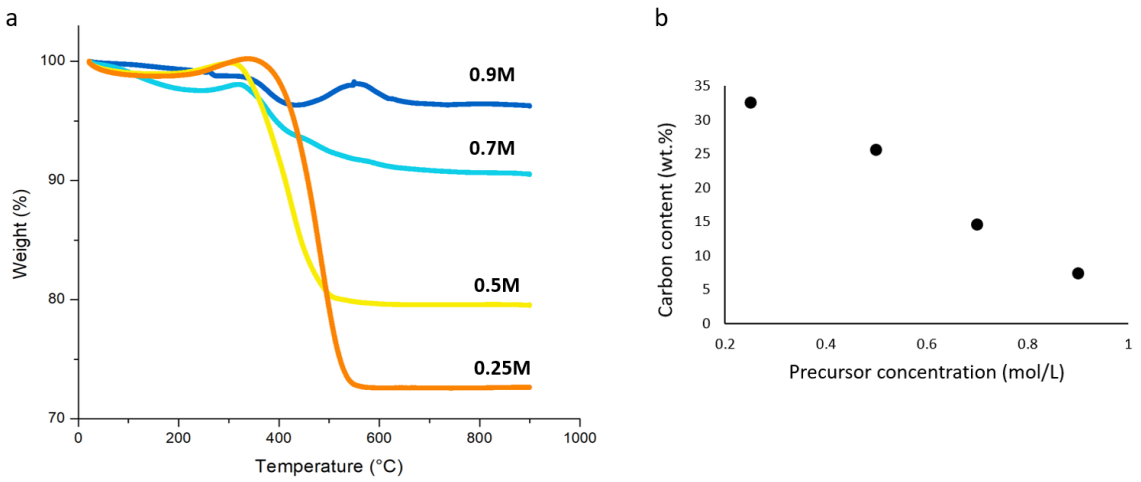

Figure 4.10 Effect of precursor concentration on the carbon content. a) TGA profile of LFP/C electrodes prepared by precursor solutions with various concentrations. A heat ramp to 900 ˚C at 1˚C/min is applied in air. b) The final carbon contents of the 3D electrodes as a function of the precursor concentration.

We investigated the mechanical behavior of the LFP/C four-layer tilted cubic lattices with varying carbon content by conducting uniaxial compression experiments at a strain rate of 10^{-3} s^{-1} until failure. Columns with 4-layer tilted cube structure (Figure 4.11a) were prepared for uniaxial compression experiments. A dynamic mechanical analyzer (DMA; DMA850, TA Instruments) with a 15 mm diameter compression clamp was used (Figure 4.11b). A layer of Crystalbond was added under the sample to align the sample top surface with the compression clamp. The videos were recorded with an inspection camera (TTAKMLY). The effective elastic modulus was calculated by the slope of the linear elastic region in the stress-

strain curve after the stress reached 0.015 MPa. Failure strength was defined as the stress before the first observed failure event, and the maximum stress during the compression test was recorded as the maximum strength.

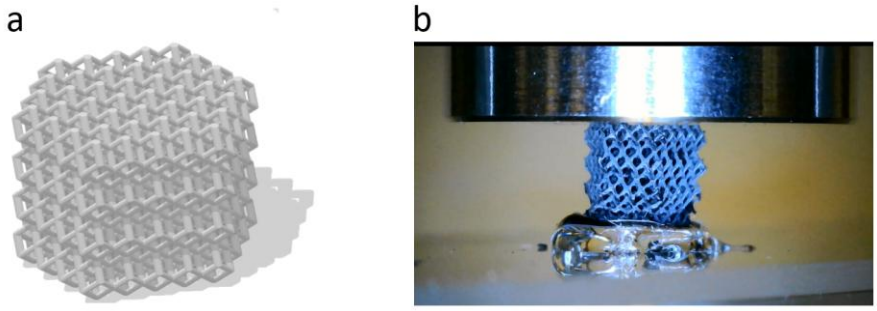

Figure 4.11 Experimental setup for uniaxial compression tests. a) CAD model of the 4-layer tilted cubic lattice for uniaxial compression test. The beams with 1mm length and tilted 35.3˚ from the horizontal were formed by sweeping circles with a diameter of 400 μm. The structure porosity is 82.1%, which is same as the tilted cubic electrodes. b) A 15 mm diameter compression clamp is used in uniaxial compression experiments.

Figure 4.12 shows several representative engineering stress-strain data sets, as well as the optical images of each lattice in the as-fabricated state and at a representative compressive strain between 4-6%. The data indicate that, after establishing full contact, the lattices first undergo linear elastic deformation up to a strain of 0.5%, after which most samples experienced a global collapse from a maximum stress of 47-162 kPa, depending on the C content, at strains between 1% and 4%. Engineering stress-strain data beyond 5% strain is shown in Figure 4.13, where the stress gradually increases as the compressive strain increases to 30%, likely as a result of densification. We observed that the samples with low carbon content (7.4% and 14.6%) failed at multiple points within the bottom lattice layers at strains of 1%-2%, resulting in broad and relatively smooth peaks in the stress-strain curve. Samples with higher carbon content (25.6% and 32.5%) exhibited multiple abrupt stress drops throughout deformation, which are attributed to layer-wide beam fracture followed by sliding along the fracture plane.

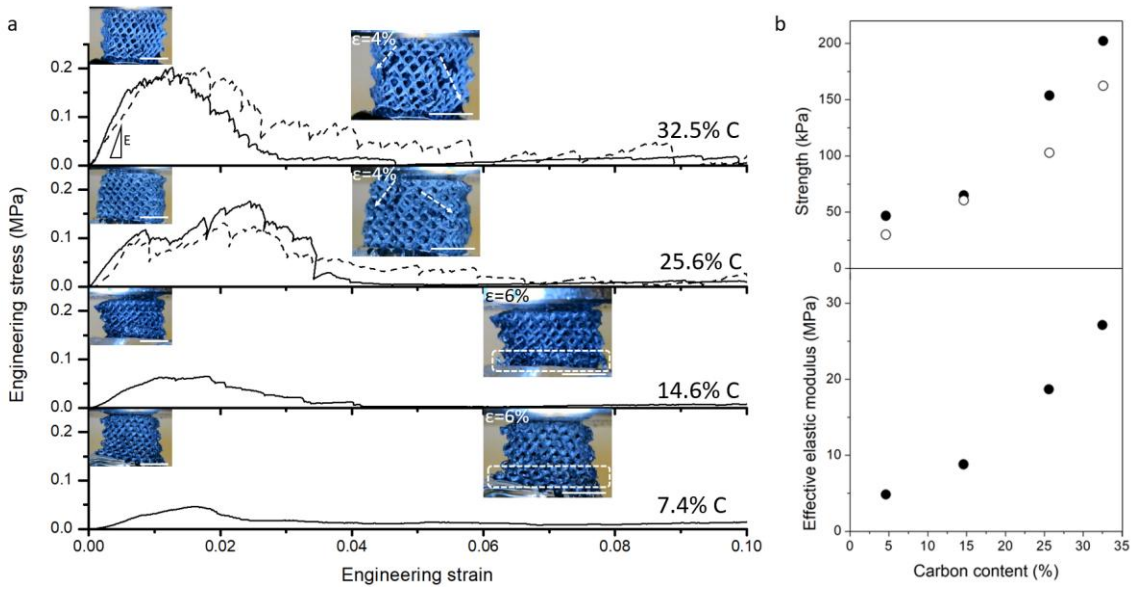

Figure 4.12. Mechanical characterization of the LFP/C composite lattices. a) Engineering stress-strain data obtained during uniaxial compression of the LFP/C lattices that contain 7.4%, 14.6%, 25.6%, and 32.5% carbon, conducted at a strain rate of 10^{-3} s^{-1}. The slope marker in the linear elastic loading section represents the effective Young's modulus of the lattice. Optical images of the same lattices before and after the major collapse are shown at corresponding strains. Scale bar = 2 mm. b) Effective Young's modulus, maximum strength (solid circles), and failure strength (open circles) as a function of carbon content in the micro-electrodes.

Figure 4.12b summarizes the strength and effective Young's modulus of the LFP/C micro lattices as a function of carbon content and reveals a non-linear increase in both. The 25.6% C and 32.5% C lattices are able to support stresses up to $\sigma_{failure}$ = 103 kPa and 162 kPa prior to the first interlayer collapse, with corresponding effective Young's moduli of E = 18.7 MPa and 27.1 MPa, respectively. The higher carbon content and the emergent interlayer collapse failure mechanism in these lattices contribute to their mechanical resilience. In contrast, the 7.4% C lattice (σ_{max} = 47 kPa, E = 4.8 MPa) and the 14.6% C lattice (σ_{max} = 65 kPa, E = 8.8 MPa) deform primarily through individual local fracture. These results indicate that the carbon network significantly enhances the mechanical strength of the LFP/C lattices and

preserves shape integrity of the 3D structure during cell assembly and function. We therefore selected the 25.6% C sample for electrochemical performance evaluation in this work, as it provides sufficient mechanical strength for cell assembly while retaining a higher LFP content than the 32.5% C sample.

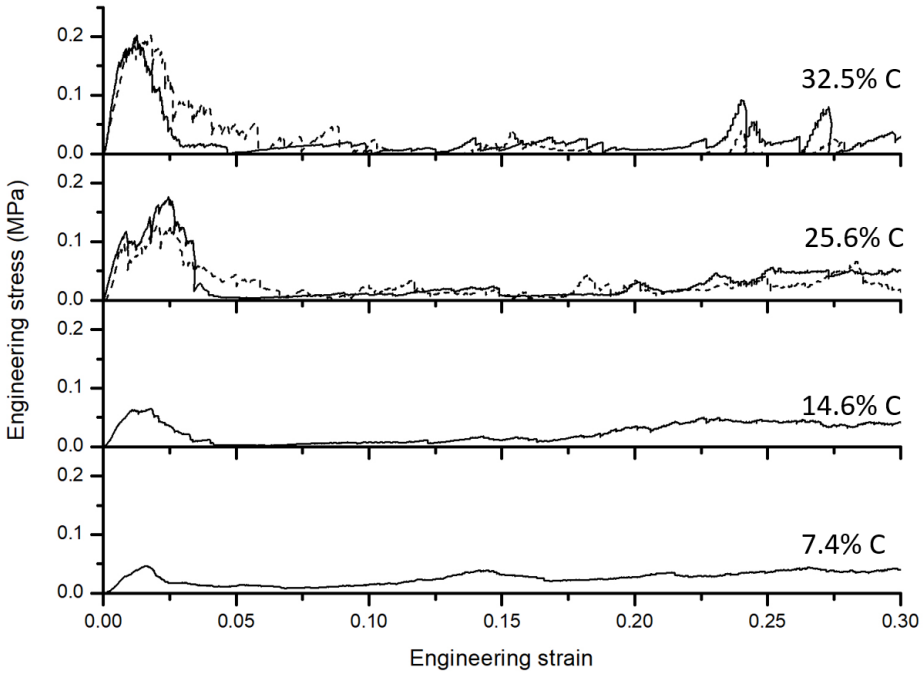

Figure 4.13 Engineering stress vs strain during uniaxial compression of the LFP/C lattices that contain 7.4%, 14.6%, 25.6%, and 32.5% carbon conducted at a strain rate of 10^{-3} s^{-1}.

4.6 Electrochemical performance of micro-architected LFP/C electrodes

To evaluate the electrochemical performance of the micro-architected LFP/C electrodes, micro-architected electrodes were assembled into CR2032 coin cells against Li foil (ribbon, thickness × W 0.38 mm × 23 mm, 99.9%, Sigma-Aldrich) for electrochemical testing (Figure 4.14a). The Al foil current collector and the 25 μm trilayer separator (Celgard 2325, Cambridge Energy Solutions) were punched out with a diameter of 15.9 mm. The electrode was adhered to the current collector via a conductive adhesive, which was made by mixing 43 wt.% carbon black (Timical Super C65, MTI) and 57 wt.% polyvinylidene fluoride

(PVDF; Sigma-Aldrich) in 1-methyl-2-pyrrolidinone (NMP; 99.5%, Sigma-Aldrich) at 56 mg/ml. A 1 mm thick polyacrylate ring printed from a commercial photoresin (PR48, Autodesk) was placed around the electrode to protect the structure. All of the components, together with the CR2032 coin cell cases (MTI), were dried at 50 ˚C under vacuum overnight before transferring to an Ar glovebox for cell assembly. 1M $LiPF_6$ in ethylene carbonate (EC) and diethyl carbonate (DEC) with 1:1 volume ratio was used as electrolyte.

Cyclic voltammetry (CV) between 2.4 V and 4.2 V was performed on the electrode with tilted cube structure using a potentiostat (SP-200, BioLogic). The scanning rate was set to be 0.025 mV/s. Figure 14b shows a pair of redox peaks centered at approximately 3.4 V, which is consistent with the characteristic redox potential of LFP vs. Li/Li^+ at around 3.5 V[80], confirming the electrochemical activity of the electrodes.

Galvanostatic cycling tests were conducted on electrodes with 3D structures using a battery cycling system (BTS4000, Neware). The batteries were charged with constant current until the voltage reached 4.2 V, then discharged until the voltage dropped to 2.2 V. After 3 formation cycles, the coin cells were cycled at C/10, C/5, C/2, 1C, and 2C for 3 cycles each, followed by 10 cycles at C/10. A 1C rate stands for fully charging or discharging the electrode in 1 hour, assuming a specific capacity of 170 mAh/g for LFP. Figure 4.15a contains the galvanostatic charge-discharge profiles of the 25.6% C sample measured under various C-rates and reveals a specific capacity of 160 mAh/g at C/10, which is only ~7% below the theoretical capacity of LFP (170 mAh/g).

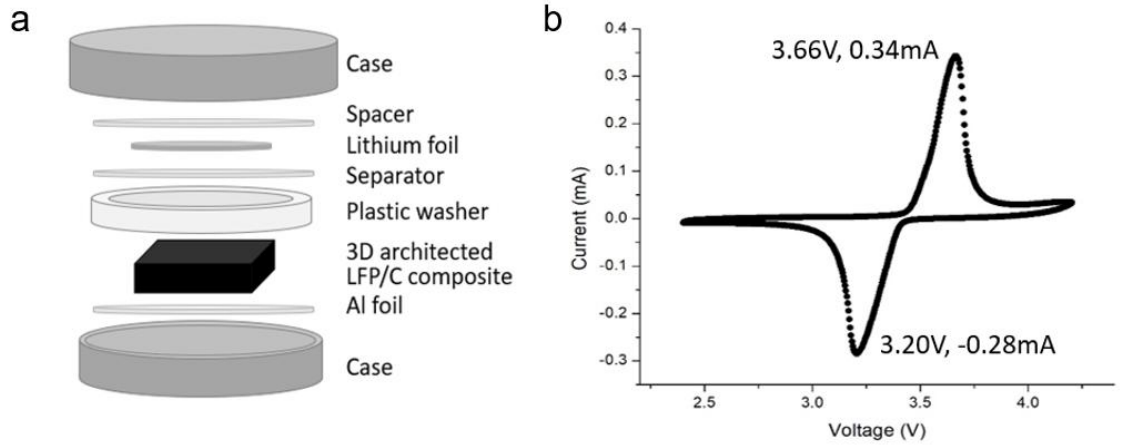

Figure 4.14 Cyclic voltammetry of a coin cell with LFP/C electrode. a) Schematic diagram of a coin cell with the micro-architected electrode for electrochemical test. b) Cyclic voltammetry measurements of the tilted cube electrode at a scan rate of 0.025 mV/s.

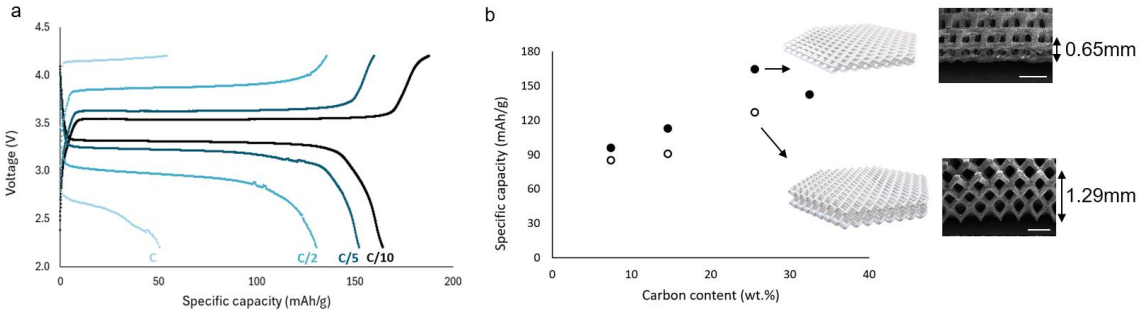

Figure 4.15 Galvanostatic charge-discharge measurement. a) Galvanostatic charge-discharge profiles of the tilted cube electrode at C/10, C/5, C/2, and 1C. b) Discharge capacities at C/10 of samples with various carbon contents. scale bar = 500 μm

The discharge capacities under C/10 of samples with different carbon contents are shown in Figure 4.15b. Samples with a 2-layer tilted cube structure (full z) and the same structure squeezed to 50% in thickness (half z) were used. The results show an improved specific capacity with increasing carbon content until a capacity of 160 mAh/g is reached at 25.6% C in the half-z sample. Mechanical failure may occur in samples with lower carbon content (7.4% and 14.6%) during cell assembly and cycling due to their weak mechanical strength.

This can cause active materials to be isolated from the conductive lattice, preventing them from participating in the electrochemical reaction. We also observe that the specific capacities of full-z samples are generally lower than those of half-z samples. This reduction in capacity with increasing thickness may arise from multiple factors, including longer transport pathways in the electrolyte through the porous structure, possible limitations in electronic conductivity, and a longer solid-state diffusion distance associated with a larger feature size. The influence of micro-architecture on electrode electrochemical performance will be discussed in more detail in the next chapter.

4.7 Summary

In this chapter, we designed, synthesized, and characterized 3D LFP/C composite electrodes with tilted cubic architecture and 51 μm beam thickness. In this additive manufacturing process, a polymer scaffold is firstly printed with a DLP 3D printer, which provides high resolution and flexibility in structural design. Subsequently, metal ion and phosphate ion precursors are infused into the hydrogel scaffolds and calcined at 800℃ under an inert atmosphere, producing LFP/C composite micro-lattices with submicron pores and 201 ± 67 nm-sized LPF particles formed within the structure. The formation of well-crystalized LFP is confirmed via powder XRD analysis and the ratio between precursor ions was tuned to suppress the formation of impurity phases. The concomitant formation of carbon within the lattice provides electron transport pathways and enhances the mechanical strength, which preserves the shape integrity of the 3D structure during cell assembly and function. The carbon content in the electrode can be controlled through the precursor solution concentration and quantified via TGA. The uniform distribution of C, O, P, and Fe elements is revealed through EDS mapping. To characterize electrochemical properties, the LFP/C electrode was assembled into a coin cell against Li foil. The electrochemical activity of LFP was confirmed by the cyclic voltammetry curve. Galvanostatic charge-discharge measurements reveal a specific capacity of 160 mAh/g at C/10, which is close to the theoretical capacity of LFP.

This method is amenable to printing a wide range of electrode materials and offers the advantages of 3D architecture in enhancing overall cell electrochemical performance.

Chapter 5

STRUCTURE–TRANSPORT RELATIONSHIPS IN MICRO-ARCHITECTED LITHIUM-ION BATTERY ELECTRODES

5.1 Overview

In recent years, additive manufacturing has attracted increasing attention as a promising approach to fabricate lithium-ion battery electrodes with well-defined architectures. Experimental and modeling studies have demonstrated that the electrochemical performance of architected electrodes is influenced by their 3D structure, including geometric factors such as feature size[81], sparse density[82], planar pattern type[45], and electrode thickness[83]. Compared with conventional electrodes, in addition to low tortuosity, several studies have also demonstrated the benefits from high surface area of 3D electrodes.[84,85] However, due to the limitations in printing resolution, comparisons between different architectures may inadvertently be affected by solid-state diffusion limitations. The mechanisms by which electrode geometry influences electrochemical performance are not yet fully understood. Therefore, it remains challenging to identify and quantify the dominant geometric parameters that govern ion transport and reaction behavior in architected electrodes.

With the fabrication platform developed in the previous chapter, we investigate the structure-transport relationships in micro-architected LFP/C electrodes. Several representative geometries, including tilted cubic lattice, honeycomb with different wall thicknesses, and TPMS architecture, are fabricated with feature size varying from 18 μm to 74 μm. Their specific capacities are compared across different charge-discharge rates to identify the dominant geometric factors influencing battery performance. The results reveal that electrode tortuosity and structural feature size play critical roles in determining electrochemical behavior.

To further understand these observations, a 3D electrochemical model based on the pseudo two-dimensional (P2D) framework is developed to simulate ionic transport, reaction kinetics, and active material utilization in architected electrodes. The modeling results agree well with experimental measurements, revealing limitations from Li^+ transport in liquid electrolyte phase and from solid-state diffusion. Electrodes with lower tortuosity and smaller feature size reduce these transport limitations and achieve improved electrochemical performance. These results provide insight into how electrode architecture governs transport processes and active material utilization in 3D printed battery electrodes, thereby contributing to the design of micro-architected battery electrodes.

5.2 Influence of 3D electrode structure on electrochemical performance

To investigate the influence of the 3D electrode geometry on electrochemical performance, we fabricated additional LFP/C electrodes with a honeycomb geometry featuring two different wall thicknesses of 18 μm and 74 μm, as well as a TPMS geometry with a wall thickness of ~38 μm. CAD models of tilted cubic lattice (beam length = 1 mm, lattice thickness = 1.73 mm, porosity = 82.1%), honeycomb I (wall thickness = 50 μm, hole diameter = 0.45 mm, lattice thickness = 2 mm, porosity = 81.0%), honeycomb II (wall thickness = 200 μm, hole diameter = 1.82 mm, lattice thickness = 2 mm, porosity = 81.1%), TPMS (wall thickness = 200μm, lattice thickness = 2mm, porosity = 80.7%) were built in SolidWorks and nTop. The tilted cubic lattice beams are tilted 16.8˚ from the horizontal and formed by sweeping circles with a diameter of 400 μm. Figure 5.1 contains optical images of the 3D printed organogels with these geometries. And the as-synthesized electrodes have thickness between 630 μm and 648 μm, measured from the side-view SEM images in Figure 5.2. The active material loading of the cathodes, normalized by both area and volume, along with the electrode thicknesses are included in Table 5.1. Although we began with CAD models with similar porosity and were able to control the electrode thickness to similar values, we still observed differences in areal mass loading between different structures, which can

be attributed to variations in printing accuracy and local shrinkage among the node, beam, and wall structures with different feature sizes.

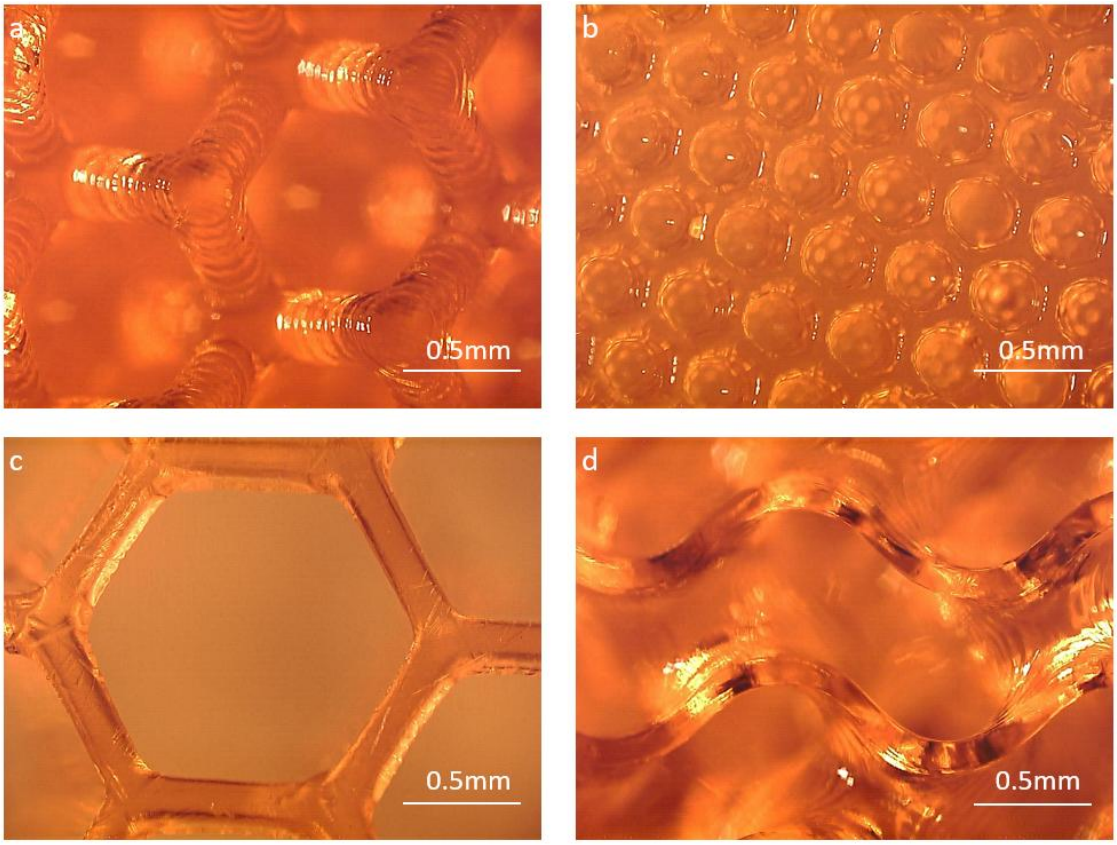

Figure 5.1. Optical images of the blank organogel with (a) tilted cube, (b) honeycomb I with wall thickness of 50 μm, (c) honeycomb II with wall thickness of 200 μm, and (d) TPMS structures.

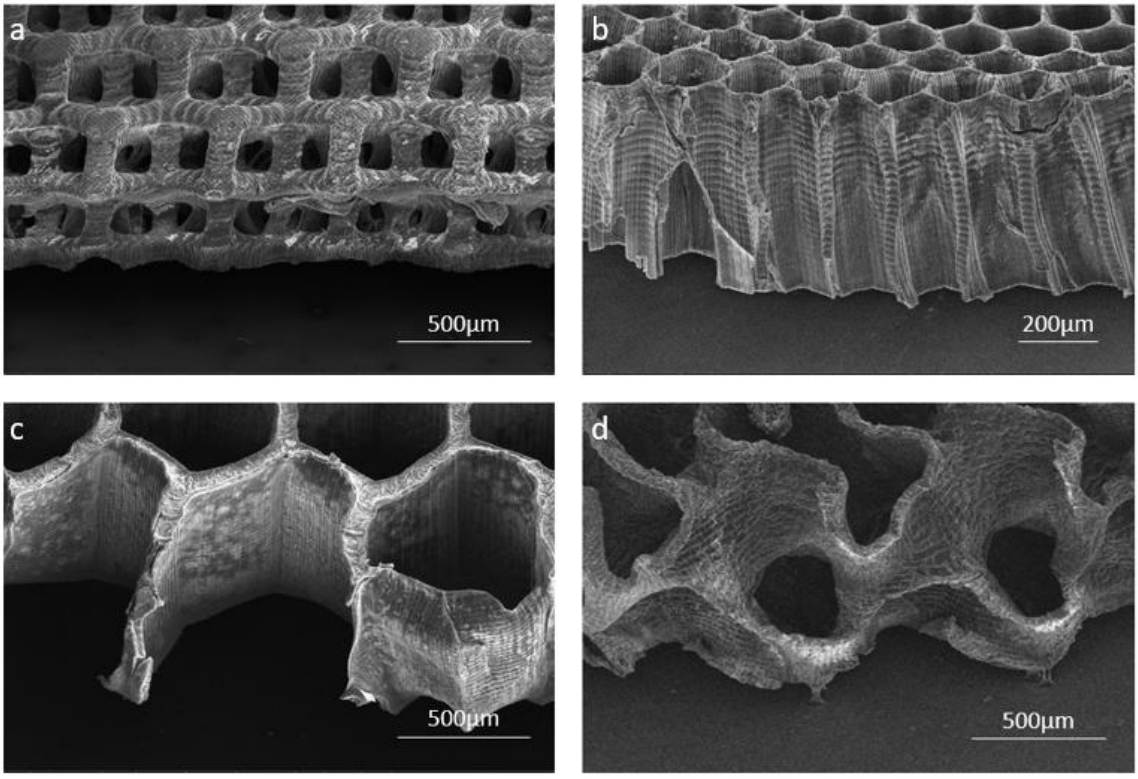

Figure 5.2. Side view (52° tilted) SEM images of the LFP/C electrodes with (a) tilted cube, (b) 18 µm honeycomb, (c) 74 µm honeycomb, and (d) TPMS structures.

Table 5.1 Areal mass loading, electrode thickness, LFP volume density, and relative density of LFP for different architectures.

	Tilted cube	Honeycomb I (18 µm)	Honeycomb II (74 µm)	TPMS
Areal mass loading (mg/cm^2)	39.7	22.3	9.9	23.9
LFP volume density (g/cm^3)	0.62	0.35	0.15	0.37
Thickness (µm)	646	630	648	642

Figure 5.3 shows images of the micro-architected electrodes with each geometry, together with their specific capacities under different charge-discharge rates. The results reveal that the TPMS electrode, which has the highest tortuosity, displays a specific capacity 40-50% lower than that of all other structures at C-rates below C/2 and maintains relatively low capacities across all C-rates. As the C-rate increases to 1C, a significant drop in capacity is observed in the tilted cube electrode, whereas both honeycomb electrodes maintain capacities higher than 120 mAh/g. Upon further increasing the C-rate to 2C, electrodes with smaller feature sizes display higher capacities. Only the honeycomb sample with 18 μm wall thickness remains electroactive at 2C, showing the highest capacity of 94 mAh/g, while the capacities of tilted cube and 74 μm honeycomb electrodes drop to near zero.

These results suggest that, under low C-rates, the electrochemical performance may be mainly limited by Li^+ transport through the electrolyte and diffusion to the electrode surface. Whereas at high C-rates (i.e., 2C), the capacity becomes dominated by the minimum feature size of the electrode architecture, as electrolyte-phase transport is no longer the rate limiting step. A direct consequence is that electrode architectures with lower tortuosity provide shorter Li^+ transport pathways in the electrolyte, thereby enhancing active material utilization. The high tortuosity of the TPMS electrodes blocks the Li^+ diffusive path through the pores, which causes a 40-50% capacity reduction compared to the other architectures. The influence of electrode tortuosity on electrochemical performance has also been reported in thick electrodes with designed pore structures[28,86,87]. The results obtained at high C-rate indicate a shift in the rate limiting step from liquid-phase Li^+ transport in the electrolyte to solid-state Li^+ diffusion within the electrode. By shortening the solid-state diffusion length, electrodes with smaller feature sizes are able to achieve better high-rate performance[44,49,88].

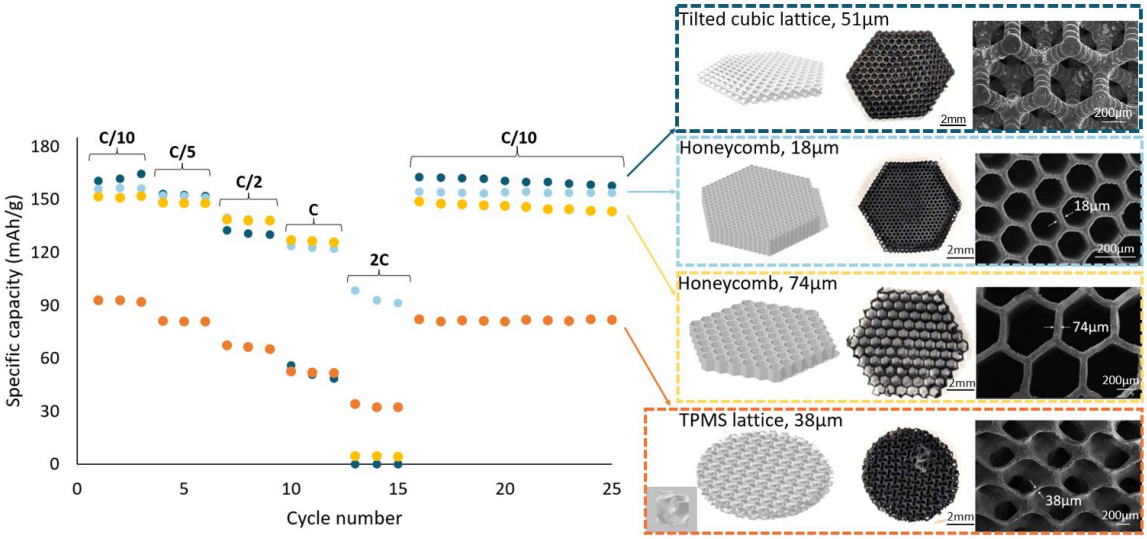

Figure 5.3. Electrochemical performance of micro-architected LFP/C electrodes. Discharge specific capacities of electrodes with tilted cube, honeycomb, and TPMS geometries at various C-rates. Insets show the CAD renderings (left), top view optical images (center), and SEM images (right) of electrodes.

5.3 3D electrochemical model for micro-architected electrodes

A 3D electrochemical model of a half-cell incorporating a micro-architected electrode was developed for finite element analysis. This model, based on Doyle and Newman's P2D framework[89], follows the approaches of Vahur et al.[90] and Bradley et al.[91]. The model includes the mechanisms of Li^+ diffusion and migration in the separator and electrolyte, electrochemical reaction on the electrode-electrolyte interface, solid-state Li^+ diffusion within cathode, and electronic transport within cathode. The schematic of the model is shown in Figure 5.4. The model includes three domains: separator, liquid electrolyte, and solid electrode. The left boundary is the interface between the Li anode and separator, while the right boundary is the interface between cathode and current collector. All the other outside boundaries are set as insulation and no flux. The geometry models are rebuilt according to the SEM images.

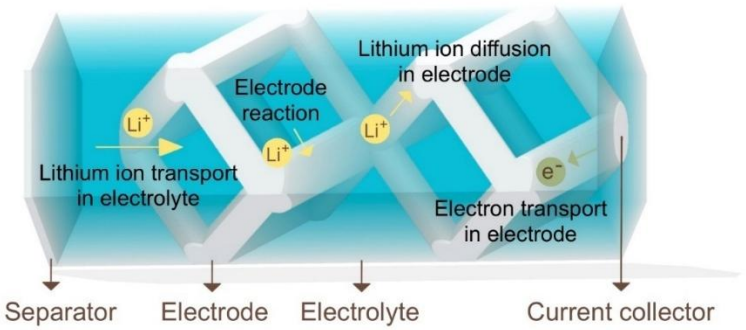

Figure 5.4. Schematic of the 3D electrochemical model built for a half cell with 3D architected cathode.

The conservation of charge and mass in electrolyte is described as:

$$\nabla \cdot \boldsymbol{i}_l = \nabla \cdot \left(-\sigma_l \nabla \phi_l + \frac{2\sigma_l RT}{F}\left(1 + \frac{\partial ln f}{\partial ln c_l}\right)(1 - t_+)\nabla ln c_l\right) = 0 \tag{13}$$

$$-\nabla \cdot \boldsymbol{J}_l = \nabla \cdot (D_l \nabla c_l - \frac{\boldsymbol{i}_l t_+}{F}) = \frac{\partial c_l}{\partial t} \tag{14}$$

Here, φ_l and c_l are the potential and local Li^+ concentration in electrolyte. The electrolyte conductivity σ_l, electrolyte diffusion coefficient D_l, mean molar activity coefficient f, and transference number of positive ions t_+ are determined by Equations (15) - (18)[92], where c_{ref} = 1000 mol/m^3

$$\sigma_l = 1.147\left(\frac{c_l}{c_{ref}}\right)^3 - 22.38\left(\frac{c_l}{c_{ref}}\right)^{1.5} + 29.15\frac{c_l}{c_{ref}}\ [S/m] \tag{15}$$

$$D_l = 7.588 \cdot 10^{-11}\left(\frac{c_l}{c_{ref}}\right)^2 - 3.036 \cdot 10^{-10}\frac{c_l}{c_{ref}} + 3.654 \cdot 10^{-10}\ [m^2/s] \tag{16}$$

$$t_+ = -0.1291\left(\frac{c_l}{c_{ref}}\right)^3 + 0.3517\left(\frac{c_l}{c_{ref}}\right)^2 - 0.4893\frac{c_l}{c_{ref}} + 0.4287 \tag{17}$$

$$1 + \frac{\partial lnf}{\partial lnc_l} = \frac{0.2731\left(\frac{c_l}{c_{ref}}\right)^2 + 0.6352\frac{c_l}{c_{ref}} + 0.4577}{0.1291\left(\frac{c_l}{c_{ref}}\right)^3 - 0.3517\left(\frac{c_l}{c_{ref}}\right)^2 + 0.4893\frac{c_l}{c_{ref}} + 0.5713} \tag{18}$$

The effective conductivity $\sigma_{l,eff}$ and diffusion coefficient $D_{l,eff}$ used in the separator domain is estimated by the Bruggeman's relation[93], where ε_l is the electrolyte volume fraction:

$$\sigma_{l,eff} = \varepsilon_l^{1.5}\sigma_l \qquad D_{l,eff} = \varepsilon_l^{1.5}D_l \tag{19}$$

and the conservation of charge and mass in separator is described as:

$$\nabla \cdot \boldsymbol{i}_l = \nabla \cdot \left(-\sigma_{l,eff}\nabla\phi_l + \frac{2\sigma_{l,eff}RT}{F}\left(1 + \frac{\partial lnf}{\partial lnc_l}\right)(1 - t_+)\nabla lnc_l\right) = 0 \tag{20}$$

$$-\nabla \cdot \boldsymbol{J}_l = \nabla \cdot (D_{l,eff}\nabla c_l - \frac{\boldsymbol{i}_l t_+}{F}) = \frac{\partial c_l}{\partial t} \tag{21}$$

Li^+ transport with in cathode is described by solid-state diffusion (Equation 22), and the electronic current density is governed by Ohm's law (Equation 23):

$$-\nabla \cdot \boldsymbol{J}_s = \nabla \cdot (D_s\nabla c_s) = \frac{\partial c_s}{\partial t} \tag{22}$$

$$\nabla \cdot \boldsymbol{i}_s = \nabla \cdot (-\sigma_s\nabla\phi_s) = 0 \tag{23}$$

Here, φ_s and c_s are the potential and local Li^+ concentration inside electrode. σ_s is the electrical conductivity and D_s is the diffusion coefficient of LFP electrode.

The boundary condition at the cathode-electrolyte interface is given by the Butler-Volmer kinetic expression, determining the electrochemical reaction rate at the interface:

$$i_{loc} = i_0 \left(exp\left(\frac{\alpha_a F\eta}{RT}\right) - exp\left(\frac{-\alpha_c F\eta}{RT}\right) \right) \tag{24}$$

The local current density i_{loc} is determined by the overpotential η and the exchange current density i_0:

$$\eta = \phi_s - \phi_l - E_{eq} \tag{25}$$

$$i_0 = F k_0 c_s^{\alpha_c} (c_{s,max} - c_s)^{\alpha_a} c_l^{\alpha_a} \tag{26}$$

Here E_{eq} and k_0 are the equilibrium potential and reaction rate constant. The flux and current into and out of this interface are described as:

$$\boldsymbol{n} \cdot \boldsymbol{J}_l = -\boldsymbol{n} \cdot \boldsymbol{J}_s = \frac{i_{loc}}{F} \tag{27}$$

$$\boldsymbol{n} \cdot \boldsymbol{i}_l = -\boldsymbol{n} \cdot \boldsymbol{i}_s = i_{loc} \tag{28}$$

Here $\boldsymbol{n}$ is the interface normal direction. The boundary condition of anode-separator is given by the kinetics of a lithium metal electrode, where the exchange current density $i_0 = F k_{Li} c_l^{\alpha_a}$, equilibrium potential $E_{eq} = 0$, and external electric potential $\varphi_s = 0$ is applied for the Butler-Volmer expression.

A constant current $I_{app} = \int_{\partial\Omega} \boldsymbol{i}_s \cdot \boldsymbol{n}\, dS$ is applied on the cathode-current collector interface to control the discharge rate, and the average potential on this interface is recorded as the cell voltage. All of the material parameters used in this model are listed in Table 5.2.

The initial Li^+ concentrations were set as $c_l = 1000$ mol/m^3 and $c_s = 228$mol/m^3 (SOC = 0.01), and the initial values for potentials are $\varphi_l = 0$V, $\varphi_s = E_{eq}$(SOC=0.01). A current distribution initialization step is applied before the time dependent discharge. The fully charged unit cells of tilted cube and honeycomb structure (wall thickness = 18 μm) were then discharged at C/10, 1C, and 2C until the voltage reached 2.5 V. In Figure 5.5, the simulation results (red dot) and the experimental charge-discharge data (black dots) under C/10 exhibit good

agreement. To show the trajectory of Li^+, starting point controlled streamline of Li^+ flux in electrolyte is generated at t = 30 min under 1C.

Table 5.2. Parameters used in electrochemical modeling

Parameters		Values	Units
σ_s	electrical conductivity of LFP	16 [94]	S m^{-1}
D_s	electrode diffusion coefficient	3.2×10^{-13} [95]	m^2 s
$c_{s,max}$	maximum concentration in LFP	22806 [96]	mol m^3
k_0	reaction rate constant of LFP	1.4×10^{-12} [96]	$m^{2.5}$ $mol^{-0.5}$ s^{-1}
k_{Li}	reaction rate constant of Li	10^{-4} [97]	$m^{-0.5}$ $mol^{0.5}$ s^{-1}
α_a	anodic transfer coefficient	0.5	-
α_c	cathodic transfer coefficient	0.5	-
ε_l	electrolyte volume fraction	0.39	-
T	temperature	293.15	K
R	molar gas constant	8.314	J mol^{-1} K^{-1}
F	Faraday constant	96487	C mol^{-1}

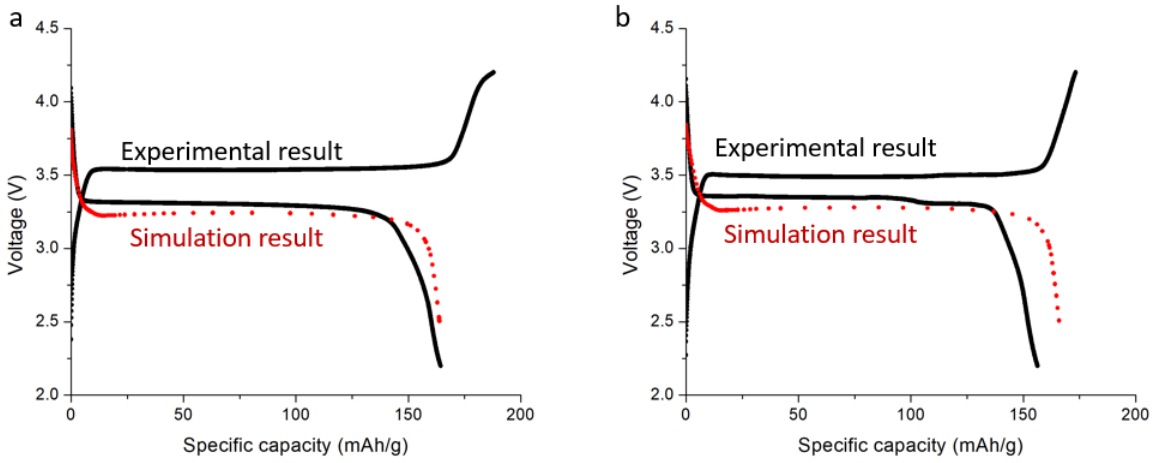

Figure 5.5 The discharge curve from the time dependent simulation (red dot) and the experimental charge-discharge curve (black line) for (a) tilted cube and (b) honeycomb electrodes at C/10.

5.4 Influence of 3D electrode structures on electrochemical performance

In the simulation, fully charged unit cells with tilted cube (porosity = 83.5%, thickness = 630 μm, feature size = 49 μm) and honeycomb (porosity = 79.5%, thickness = 629 μm, feature size = 18 μm) geometries were discharged at C/10, 1C, and 2C until the cell voltage dropped to 2.5 V. We applied this model to analyze ionic transport and the SOC, defined as the ratio of the local Li concentration to the maximum Li concentration LFP can hold, which represents the local utilization of active material. We did not analyze the TPMS geometry due to its low-capacity performance. Figure 5.6 contains the SOC distribution at the end of discharge and conveys the presence of an SOC gradient through the electrode thickness as the discharge rate increases. Limited by the Li^+ transport in electrolyte, the depletion of Li^+ in electrolyte near the current collector leads to a substantial reduction in SOC in this region. A detailed discussion about Li^+ concentration distribution in electrolyte is provided in section 5.5. This effect is more pronounced in the tilted cube electrode, which has higher tortuosity and longer Li^+ transport distance. We define the tortuosity as the length of the diffusive trajectory in electrolyte divided by the straight distance from the start point to the end point.

Figure 5.7 a-d shows the Li^+ flux and corresponding trajectories at 50% SOC. The tortuosity is 1.22 ± 0.18 for the tilted cube geometry compared with 1.01 ± 0.02 for the honeycomb (Figure 5.7e).

The SOC inside the beams and nodes of tilted cube significantly decreases at 2C, indicating that solid-state diffusion limits active material utilization. We did not observe this phenomenon in the honeycomb electrode, where the smaller feature size (18 μm) enables relatively high material utilization inside the walls. These simulation results further support our hypothesis that the electrochemical performance of micro-architected electrodes is mainly limited by Li^+ transport in electrolyte at low discharge rates and by solid-state diffusion within electrode at high discharge rate.

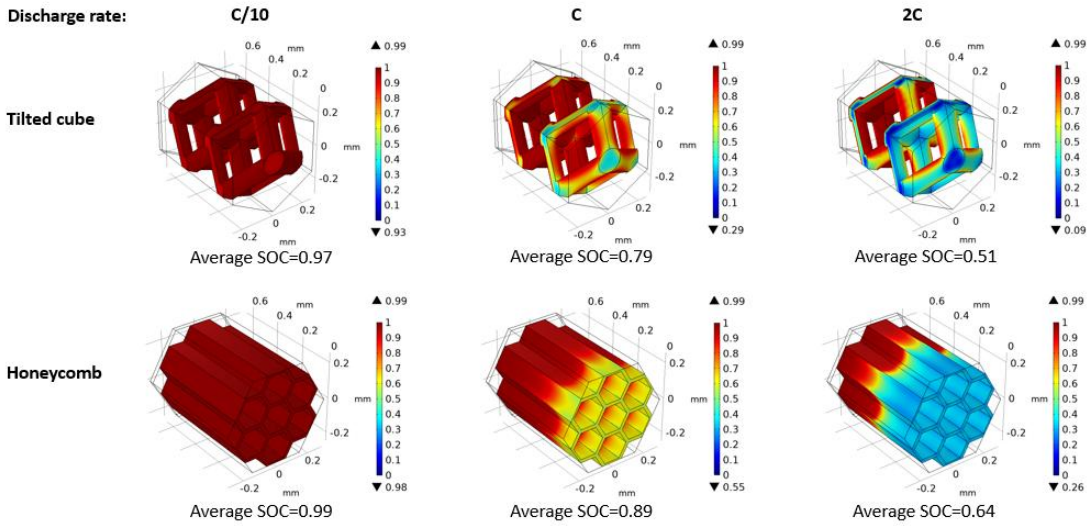

Figure 5.6. SOC distribution in tilted cube and honeycomb unit cells at the end of discharge under various C-rates.

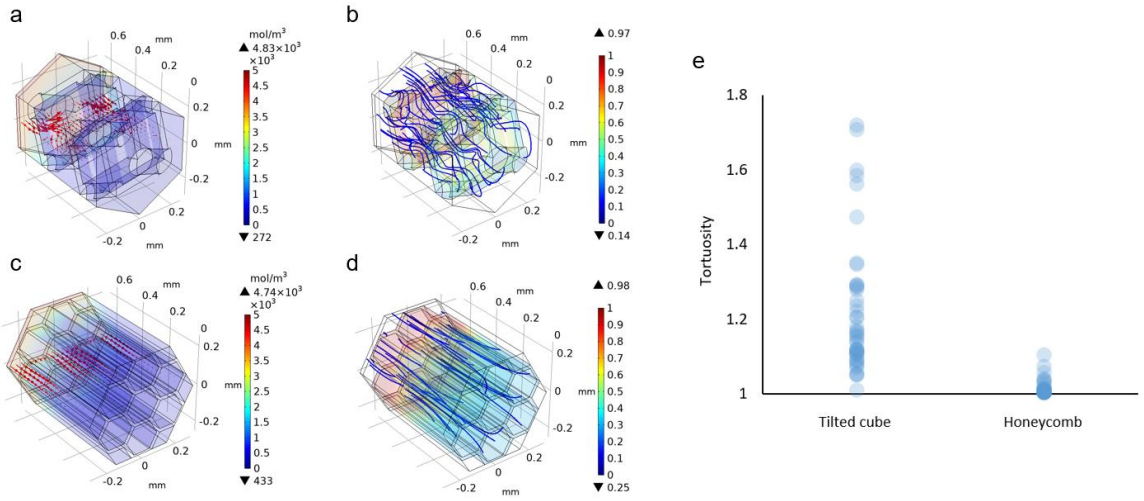

Figure 5.7 Li^+ flux vectors (red arrows) with a) tilted cube and c) honeycomb electrodes at 50% SOC with a discharge rate of 1C, overlaid on the electrolyte Li^+ concentration map. Streamlines of Li^+ flux with b) tilted cube and d) honeycomb electrodes at 50% SOC with a discharge rate of 1C, overlaid on the electrode SOC distribution. e) Tortuosity for each structure, 45 streamlines were calculated.

5.5 Discussion of Li^+ Concentration Distribution in the Electrolyte

The evolution of Li^+ concentration is analyzed using the 3D half-cell electrochemical model. Cells with the tilted cubic and 18 μm honeycomb 3D electrodes are initialized with a uniform Li^+ concentration of 1000 mol/m^3 in the electrolyte. The Li^+ concentration distributions in electrolyte at SOC = 50%, when the cells are discharged at C/10, C, and 2C, are shown in Figure 5.8. The Li^+ concentration in electrolyte exhibits a tendency similar to that of SOC distribution in the electrode, developing an obvious gradient from the separator toward the current collector at 1C, with the gradient becoming increasingly severe as the discharge rate increases. This effect is more pronounced with the tilted cubic electrode, which has higher tortuosity and longer Li^+ transport pathway, resulting in a minimum Li^+ concentration of 272 mol/m^3 at 1C and 9.45 mol/m^3 at 2C. These simulation results indicate that Li^+ depletion and insufficient ionic transport in the electrolyte lead to severely reduced Li^+ concentration in the

bottom region (near current collector), which suppresses the local electrochemical reaction rate and results in reduced active material utilization in this region.

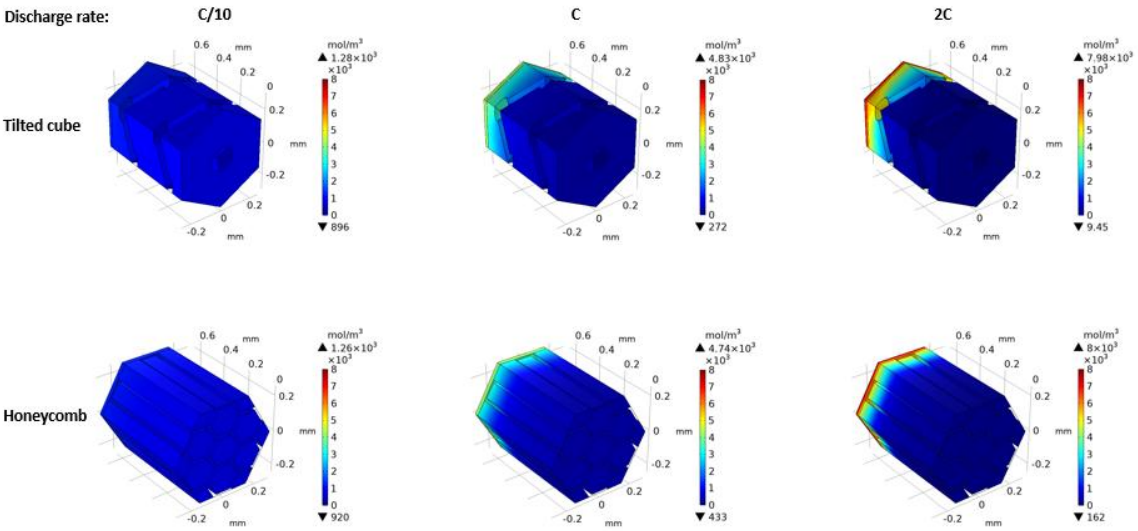

Figure 5.8. Distribution of Li ion concentration in electrolyte at 50% SOC.

5.6 Discussion of electronic percolation limitations

Given the intrinsically low electronic conductivity of LFP and the relatively thick electrodes, the percolation of electronically conductive material can also influence polarization and rate performance. In particular, the high aspect ratio architecture (thin beams and walls) could introduce local electronic resistance.[98] The in-situ formation of a carbon network via pyrolysis during the LFP synthesis has been proven to significantly improve the conductivity and rate capabilities.[79,99] For instance, Delacourt et al. reported that a 4.75 wt.% carbon coating formed by thermal decomposition of additional carbon source (citric acid and ethylene glycol) at 700 °C are able to increase the conductivity of LFP from the order of 10^{-9} S/cm to 0.16 S/cm.[100] In our system, 25.6 wt.% amorphous carbon concomitantly formed inside the structure was expected to provide improved electronic transport. To estimate the electronic conductivity, the resistance of a honeycomb electrode was tested by using copper

foil as contacts on the top and bottoms faces (Figure 5.9a, b), measuring a resistance of R = 4.6 Ω. The effective area (A = 0.084 cm^2) was estimated based on the top-view SEM image in Figure 5.9c. The surface exhibited partial mechanical damage during the resistance test, while the main structure remained intact. The thickness (t = 677 µm) was measured from the side-view (52° tilted) SEM image in Figure 5.9d. An apparent conductivity of approximately 0.18 S/cm was calculated by:

$$\sigma = \frac{t}{R \cdot A} \tag{29}$$

Considering that this two-probe measurement includes contact resistance, the calculated value should be regarded as a lower bound. Therefore, the material conductivity is expected to be on the order of 10^{-1} S/cm.

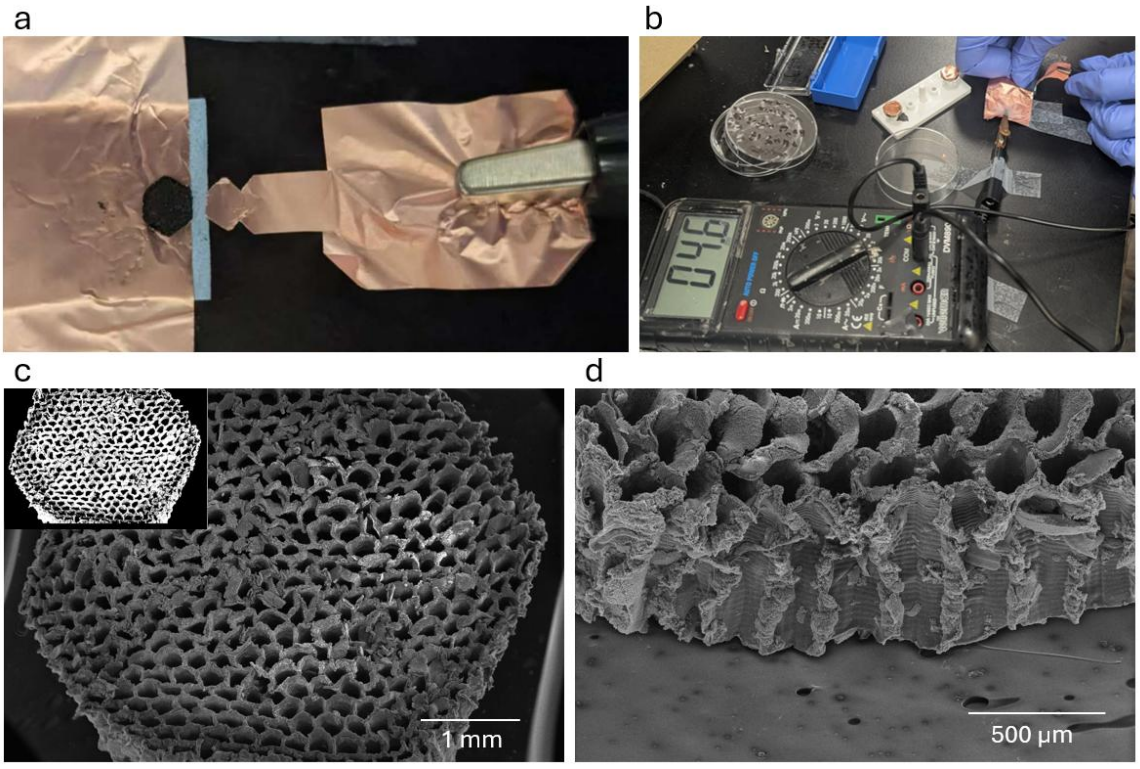

Figure 5.9 Experimental setup for conductivity measurement. a, b) Copper foil was contacted onto the top and bottom side of a honeycomb electrode. c) Top-view SEM image after the resistance test. Inset shows the estimated cross-section area. d) 52° tilted side-view SEM image.

We examined the simulated potential distributions in electrode φ_s and electrolyte φ_l at the final time step (Figures 5.10 and 5.11). The results indicate that the ohmic overpotential accounts for part of the voltage drop at high charge rates, but its contribution is negligible at moderate discharge rate (e.g., 1C) or in the honeycomb structure. In contrast, a significant potential drop is observed in the electrolyte phase (Figure 5.11), which is coupled with the migration of Li^+ in electrolyte and can help to explain the noticeable polarization in experimental results. Considering that these simulations were performed using relatively high electronic conductivity (0.16 S/cm), applying a lower conductivity may exacerbate the limitation from electronic resistance.

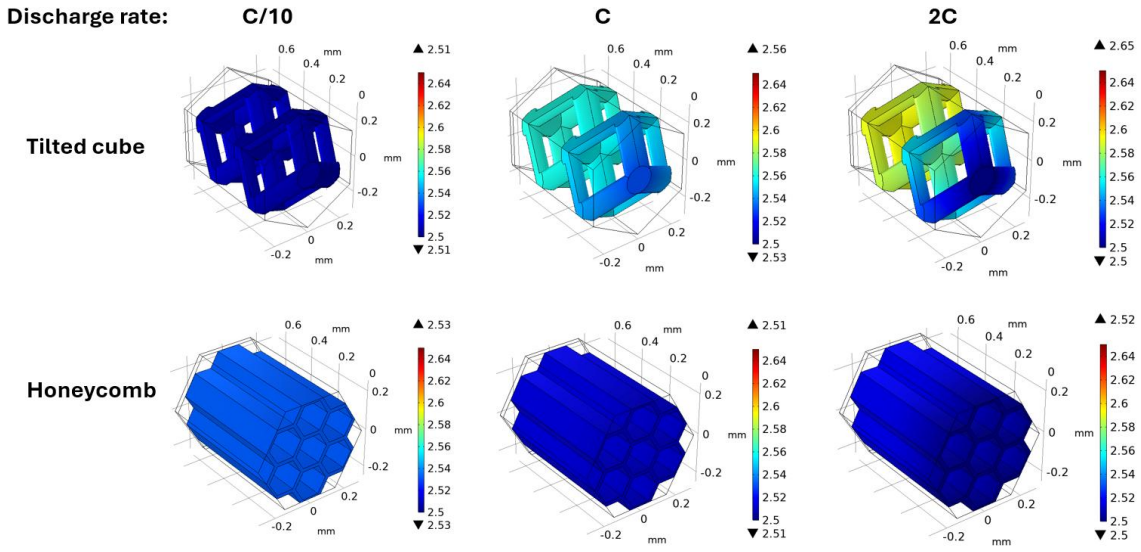

Figure 5.10 Potential distributions in electrode at the final time step.

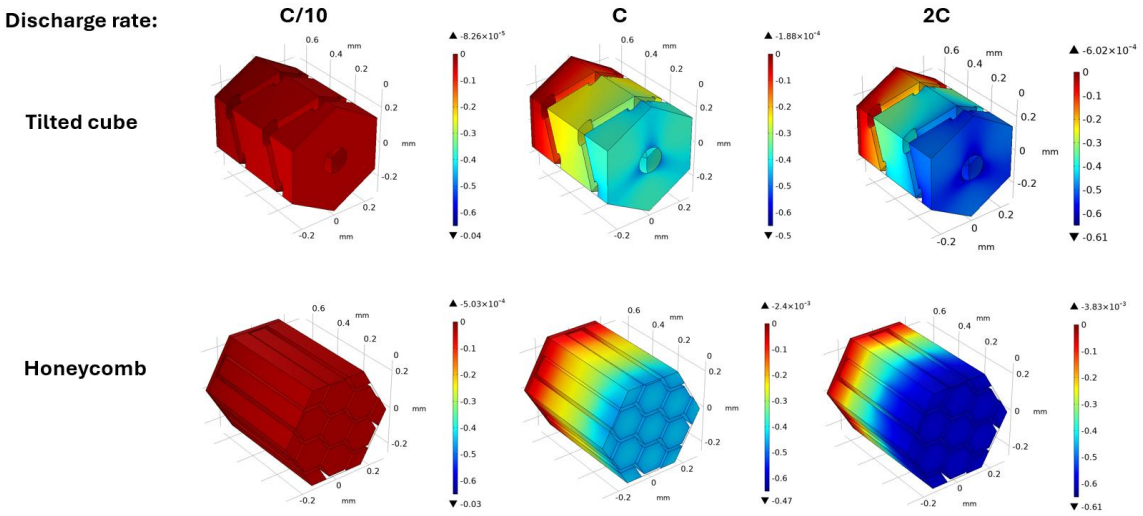

Figure 5.11 Potential distributions in electrolyte at the final time step.

5.7 Summary

To investigate the structure-transport relationships with micro-architected LFP/C electrodes, in addition to the tilted cubic lattice, electrodes with honeycomb and TPMS geometries were synthesized, with a minimum feature size varying from 18 μm to 74 μm. Benefiting from low tortuosity and small feature size, the honeycomb structure with 18 μm wall thickness exhibits the best rate performance due to promoted ion transport. An electrochemical model that incorporates the specific electrode geometry with respect to the ionic flow was developed, demonstrating the dominant effect of Li^+ transport in electrolyte and Li^+ diffusion in electrodes on the active material utilization. These results provide insight into the role of electrode architecture in governing transport processes and active material utilization, contributing to the design of micro-architected electrodes.

Chapter 6

SUMMARY AND OUTLOOK

6.1 Summary

In this work, we began with an investigation of the mechanical behavior of lithium-ion battery electrodes at the micro- and submicroscale, including both electrodeposited LCO cathodes and Li-based composite anodes. Then, we developed a HIAM-based additive manufacturing method to fabricate micro-architected LFP/C composite electrodes and explored the structure-transport relationships in these 3D architected lithium-ion battery electrodes.

The mechanical behavior of electrode materials was investigated using in situ nanoindentation and micro-pillar compression experiments. To determine the intrinsic mechanical properties of charged LCO crystals while minimizing grain boundary and air exposure effects, nanoindentation was performed with a custom mechanical testing system inside an SEM. The results show that the elastic modulus and hardness decrease with increasing SOC due to Li deintercalation and the expansion of the layered LCO structure. The recovery of mechanical properties during discharge indicates that the changes are mainly governed by Li concentration rather than structural damage. Fracture toughness measurements on the electrode cross-section reveal a 20% reduction near the current collector after delithiation, which is attributed to the formation of cracks and voids.

In addition, the mechanical behavior of Li/rGO anodes was studied through uniaxial compression experiments on FIB-milled micro-pillars. The Li/rGO composite exhibits reduced elastic modulus and yield strength due to the collapse of pore-rich regions. The nanoindentation measurements on Li/Na anodes show that the Na filler decreases the overall modulus and exhibits 54% lower hardness than the Li phase in the composite. The

deformability of the Na phase can reduce void formation and improve interfacial contact in solid-state batteries. Following the investigation of electrode mechanical properties, we further conducted studies on micro-architected electrodes.

We demonstrated that the HIAM technique is capable of fabricating micro-architected LFP/C composite electrodes with high resolution and complex geometries. The formation of carbon within the lattice significantly enhanced the mechanical strength of the electrodes, providing sufficient mechanical support for cell assembly. We investigated the influence of geometric factors, including feature size and tortuosity, on the electrochemical performance of electrodes with tilted cube, honeycomb, and TPMS geometries. We found that Li^+ transport in the liquid electrolyte is the rate-limiting factor at low charge-discharge rates. As the rate increases, the dominant limitation shifts to Li^+ diffusion within the electrode. To further understand these observations, a 3D electrochemical model was developed, revealing the impact of architectural features on Li^+ transport and active material utilization.

Although the volumetric energy density is currently limited by the high porosity, our results suggest a viable design strategy for future architected electrodes. Specifically, architecture with low tortuosity pathways can facilitate ionic transport through the electrolyte, whereas reduced feature size on the order of ~20 μm and minimized node size help alleviate solid-state diffusion limitations. Further optimization, such as decreasing pore size and overall porosity, may improve volumetric utilization without compromising rate performance.

6.2 Outlook: Interpenetrated electrodes for lithium-ion batteries

Most 3D printed electrodes reported to date are integrated into batteries using a sandwich-type configuration, in which the cathode and anode are separated by a planar separator or solid electrolyte and assembled in a stacked geometry, so as in this work. In such systems, the porous architecture of 3D printed electrodes can help to enhance lithium-ion transport within thick electrodes by introducing low-tortuosity pathways filled with electrolyte. This approach has been widely explored as a strategy to increase electrode mass loading while

maintaining reasonable rate performance. In this work, the high resolution by our HIAM-based approach enabled sufficiently small feature sizes, thereby minimizing limitations from solid-state diffusion within the electrode at charge-discharge rate below 2C. The honeycomb architecture with 18 μm wall thickness exhibits a mass loading of 22.3 mg/cm^2 and delivers an areal capacity of 2.1 mAh/cm^2 at 2C, indicating its potential to simultaneously achieve high areal capacity and rate capability.

Despite these structural advantages, the electrochemical performance of these ~630 μm thick electrodes with ~80% porosity remains limited by lithium-ion transport through the liquid electrolyte phase. As the electrode thickness increases, we would expect that the transport distance within the electrolyte-filled pores becomes progressively longer, leading to a more severe concentration gradient and increased ionic resistance. This observation highlights an inherent limitation of the conventional sandwich-type battery architecture, in which ionic transport between the cathode and anode must occur across the full thickness of the electrode-separator-electrode stack. In such configurations, increased electrode thickness impairs ion transport and limits the full potential of micro-architected electrodes to achieve high areal capacity.

One promising strategy to overcome this limitation is the development of 3D interpenetrated electrode architectures, in which the cathode and anode are spatially interwoven within a shared electrolyte network. In this case, the ionic transport distance between electrodes can be dramatically reduced to the distance between the adjacent lattice beams, enabling high-rate operation even with large electrode thickness and high active material loading. From a transport perspective, interpenetrated electrodes can effectively decouple electrode thickness from ionic transport distance, allowing thick electrodes to maintain efficient ionic transport. Additive manufacturing provides an attractive platform for realizing such interpenetrated architectures, as it enables precise spatial control over electrode geometry and material distribution. Several studies have fabricated comb-shaped interdigitated electrodes using extrusion-based 3D printing[39,101,102], demonstrating the capability of this architecture to

support high areal capacity. However, due to the viscous nature of the ink, these layer-by-layer stacking strategies usually have limitations in the aspect ratio of the structures and the electrode thickness. In this case, our HIAM-based approach provides a practical route to fabricate these complex structures with well-defined geometries and high resolution.

Overall, this work looks at the roles of materials, mechanics, and 3D architectures in lithium-ion batteries. A fabrication platform for micro-architected electrodes is developed to understand how these 3D structures are connected to battery performance. In addition, there remains significant opportunity to further improve these designs and advance them toward practical applications.

BIBLIOGRAPHY

(1) Degen, F.; Winter, M.; Bendig, D.; Tübke, J. Energy Consumption of Current and Future Production of Lithium-Ion and Post Lithium-Ion Battery Cells. *Nat. Energy* **2023**, *8* (11), 1284–1295. https://doi.org/10.1038/s41560-023-01355-z.

(2) *Lithium-Ion Batteries: A Pillar for a Fossil Fuel-Free Economy.*; Frontier Technology Issues; United Nations Department of Economic and Social Affairs, 2021.

(3) Sarma, D. D.; Shukla, A. K. Building Better Batteries: A Travel Back in Time. *ACS Energy Lett.* **2018**, *3* (11), 2841–2845. https://doi.org/10.1021/acsenergylett.8b01966.

(4) Mizushima, K.; Jones, P. C.; Wiseman, P. J.; Goodenough, J. B. LixCoO2 (0< X<-1): A New Cathode Material for Batteries of High Energy Density. *Mater. Res. Bull.* **1980**, *15(6)*, 783–789.

(5) Ozawa, K. Lithium-Ion Rechargeable Batteries with LiCoO2 and Carbon Electrodes: The LiCoO2/C System. *Solid State Ion.* **1994**, *69* (3–4), 212–221. https://doi.org/10.1016/0167-2738(94)90411-1.

(6) Chu, B.; Guo, Y.-J.; Shi, J.-L.; Yin, Y.-X.; Huang, T.; Su, H.; Yu, A.; Guo, Y.-G.; Li, Y. Cobalt in High-Energy-Density Layered Cathode Materials for Lithium Ion Batteries. *J. Power Sources* **2022**, *544*, 231873. https://doi.org/10.1016/j.jpowsour.2022.231873.

(7) Hu, J.; Huang, W.; Yang, L.; Pan, F. Structure and Performance of the $LiFePO_4$ Cathode Material: From the Bulk to the Surface. *Nanoscale* **2020**, *12* (28), 15036–15044. https://doi.org/10.1039/D0NR03776A.

(8) Zhang, W.-J. Structure and Performance of LiFePO4 Cathode Materials: A Review. *J. Power Sources* **2011**, *196* (6), 2962–2970. https://doi.org/10.1016/j.jpowsour.2010.11.113.

(9) Chang, H.; Wu, Y.-R.; Han, X.; Yi, T.-F. Recent Developments in Advanced Anode Materials for Lithium-Ion Batteries. *Energy Mater.* **2022**, *1* (1), 100003. https://doi.org/10.20517/energymater.2021.02.

(10) Guo, Y.; Li, H.; Zhai, T. Reviving Lithium-Metal Anodes for Next-Generation High-Energy Batteries. *Adv. Mater.* **2017**, *29* (29), 1700007. https://doi.org/10.1002/adma.201700007.

(11) Morzy, J. K.; Dose, W. M.; Vullum, P. E.; Lai, M. C.; Mahadevegowda, A.; De Volder, M. F. L.; Ducati, C. Origins and Importance of Intragranular Cracking in Layered Lithium Transition Metal Oxide Cathodes. *ACS Appl. Energy Mater.* **2024**, *7* (9), 3945–3956. https://doi.org/10.1021/acsaem.4c00279.

(12) Jiang, Y.; Yan, P.; Yu, M.; Li, J.; Jiao, H.; Zhou, B.; Sui, M. Atomistic Mechanism of Cracking Degradation at Twin Boundary of LiCoO2. *Nano Energy* **2020**, *78*, 105364. https://doi.org/10.1016/j.nanoen.2020.105364.

(13) Naik, K. G.; Vishnugopi, B. S.; Datta, J.; Datta, D.; Mukherjee, P. P. Electro-Chemo-Mechanical Challenges and Perspective in Lithium Metal Batteries. *Appl. Mech. Rev.* **2023**, *75* (1), 010802. https://doi.org/10.1115/1.4057039.

(14) Reimers, J. N.; Dahn, J. R. Electrochemical and In Situ X-Ray Diffraction Studies of Lithium Intercalation in Li x CoO2. *J. Electrochem. Soc.* **1992**, *139* (8), 2091–2097. https://doi.org/10.1149/1.2221184.

(15) Monroe, C.; Newman, J. The Impact of Elastic Deformation on Deposition Kinetics at Lithium/Polymer Interfaces. *J. Electrochem. Soc.* **2005**, *152* (2), A396. https://doi.org/10.1149/1.1850854.

(16) Sharafi, A.; Meyer, H. M.; Nanda, J.; Wolfenstine, J.; Sakamoto, J. Characterizing the Li–Li7La3Zr2O12 Interface Stability and Kinetics as a Function of Temperature and Current Density. *J. Power Sources* **2016**, *302*, 135–139. https://doi.org/10.1016/j.jpowsour.2015.10.053.

(17) Ni, J. E.; Case, E. D.; Sakamoto, J. S.; Rangasamy, E.; Wolfenstine, J. B. Room Temperature Elastic Moduli and Vickers Hardness of Hot-Pressed LLZO Cubic Garnet. *J. Mater. Sci.* **2012**, *47* (23), 7978–7985. https://doi.org/10.1007/s10853-012-6687-5.

(18) Kerman, K.; Luntz, A.; Viswanathan, V.; Chiang, Y.-M.; Chen, Z. Review—Practical Challenges Hindering the Development of Solid State Li Ion Batteries. *J. Electrochem. Soc.* **2017**, *164* (7), A1731–A1744. https://doi.org/10.1149/2.1571707jes.

(19) Xu, C.; Ahmad, Z.; Aryanfar, A.; Viswanathan, V.; Greer, J. R. Enhanced Strength and Temperature Dependence of Mechanical Properties of Li at Small Scales and Its Implications for Li Metal Anodes. *Proc. Natl. Acad. Sci.* **2017**, *114* (1), 57–61. https://doi.org/10.1073/pnas.1615733114.

(20) Krauskopf, T.; Hartmann, H.; Zeier, W. G.; Janek, J. Toward a Fundamental Understanding of the Lithium Metal Anode in Solid-State Batteries—An Electrochemo-Mechanical Study on the Garnet-Type Solid Electrolyte $Li_{6.25}$ $Al_{0.25}$ La_3 Zr_2 O_{12}. *ACS Appl. Mater. Interfaces* **2019**, *11* (15), 14463–14477. https://doi.org/10.1021/acsami.9b02537.

(21) Gireaud, L.; Grugeon, S.; Laruelle, S.; Yrieix, B.; Tarascon, J.-M. Lithium Metal Stripping/Plating Mechanisms Studies: A Metallurgical Approach. *Electrochem. Commun.* **2006**, *8* (10), 1639–1649. https://doi.org/10.1016/j.elecom.2006.07.037.

(22) Heubner, C.; Nikolowski, K.; Reuber, S.; Schneider, M.; Wolter, M.; Michaelis, A. Recent Insights into Rate Performance Limitations of Li-ion Batteries. *Batter. Supercaps* **2021**, *4* (2), 268–285. https://doi.org/10.1002/batt.202000227.

(23) Gao, H.; Wu, Q.; Hu, Y.; Zheng, J. P.; Amine, K.; Chen, Z. Revealing the Rate-Limiting Li-Ion Diffusion Pathway in Ultrathick Electrodes for Li-Ion Batteries. *J. Phys. Chem. Lett.* **2018**, *9* (17), 5100–5104. https://doi.org/10.1021/acs.jpclett.8b02229.

(24) Weng, S.; Yang, G.; Zhang, S.; Liu, X.; Zhang, X.; Liu, Z.; Cao, M.; Ateş, M. N.; Li, Y.; Chen, L.; Wang, Z.; Wang, X. Kinetic Limits of Graphite Anode for Fast-Charging

Lithium-Ion Batteries. *Nano-Micro Lett.* **2023**, *15* (1), 215. https://doi.org/10.1007/s40820-023-01183-6.

(25) Wang, J.; Wang, M.; Ren, N.; Dong, J.; Li, Y.; Chen, C. High-Areal-Capacity Thick Cathode with Vertically-Aligned Micro-Channels for Advanced Lithium Ion Batteries. *Energy Storage Mater.* **2021**, *39*, 287–293. https://doi.org/10.1016/j.ensm.2021.04.030.

(26) Sander, J. S.; Erb, R. M.; Li, L.; Gurijala, A.; Chiang, Y.-M. High-Performance Battery Electrodes via Magnetic Templating. *Nat. Energy* **2016**, *1* (8), 16099. https://doi.org/10.1038/nenergy.2016.99.

(27) He, R.; Tian, G.; Li, S.; Han, Z.; Zhong, W.; Cheng, S.; Xie, J. Enhancing the Reversibility of Lithium Cobalt Oxide Phase Transition in Thick Electrode via Low Tortuosity Design. *Nano Lett.* **2022**, *22* (6), 2429–2436. https://doi.org/10.1021/acs.nanolett.2c00123.

(28) Xu, Y.; Lin, Z.; Zhong, X.; Huang, X.; Weiss, N. O.; Huang, Y.; Duan, X. Holey Graphene Frameworks for Highly Efficient Capacitive Energy Storage. *Nat. Commun.* **2014**, *5* (1), 4554. https://doi.org/10.1038/ncomms5554.

(29) Kuang, Y.; Chen, C.; Pastel, G.; Li, Y.; Song, J.; Mi, R.; Kong, W.; Liu, B.; Jiang, Y.; Yang, K.; Hu, L. Conductive Cellulose Nanofiber Enabled Thick Electrode for Compact and Flexible Energy Storage Devices. *Adv. Energy Mater.* **2018**, *8* (33), 1802398. https://doi.org/10.1002/aenm.201802398.

(30) Lee, D.; Jung, A.; Liu, P.; Yeom, B. Coordinated Self-Assembly of Ultraporous 3D Aramid Nanofibrous Separators with a Poly(Vinyl Alcohol) Sheath for Lithium-Metal Batteries. *Energy Storage Mater.* **2024**, *65*, 103107. https://doi.org/10.1016/j.ensm.2023.103107.

(31) Hu, Y.; Gu, D.; Jiang, H.; Wang, L.; Sun, H.; Wang, J.; Shen, L. Electrochemical Performance of LiFePO₄/C via Coaxial and Uniaxial Electrospinning Method. *Adv. Chem. Eng. Sci.* **2016**, *06* (02), 149–157. https://doi.org/10.4236/aces.2016.62017.

(32) Arrese-Igor, M.; Vong, M.; Orue, A.; Kassanos, P.; George, C.; Aguesse, F.; Mysyk, R.; Radacsi, N.; López-Aranguren, P. Solid-State Li-Ion Batteries with Carbon Microfiber Electrodes via 3D Electrospinning. *Appl. Phys. Lett.* **2023**, *122* (17), 173903. https://doi.org/10.1063/5.0151949.

(33) Zhang, H.; Ning, H.; Busbee, J.; Shen, Z.; Kiggins, C.; Hua, Y.; Eaves, J.; Davis, J.; Shi, T.; Shao, Y.-T.; Zuo, J.-M.; Hong, X.; Chan, Y.; Wang, S.; Wang, P.; Sun, P.; Xu, S.; Liu, J.; Braun, P. V. Electroplating Lithium Transition Metal Oxides. *Sci. Adv.* **2017**, *3* (5), e1602427. https://doi.org/10.1126/sciadv.1602427.

(34) Ham, Y.; Fritz, N. J.; Hyun, G.; Lee, Y. B.; Nam, J. S.; Kim, I.-D.; Braun, P. V.; Jeon, S. 3D Periodic Polyimide Nano-Networks for Ultrahigh-Rate and Sustainable Energy Storage. *Energy Environ. Sci.* **2021**, *14* (11), 5894–5902. https://doi.org/10.1039/D1EE01739J.

(35) Sun, P.; Li, X.; Shao, J.; Braun, P. V. High-Performance Packaged 3D Lithium-Ion Microbatteries Fabricated Using Imprint Lithography. *Adv. Mater.* **2021**, *33* (1), 2006229. https://doi.org/10.1002/adma.202006229.

(36) Sun, H.; Zhu, J.; Baumann, D.; Peng, L.; Xu, Y.; Shakir, I.; Huang, Y.; Duan, X. Hierarchical 3D Electrodes for Electrochemical Energy Storage. *Nat. Rev. Mater.* **2018**, *4* (1), 45–60. https://doi.org/10.1038/s41578-018-0069-9.

(37) Chu, T.; Park, S.; Fu, K. (Kelvin). 3D Printing-enabled Advanced Electrode Architecture Design. *Carbon Energy* **2021**, *3* (3), 424–439. https://doi.org/10.1002/cey2.114.

(38) Liu, X.; Wang, J.; Wu, B.; Li, H.; Ma, P.; Yang, H. Y. 3D Printed Electrode Structures and Materials for Rechargeable Batteries. *Adv. Funct. Mater.* **2025**, *35* (34), 2500946. https://doi.org/10.1002/adfm.202500946.

(39) Sun, K.; Wei, T.; Ahn, B. Y.; Seo, J. Y.; Dillon, S. J.; Lewis, J. A. 3D Printing of Interdigitated Li-Ion Microbattery Architectures. *Adv. Mater.* **2013**, *25* (33), 4539–4543. https://doi.org/10.1002/adma.201301036.

(40) Wei, T.; Ahn, B. Y.; Grotto, J.; Lewis, J. A. 3D Printing of Customized Li-Ion Batteries with Thick Electrodes. *Adv. Mater.* **2018**, *30* (16), 1703027. https://doi.org/10.1002/adma.201703027.

(41) Cong, M.; Du, Y.; Liu, Y.; Xu, J.; Zhao, K.; Lian, F.; Lin, T.; Shao, H. Preparation of Lithium Iron Phosphate Battery by 3D Printing. *Ceram. Int.* **2024**, *50* (9), 14749–14756. https://doi.org/10.1016/j.ceramint.2024.01.389.

(42) Gao, W.; Pumera, M. 3D Printed Nanocarbon Frameworks for Li-Ion Battery Cathodes. *Adv. Funct. Mater.* **2021**, *31* (11), 2007285. https://doi.org/10.1002/adfm.202007285.

(43) Hu, X.; Chen, Y.; Xu, W.; Zhu, Y.; Kim, D.; Fan, Y.; Yu, B.; Chen, Y. 3D-Printed Thermoplastic Polyurethane Electrodes for Customizable, Flexible Lithium-Ion Batteries with an Ultra-Long Lifetime. *Small* **2023**, *19* (34), 2301604. https://doi.org/10.1002/smll.202301604.

(44) Park, S.; Cao, Z.; Sung, D. H.; Fu, K. K. High-Loaded Electrode Filaments for Additive Manufacturing of Structural Batteries. *Adv. Energy Mater.* **2023**, *13* (38), 2301704. https://doi.org/10.1002/aenm.202301704.

(45) Wang, J.; Sun, Q.; Gao, X.; Wang, C.; Li, W.; Holness, F. B.; Zheng, M.; Li, R.; Price, A. D.; Sun, X.; Sham, T.-K.; Sun, X. Toward High Areal Energy and Power Density Electrode for Li-Ion Batteries via Optimized 3D Printing Approach. *ACS Appl. Mater. Interfaces* **2018**, *10* (46), 39794–39801. https://doi.org/10.1021/acsami.8b14797.

(46) Saccone, M. A.; Greer, J. R. Understanding and Mitigating Mechanical Degradation in Lithium–Sulfur Batteries: Additive Manufacturing of Li2S Composites and Nanomechanical Particle Compressions. *J. Mater. Res.* **2021**, *36* (18), 3656–3666. https://doi.org/10.1557/s43578-021-00182-w.

(47) Yee, D. W.; Citrin, M. A.; Taylor, Z. W.; Saccone, M. A.; Tovmasyan, V. L.; Greer, J. R. Hydrogel-Based Additive Manufacturing of Lithium Cobalt Oxide. *Adv. Mater. Technol.* **2021**, *6* (2), 2000791. https://doi.org/10.1002/admt.202000791.

(48) Saccone, M. A.; Gallivan, R. A.; Narita, K.; Yee, D. W.; Greer, J. R. Additive Manufacturing of Micro-Architected Metals via Hydrogel Infusion. *Nature* **2022**, *612* (7941), 685–690. https://doi.org/10.1038/s41586-022-05433-2.

(49) Sun, Y.; Greer, J. R. Micro-Architected Lithium Cobalt Oxide. *Adv. Sci.* **2025**, *12* (43), e13312. https://doi.org/10.1002/advs.202513312.

(50) Wu, L.; Zhang, J. *Ab Initio* Study of Anisotropic Mechanical Properties of LiCoO2 during Lithium Intercalation and Deintercalation Process. *J. Appl. Phys.* **2015**, *118* (22), 225101. https://doi.org/10.1063/1.4937409.

(51) Qi, Y.; Hector, L. G.; James, C.; Kim, K. J. Lithium Concentration Dependent Elastic Properties of Battery Electrode Materials from First Principles Calculations. *J. Electrochem. Soc.* **2014**, *161* (11), F3010–F3018. https://doi.org/10.1149/2.0031411jes.

(52) Swallow, J. G.; Woodford, W. H.; McGrogan, F. P.; Ferralis, N.; Chiang, Y.-M.; Van Vliet, K. J. Effect of Electrochemical Charging on Elastoplastic Properties and Fracture Toughness of Li_X CoO_2. *J. Electrochem. Soc.* **2014**, *161* (11), F3084–F3090. https://doi.org/10.1149/2.0141411jes.

(53) Cho, J.; Losego, M. D.; Zhang, H. G.; Kim, H.; Zuo, J.; Petrov, I.; Cahill, D. G.; Braun, P. V. Electrochemically Tunable Thermal Conductivity of Lithium Cobalt Oxide. *Nat. Commun.* **2014**, *5* (1), 4035. https://doi.org/10.1038/ncomms5035.

(54) Zahiri, B.; Patra, A.; Kiggins, C.; Yong, A. X. B.; Ertekin, E.; Cook, J. B.; Braun, P. V. Revealing the Role of the Cathode–Electrolyte Interface on Solid-State Batteries. *Nat. Mater.* **2021**, *20* (10), 1392–1400. https://doi.org/10.1038/s41563-021-01016-0.

(55) Qu, M.; Woodford, W. H.; Maloney, J. M.; Carter, W. C.; Chiang, Y.; Van Vliet, K. J. Nanomechanical Quantification of Elastic, Plastic, and Fracture Properties of $LiCoO_2$. *Adv. Energy Mater.* **2012**, *2* (8), 940–944. https://doi.org/10.1002/aenm.201200107.

(56) Cheng, E. J.; Taylor, N. J.; Wolfenstine, J.; Sakamoto, J. Elastic Properties of Lithium Cobalt Oxide ($LiCoO_2$). *J. Asian Ceram. Soc.* **2017**, *5* (2), 113–117. https://doi.org/10.1016/j.jascer.2017.03.001.

(57) Xu, R.; Sun, H.; De Vasconcelos, L. S.; Zhao, K. Mechanical and Structural Degradation of $LiNi_x$ Mn_y Co_z O_2 Cathode in Li-Ion Batteries: An Experimental Study. *J. Electrochem. Soc.* **2017**, *164* (13), A3333–A3341. https://doi.org/10.1149/2.1751713jes.

(58) Roberts, A. P.; Garboczi, E. J. Elastic Properties of Model Porous Ceramics. *J. Am. Ceram. Soc.* **2000**, *83* (12), 3041–3048. https://doi.org/10.1111/j.1151-2916.2000.tb01680.x.

(59) Rice, R. W. *Porosity of Ceramics*; Materials engineering; Dekker: New York, 1998.

(60) *Mechanical Properties and Deformation Behavior of Materials Having Ultra-Fine Microstructures*; Nastasi, M., Parkin, D. M., Gleiter, H., Eds.; Springer Netherlands: Dordrecht, 1993. https://doi.org/10.1007/978-94-011-1765-4.

(61) Field, J. S.; Swain, M. V.; Dukino, R. D. Determination of Fracture Toughness from the Extra Penetration Produced by Indentation-Induced Pop-In. *J. Mater. Res.* **2003**, *18* (6), 1412–1419. https://doi.org/10.1557/JMR.2003.0194.

(62) Jang, J.; Pharr, G. M. Influence of Indenter Angle on Cracking in Si and Ge during Nanoindentation. *Acta Mater.* **2008**, *56* (16), 4458–4469. https://doi.org/10.1016/j.actamat.2008.05.005.

(63) Nasir Khan, M.; Bashir, J. Synthesis and Structural Refinement of LiAlxCo1−xO2 System. *Mater. Res. Bull.* **2006**, *41* (9), 1589–1595. https://doi.org/10.1016/j.materresbull.2006.02.032.

(64) Yoon, S. G.; Vishnugopi, B. S.; Alsaç, E. P.; Jeong, W. J.; Sandoval, S. E.; Nelson, D. L.; Ayyaswamy, A.; Mukherjee, P. P.; McDowell, M. T. Synergistic Evolution of Alloy Nanoparticles and Carbon in Solid-State Lithium Metal Anode Composites at Low Stack Pressure. *ACS Nano* **2024**, *18* (31), 20792–20805. https://doi.org/10.1021/acsnano.4c07687.

(65) Yoon, S. G.; Vishnugopi, B.; Nelson, D.; Xiao Bin Yong, A.; Wang, Y.; Sandoval, S.; Thomas, T.; Cavallaro, K.; Shevchenko, P.; Alsaç, E. P.; Wang, C.; Singla, A.; Greer, J.; Ertekin, E.; Mukherjee, P.; McDowell, M. Interface Morphogenesis with a Deformable Secondary Phase in Solid-State Lithium Batteries. *Science* **2025**, *388* (6751), 1062–1068. https://doi.org/10.1126/science.adt5229.

(66) Tariq, S.; Ammigan, K.; Hurh, P.; Schultz, R.; Liu, P.; Shang, J. LI Material Testing-Fermilab Antiproton Source Litihum Collection Lens. In *Proceedings of the 2003 Bipolar/BiCMOS Circuits and Technology Meeting (IEEE Cat. No.03CH37440)*; IEEE: Portland, OR, USA, 2003; Vol. 3, pp 1452–1454. https://doi.org/10.1109/PAC.2003.1288558.

(67) Robertson, W. M.; Montgomery, D. J. Elastic Modulus of Isotopically-Concentrated Lithium. *Phys. Rev.* **1960**, *117* (2), 440–442. https://doi.org/10.1103/PhysRev.117.440.

(68) Schultz, R. P. *Lithium: Measurement of Young's Modulus and Yield Strength*; Technical Report FERMILAB-TM-2191; Fermi National Accelerator Laboratory, 2002. https://doi.org/10.2172/804180.

(69) Darnbrough, E.; Aspinall, J.; Pasta, M.; Armstrong, D. E. J. Elastic and Plastic Mechanical Properties of Lithium Measured by Nanoindentation. *Mater. Des.* **2023**, *233*, 112200. https://doi.org/10.1016/j.matdes.2023.112200.

(70) Slotwinski, T.; Trivisonno, J. Temperature Dependence of the Elastic Constants of Single Crystal Lithium. *J. Phys. Chem. Solids* **1969**, *30* (5), 1276–1278. https://doi.org/10.1016/0022-3697(69)90386-2.

(71) Masias, A.; Felten, N.; Garcia-Mendez, R.; Wolfenstine, J.; Sakamoto, J. Elastic, Plastic, and Creep Mechanical Properties of Lithium Metal. *J. Mater. Sci.* **2019**, *54* (3), 2585–2600. https://doi.org/10.1007/s10853-018-2971-3.

(72) Fincher, C. D.; Ojeda, D.; Zhang, Y.; Pharr, G. M.; Pharr, M. Mechanical Properties of Metallic Lithium: From Nano to Bulk Scales. *Acta Mater.* **2020**, *186*, 215–222. https://doi.org/10.1016/j.actamat.2019.12.036.

(73) Herbert, E. G.; Hackney, S. A.; Thole, V.; Dudney, N. J.; Phani, P. S. Nanoindentation of High-Purity Vapor Deposited Lithium Films: A Mechanistic Rationalization of the Transition from Diffusion to Dislocation-Mediated Flow. *J. Mater. Res.* **2018**, *33* (10), 1361–1368. https://doi.org/10.1557/jmr.2018.85.

(74) Fincher, C. D.; Zhang, Y.; Pharr, G. M.; Pharr, M. Elastic and Plastic Characteristics of Sodium Metal. *ACS Appl. Energy Mater.* **2020**, *3* (2), 1759–1767. https://doi.org/10.1021/acsaem.9b02225.

(75) Wang, M. J.; Chang, J.-Y.; Wolfenstine, J. B.; Sakamoto, J. Analysis of Elastic, Plastic, and Creep Properties of Sodium Metal and Implications for Solid-State Batteries. *Materialia* **2020**, *12*, 100792. https://doi.org/10.1016/j.mtla.2020.100792.

(76) Liu, Q.; Zhang, L.; Sun, H.; Geng, L.; Li, Y.; Tang, Y.; Jia, P.; Wang, Z.; Dai, Q.; Shen, T.; Tang, Y.; Zhu, T.; Huang, J. *In Situ* Observation of Sodium Dendrite Growth and Concurrent Mechanical Property Measurements Using an Environmental Transmission Electron Microscopy–Atomic Force Microscopy (ETEM-AFM) Platform. *ACS Energy Lett.* **2020**, *5* (8), 2546–2559. https://doi.org/10.1021/acsenergylett.0c01214.

(77) Zhang, L.; Yang, T.; Du, C.; Liu, Q.; Tang, Y.; Zhao, J.; Wang, B.; Chen, T.; Sun, Y.; Jia, P.; Li, H.; Geng, L.; Chen, J.; Ye, H.; Wang, Z.; Li, Y.; Sun, H.; Li, X.; Dai, Q.; Tang, Y.; Peng, Q.; Shen, T.; Zhang, S.; Zhu, T.; Huang, J. Lithium Whisker Growth and Stress Generation in an in Situ Atomic Force Microscope–Environmental Transmission Electron Microscope Set-Up. *Nat. Nanotechnol.* **2020**, *15* (2), 94–98. https://doi.org/10.1038/s41565-019-0604-x.

(78) Citrin, M. A.; Yang, H.; Nieh, S. K.; Berry, J.; Gao, W.; Pan, X.; Srolovitz, D. J.; Greer, J. R. From Ion to Atom to Dendrite: Formation and Nanomechanical Behavior of Electrodeposited Lithium. *MRS Bull.* **2020**, *45* (11), 891–904. https://doi.org/10.1557/mrs.2020.148.

(79) Fischer, M. G.; Hua, X.; Wilts, B. D.; Castillo-Martínez, E.; Steiner, U. Polymer-Templated $LiFePO_4$ /C Nanonetworks as High-Performance Cathode Materials for Lithium-Ion Batteries. *ACS Appl. Mater. Interfaces* **2018**, *10* (2), 1646–1653. https://doi.org/10.1021/acsami.7b12376.

(80) Padhi, A. K.; Nanjundaswamy, K. S.; Goodenough, J. B. Phospho-olivines as Positive-Electrode Materials for Rechargeable Lithium Batteries. *J. Electrochem. Soc.* **1997**, *144* (4), 1188–1194. https://doi.org/10.1149/1.1837571.

(81) Katsuyama, Y.; Kudo, A.; Kobayashi, H.; Han, J.; Chen, M.; Honma, I.; Kaner, R. B. A 3D-Printed, Freestanding Carbon Lattice for Sodium Ion Batteries. *Small* **2022**, *18* (29), 2202277. https://doi.org/10.1002/smll.202202277.

(82) Xu, S.; Li, S.; Zhu, L.; Zhao, Y.; Dou, H.; Zhang, X. Optimization of $LiCoO_2$ Thick Electrodes with Low Tortuosity for Lithium-Ion Batteries by 3D Printing. *J. Mater. Chem. A* **2025**, *13* (14), 9747–9756. https://doi.org/10.1039/D5TA00723B.

(83) Liu, C.; Qiu, Y.; Liu, Y.; Xu, K.; Zhao, N.; Lao, C.; Shen, J.; Chen, Z. Novel 3D Grid Porous Li4Ti5O12 Thick Electrodes Fabricated by 3D Printing for High Performance Lithium-Ion Batteries. *J. Adv. Ceram.* **2022**, *11* (2), 295–307. https://doi.org/10.1007/s40145-021-0533-7.

(84) Roberts, M.; Huang, A. F.; Johns, P.; Owen, J. Dip–Spin Coating of Reticulated Vitreous Carbon with Composite Materials to Act as an Electrode for 3D Microstructured Lithium Ion Batteries. *J. Power Sources* **2013**, *224*, 250–259. https://doi.org/10.1016/j.jpowsour.2012.09.103.

(85) Dong, H.; Liu, G.; Li, S.; Deng, S.; Cui, Y.; Liu, H.; Liu, H.; Sun, X. Design of a 3D-Porous Structure with Residual Carbon for High-Performance Ni-Rich Cathode Materials. *ACS Appl. Mater. Interfaces* **2019**, *11* (2), 2500–2506. https://doi.org/10.1021/acsami.8b17800.

(86) Wang, Y.; Zhang, Y.; Cao, D.; Ji, T.; Ren, H.; Wang, G.; Wu, Q.; Zhu, H. Designing Low Tortuosity Electrodes through Pattern Optimization for Fast-Charging. *Small Methods* **2023**, *7* (4), 2201344. https://doi.org/10.1002/smtd.202201344.

(87) Kim, H.; Oh, S. K.; Lee, J.; Doo, S. W.; Kim, Y.; Lee, K. T. Failure Mode of Thick Cathodes for Li-Ion Batteries: Variation of State-of-Charge along the Electrode Thickness Direction. *Electrochimica Acta* **2021**, *370*, 137743. https://doi.org/10.1016/j.electacta.2021.137743.

(88) Katsuyama, Y.; Kudo, A.; Kobayashi, H.; Han, J.; Chen, M.; Honma, I.; Kaner, R. B. A 3D-Printed, Freestanding Carbon Lattice for Sodium Ion Batteries. *Small* **2022**, *18* (29), 2202277. https://doi.org/10.1002/smll.202202277.

(89) Doyle, M.; Fuller, T. F.; Newman, J. Modeling of Galvanostatic Charge and Discharge of the Lithium/Polymer/Insertion Cell. *J. Electrochem. Soc.* **1993**, *140* (6), 1526–1533. https://doi.org/10.1149/1.2221597.

(90) Zadin, V.; Kasemägi, H.; Aabloo, A.; Brandell, D. Modelling Electrode Material Utilization in the Trench Model 3D-Microbattery by Finite Element Analysis. *J. Power Sources* **2010**, *195* (18), 6218–6224. https://doi.org/10.1016/j.jpowsour.2010.02.056.

(91) Trembacki, B.; Duoss, E.; Oxberry, G.; Stadermann, M.; Murthy, J. Mesoscale Electrochemical Performance Simulation of 3D Interpenetrating Lithium-Ion Battery Electrodes. *J. Electrochem. Soc.* **2019**, *166* (6), A923–A934. https://doi.org/10.1149/2.0031906jes.

(92) Lundgren, H.; Behm, M.; Lindbergh, G. Electrochemical Characterization and Temperature Dependency of Mass-Transport Properties of $LiPF_6$ in EC:DEC. *J. Electrochem. Soc.* **2015**, *162* (3), A413–A420. https://doi.org/10.1149/2.0641503jes.

(93) Tjaden, B.; Cooper, S. J.; Brett, D. J.; Kramer, D.; Shearing, P. R. On the Origin and Application of the Bruggeman Correlation for Analysing Transport Phenomena in Electrochemical Systems. *Curr. Opin. Chem. Eng.* **2016**, *12*, 44–51. https://doi.org/10.1016/j.coche.2016.02.006.

(94) Delacourt, C.; Laffont, L.; Bouchet, R.; Wurm, C. Toward Understanding of Electrical Limitations (Electronic, Ionic) in LiMPO4 (M = Fe, Mn) Electrode Materials. *J. Electrochem. Soc.* **2005**, *152(5)*, A913–A921. https://doi.org/10.1149/1.1884787.

(95) Wang, C.; Kasavajjula, U. S.; Arce, P. E. A Discharge Model for Phase Transformation Electrodes: Formulation, Experimental Validation, and Analysis. *J. Phys. Chem. C* **2007**, *111* (44), 16656–16663. https://doi.org/10.1021/jp074490u.

(96) Ye, Y.; Shi, Y.; Tay, A. A. O. Electro-Thermal Cycle Life Model for Lithium Iron Phosphate Battery. *J. Power Sources* **2012**, *217*, 509–518. https://doi.org/10.1016/j.jpowsour.2012.06.055.

(97) Franke-Lang, R.; Kowal, J. Electrochemical Model-Based Investigation of Thick LiFePO4 Electrode Design Parameters. *Modelling* **2021**, *2* (2), 259–287. https://doi.org/10.3390/modelling2020014.

(98) Zhu, Y.; Li, J.; Saleh, M. S.; Pham, H.; Plateau, T. P.; Panat, R.; Park, J. Towards High-Performance Li-Ion Batteries via Optimized Three-Dimensional Micro-Lattice Electrode Architectures. *J. Power Sources* **2020**, *476*, 228593. https://doi.org/10.1016/j.jpowsour.2020.228593.

(99) Wu, S.; Luo, E.; Ouyang, J.; Lu, Q.; Zhang, X.; Wei, D.; Han, W. K.; Xu, X.; Wei, L. Tuning the Graphitization of the Carbon Coating Layer on LiFePO4 Enables Superior Properties. *Int. J. Electrochem. Sci.* **2024**, *19* (1), 100450. https://doi.org/10.1016/j.ijoes.2023.100450.

(100) Delacourt, C.; Wurm, C.; Laffont, L.; Leriche, J.-B.; Masquelier, C. Electrochemical and Electrical Properties of Nb- and/or C-Containing LiFePO4 Composites. *Solid State Ion.* **2006**, *177* (3–4), 333–341. https://doi.org/10.1016/j.ssi.2005.11.003.

(101) Fu, K.; Wang, Y.; Yan, C.; Yao, Y.; Chen, Y.; Dai, J.; Lacey, S.; Wang, Y.; Wan, J.; Li, T.; Wang, Z.; Xu, Y.; Hu, L. Graphene Oxide-Based Electrode Inks for 3D-Printed Lithium-Ion Batteries. *Adv. Mater.* **2016**, *28* (13), 2587–2594. https://doi.org/10.1002/adma.201505391.

(102) Xu, K.; Zhao, N.; Li, Y.; Wang, P.; Liu, Z.; Chen, Z.; Shen, J.; Liu, C. Design and 3D Printing of Interdigitated Electrode Structures for High-Performance Full Lithium-Ion Battery. *Chin. J. Mech. Eng. Addit. Manuf. Front.* **2022**, *1* (4), 100053. https://doi.org/10.1016/j.cjmeam.2022.100053.